UNIVERSITY OF
BIRMINGHAM

MILLIMETER-WAVE POWER DETECTORS

by

HARSHWARDHAN KAMBLE

A thesis submitted to the University of Birmingham for the degree of DOCTOR OF PHILOSOPHY

School of Electronic, Electrical and Systems Engineering,
University of Birmingham

May 2024

Abstract

The power measurement traceability above 100 GHz has been challenging due to the unavailability of commercial power transfer standards above 100 GHz. As the frequency increases, the sensor mounting becomes difficult in the increasingly small waveguides, posing fabrication challenges and losses. The commercial transfer standards based on thermistor mount were only operating up to W-band (75-110 GHz), and production has stopped. The emerging applications above the W-band demand the establishment of new power metrology capabilities. This thesis aims to develop new power detectors to meet this urgent demand.

This thesis primarily focuses on the bolometric power detector as a transfer standard in the D-band (110-170 GHz). The bolometric detector consists of a thin film sensor element in the E-plane of the waveguide. The element is designed to be a dual-line thin film on a quartz substrate and has proven to improve the bandwidth. The equivalent circuit analysis is presented on single and dual-line structures inside the waveguide. The power detector body is designed in plastic PEEK (polyether ether ketone). It is enclosed in dual shielding layers; the inner is PEEK, and the outer is aluminium. All these measures have helped achieve a power detector with a competitive response time of fewer than 2.6 seconds (a limitation of the external measurement system/facility). The device can operate at ambient temperature, benefiting from additional dummy sensors within the inner shielding. It has shown a very good short-term time response with only ~0.19% deviation in a given time interval, which is very close to a commercial PM5 sensor with ~0.27% deviation. The long-term time response is also impressive, with a deviation of less than 0.6%, similar to a commercial PM5 sensor. The fast response time, good thermal isolation, and ambient compensation ability make it suitable for transfer/working standards, which can be used in ambient temperature environments.

This thesis also demonstrated a Schottky diode power detector. Schottky diodes are most suitable for applications such as imaging, communication and particle accelerators where fast response time (in picoseconds or ps) is vital over absolute power measurement. The device has been successfully designed, fabricated and tested. This is a square law power detector, where the output voltage is proportional to the square of the input voltage. The detector split blocks are fabricated in aluminium and plated with gold. The measurement shows an average responsivity of 5000 V/W over the D-band, and the minimum is 1900 V/W at 160 GHz for -20 dBm input power.

To those struggling for the emancipation of marginalised and downtrodden….

"*Cultivation of mind should be the ultimate aim of human existence….*"

- Dr. B. R. Ambedkar

Acknowledgement

I would like to express my deep gratitude to my supervisor, Prof. Yi Wang, who has patiently guided me throughout the project. I thank him for encouraging me during the challenging times of the COVID-19 pandemic. Without his support, this work would never have been accomplished. I also thank him for supporting my participation in activities such as officer elections in the university's Guild of Students and an internship in Germany, which helped me overcome the boundaries and gain confidence.

I want to thank NPL colleagues Dr. Murat Celep, Mr. Daniel Stokes and Mr. James Skinner for performing power and S-parameter measurements for the bolometric detector and assisting me with S-parameter measurements for the diode detector. I thank Dr. Milan Salek and Dr. Murat Celep for their valuable advice during the bolometric detector design. I want to thank Dr. Aydin Sabouri for giving initial guidance on the dimension constraints for sensor chip fabrication. I also thank Dr. Xunshen Wang for his expertise in fabricating the sensor chip. I want to thank Mr. Jag Sangha, Mr. Warren Hay and their team from the university's workshop for manufacturing the bolometric detector housing.

I want to thank Teratech colleagues Dr. Jeffrey Powell, Dr. Byron Alderman, and the team for their guidance on the Schottky diode detector, fabrication and power measurement.

I want to thank all my colleagues from the Emerging Device Technology Lab for their friendly advice, support and company during my stay in Birmingham, U.K. The Friday walk-turned-dinner with Dr. Milan Salek, Dr. Talal Skaik, Lu Qian, and others have been good times in Birmingham, with lots of fruitful discussions and fun. Thanks to all of them and Dr. Ali Musa Mohammed for promptly looking into my queries related to academia and school administration. Also, thank all my friends from India, who have always wished me success.

I want to acknowledge my financial sponsor, the Social Justice and Special Assistance Department, State Government of Maharashtra, India, for supporting my education under the 'Rajarshi Shahu Maharaj Foreign Scholarship'.

Finally, I would like to acknowledge with gratitude the support and love of my parents, Mr. Baban Kamble and Mrs. Sujata Kamble; my brother, Tushar; and my sister, Swati. Thanks to our late pet cats, Manee and Kitty, for making me happy and relaxed with their adorable and funny poses.

Table of Content

CHAPTER 1

INTRODUCTION

1.1 Power Detection Overview

Power is one of the fundamental quantities critical in the radio frequency (RF) and microwave fields, and it has economic and technical importance [1]. Power measurement is preferred in high frequency over other quantities, such as current and voltage. Low frequencies have a wavelength much longer than the circuit dimension with insignificant phase delay between two points in a circuit. Therefore, voltage and current remain constant along the line and can be measured easily. However, as the frequency goes higher (> 1 GHz), the wavelength becomes comparable (< 30 cm) to the circuit dimension with a significant phase delay between the two points. This phase delay causes varying voltage and current, which then become difficult to measure. However, the power remains the same over the transmission line (TL) length, which is easy to measure. Moreover, voltage and current depend on the TL's characteristics impedance (50 Ω or 75 Ω system), considering matched load conditions. In contrast, the power measured is independent of the characteristic impedance and can be measured accurately. Also, there is no straightforward way to measure the current and voltage in hollow waveguides, so power measurement is more convenient [2], [3].

There are two types of power detectors: thermal and electric/electronic, which can be placed under the direct detection category, as shown in Figure 1.1. As the name 'direct' indicates, the electromagnetic energy interacts directly with the sensor, unlike heterodyne, where a signal is first frequency-down-converted before being detected using a diode or transistor detector. Not all direct detectors are power detectors, but all power detectors are direct detectors.

Thermal detectors sense the temperature rise when RF energy hits the sensing element. The change in material resistivity or induced voltage, depending on the type of sensor element (thermistor or thermoelectric), is calibrated to measure the RF power. A thermistor is a sensor whose resistance changes due to a temperature rise, whereas a thermoelectric is a sensor made of two metals forming a hot and cold junction. It generates a voltage when the temperature of the hot junction is raised with respect to the cold junction. A thin film sensor can be a thermistor to measure resistance change or a highly resistive metal attached to a thermocouple to measure generated voltage. Thermal detectors are preferred for absolute power measurement in metrology applications due to their linearity and stability [4]. They suffer from the long thermal time constant, so they are not used in electronic circuits where fast detection is necessary, such as in automatic gain control circuits.

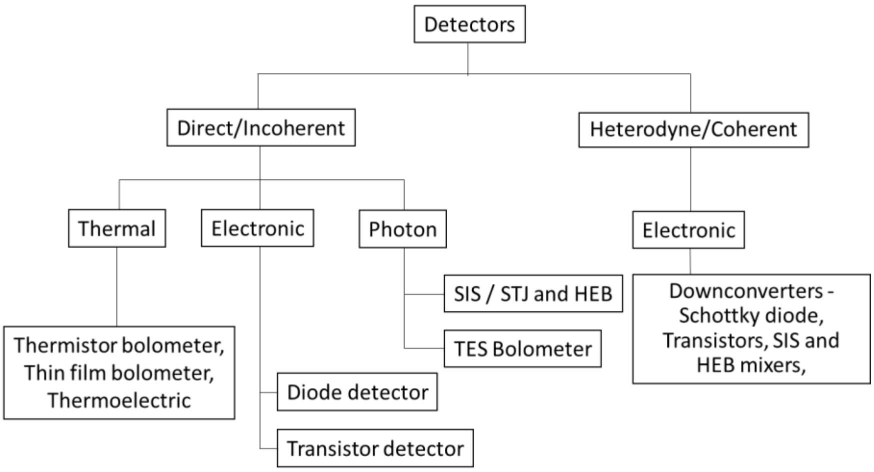

Figure 1.1 Types of detector.

Electronic detectors usually consist of nonlinear devices, diodes and transistors. Schottky contact in the Schottky diode has a nonlinear response. Similarly, the gate contact in FET (field effect transistors) and the emitter-base junction in BJT (bipolar Junction transistors) have a nonlinear response. Depending on the applications, they are used in square law (power) and linear (rectification) modes. Square law detectors are used as power detectors in electronic circuits, where the output voltage is proportional to the square of the input voltage. They benefit from fast response time (in ps for a diode with cut-off frequency 0.1-1.5 THz [5]) compared to thermal detectors and are widely preferred where absolute power measurement is unnecessary, for example, in network analysers, communication systems and radio astronomy. Linear detectors are the rectifiers used in applications such as envelope detectors, a type of AM (amplitude modulation) demodulator.

Photon detectors, SIS (superconductor-insulator-superconductor), TES (transition edge sensor) bolometer and HEB (hot-electron-bolometer) are used as direct detectors above 1 THz [6][7]. These are cryogenic (low temperature) detectors that use the physics of superconductors, such as the formation of cooper pair and transition temperature Tc and the quantum mechanical phenomena, such as quantum tunnelling. These are not used as power detectors; instead, they detect submillimetre wave photons/particle energies. It is used in radio astronomy at cryogenic temperatures where high sensitivity is required.

Heterodyne detectors have become common at high frequencies due to the lack of electronic components such as resistors, capacitors, inductors and low-loss transmission media [6]. The RF signal is mixed with the local oscillator signal using a nonlinear device called a mixer. At room temperature, the Schottky diode is used for mixing, which produces the IF (intermediate frequency) signal that is easy to process with available electronics. In superconductors, the tunnelling current in SIS and resistivity in HEB are nonlinear near the transition temperature. In terahertz astronomy, the high-frequency signal is first down-converted by using SIS or HEB mixers [6][7]. After the downconversion, the diode-based or transistor-based envelope detector or square law detector is used for detection. Among all the detectors discussed above, the thermal and electronic detectors are of interest to research as they are used for RF power detection.

1.2 Thesis Motivation and Objective

In the electromagnetic spectrum, microwave (3-30 GHz) and millimetre (30-300 GHz) bands have a major contribution to communication, military, astronomy, and medical applications. However, frequencies above 100 GHz in millimetres and terahertz (300 GHz to 3 THz) bands are not substantially commercialised [6]. Today, this band is primarily used for scientific research in astronomy and spectroscopy, while a survey of more emerging applications above 100 GHz, such as wireless cognition, sensing, imaging, precise positioning, and 6G (six-generation), was done in [8]. One of the reasons behind this band being immature for many years is manufacturing limitations and the cost of fabrication at very short wavelengths ($\lambda < 3$ mm). Considerable research is going on to utilise the band using advanced fabrication techniques such as high-precision CNC (computer numerical control) machining, 3D (three-dimensional) printing, and photolithography [9]. Another reason is that very few commercial solid-state sources and detectors are readily available, as they suffer from parasitic losses and limited efficiency [6]. Accurately measuring absolute power is one of the keys to driving the development in this frequency band. While expensive solid-state devices struggle to generate high power above 100 GHz, every extra dBm has economic value and hence does the accurate power measurement [1]. At such time, RF and microwave technology seek a cost-effective solution to measure power above 100 GHz. Only a handful of commercial devices are available, for example, the Erickson PM5 power meter, but uses waveguide tapers to cover higher frequencies [10].

This PhD project is, therefore, primarily focused on power detectors at D-band (110-170 GHz) frequencies for metrology application as a transfer standard at the national metrology institutes and laboratories of different countries. There are already detectors in this band, but they are using calorimetric techniques, which have a slow response time due to the large volume of absorbing elements [11]. Hence, their use is sometimes limited to as a load in primary power standard (calorimeter setup). This work aims to reduce the response time, reduce the temperature drift, and compensate for ambient temperature variation with the additional sensor. This work is based on the thin-film bolometer technique, which aims to overcome these problems. It would not only be used as a load in primary power standards (calorimeter) but also as a transfer standard in the NMIs (national metrology institutes) and as a CW (continuous wave) power sensor in laboratories, industry and communication systems for characterisation purposes.

This PhD work is partly about Schottky diode power detectors for emerging applications in D-band (110-170 GHz), such as six-port radar technology [12], with an aim to achieve responsivity above 2000 V/W.

1.3 State of the Art

1.3.1 Bolometric power detectors

The bolometer is a temperature-sensitive device whose resistance change, hence, the DC (direct current) voltage/current depends on temperature. It can be a thermistor or a thin film-based device. Similarly, another temperature-sensitive device is the thermocouple (a thermopile or thermoelectric sensor), which generates a voltage when there is a temperature gradient between two dissimilar metal junctions. The RF power is applied to these sensor elements, heating up and producing proportional DC voltage/resistance. The traceable DC voltage and resistance standards are well maintained at the NMIs. The RF power can be measured accurately with existing traceability to DC standards. An RF power standard is a complete system of power sensors, controlled temperature, and ambient temperature compensation mechanisms (using a dummy sensor) depending on accuracy.

The power standard has a hierarchy based on accuracy, as shown in Figure 1.2. The accuracy of power measurement depends on the thermal isolation of the sensor element from its body, the thermal isolation of the sensor body from the surrounding/ambient environment, the reflection coefficient (frequency dependence), linearity with respect to frequency and power, DC substitution/equivalence error (depends on overall sensor structure), and potentially more factors in some cases [13].

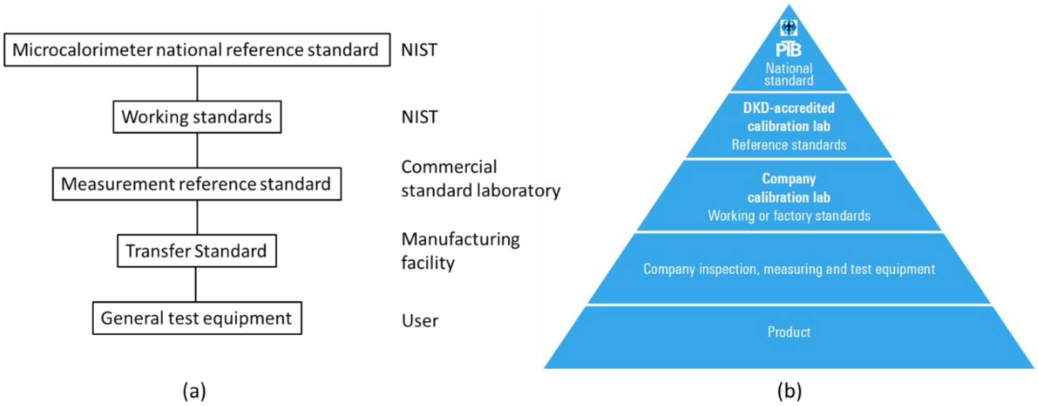

Figure 1.2 Power standard hierarchy (a) at NIST, USA, adapted from [1], (b) at PTB, Germany, reproduced from [14].

The power sensors (bolometric or thermoelectric) can be anywhere in the hierarchy, depending on external conditioning for accurate measurement. The power sensor in its basic form is referred to as a reference or, more commonly, a transfer standard in the literature [15]–[18]. However, a slight distinction between the two is that the reference standard is calibrated using a microcalorimeter system to be recognised as a transfer standard and then can be ready for power measurement. They are also called traceable power standards [19]. The transfer standard can be used to calibrate the commercial power sensor/user equipment [16], [20]. The terms power sensor and power detector are used interchangeably in this thesis. A power meter is a separate instrument that reads the input from the power sensor, processes it, and displays the meaningful measurement result.

Some well-utilised transfer/reference standards based on the bolometric (thermistor [21] or thin film [10]) and thermoelectric [22] are shown in Figure 1.3. These sensors are used with power meters, which consist of necessary electronics and a display to show power readings. The thermistor mount includes a compensation sensor to compensate for the change in ambient temperature. The thermistor beads with high thermal mass suffer from a thermal time constant of around 60 to 90 minutes [14].

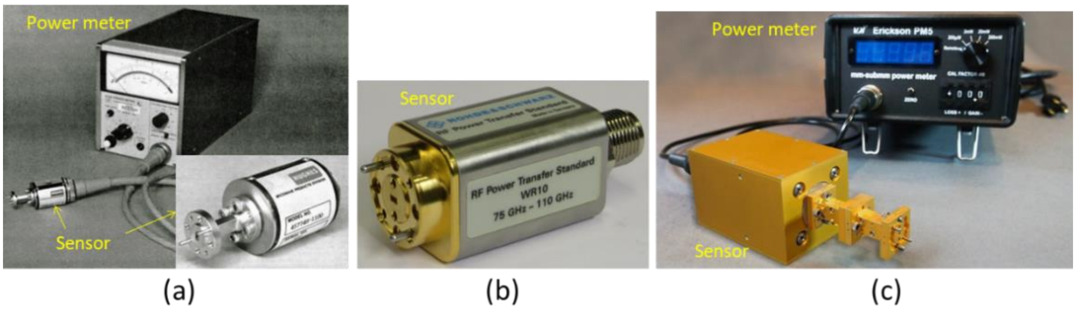

Figure 1.3 Transfer standards (a) Hughes power sensor (thermistor mount) with power meter [21], (b) Rohde & Schwarz thermoelectric standard [22], (c) VDI-Erickson power sensor with power meters [10].

The bolometric or thermoelectric reference standards are used as a load (mount) in the microcalorimeter set-up, which becomes the primary power standard. The microcalorimeter system is highly temperature-conditioned to improve power measurement accuracy. The sensors are enclosed inside the multiple layers of metal vessels and are sometimes immersed in the water baths. Microcalorimeters are maintained as the primary power measurement system in the NMIs, and the calibrated reference standards are transferred down in the hierarchy to continue calibrating the lower standards. The known reference standard is also sent within NMIs of different countries to maintain a common global consensus. This concept of transferring power standards between NMIs is called traceability, and it is currently limited to up to 100 GHz because there is no commercial reference standard [19], [23]. The reference power standard or power sensor with two calorimeter setups and corresponding working frequency is given in Table 1.1, and some examples are shown in Figure 1.4.

Table 1.1 Calorimeter setups.

Configuration	RF Sensor Type	Frequency (GHz)	Reference
Twin Load	Absorbing material with thin film	110-170	[24]
		110-170	[25]
		110-170	[15]
	Commercial VDI-Erickson PM5 with W-band to D-band taper	110-170	[26]
	Absorbing material with thermopile	110-170	[27]
	Absorbing material with thermopile (Quasi-Twin)	110-170	[28]
		140-220	[29]
	Thermoelectric/thermopile (Waveguide-Coplanar waveguide transition)	75-110	[16] [20]
	Absorbing material with thermistor	110-170	[30]
		26.5-40	[17]
	Commercial Thermistor mount from Hughes	75-110	[31]
		40-75, 75-110	[23]
		33-50,50-75	[4]
	Commercial Thermistor	75-110	[32]
		50-75	[33]
		33-50	[18]
	Commercial thermistor mount from HP	18-26.5	[34]
Single Load	Absorbing material (Isothermal calorimeter)	110-170	[35]
	Commercial Thermistor mount from Hughes	75-110	[31]

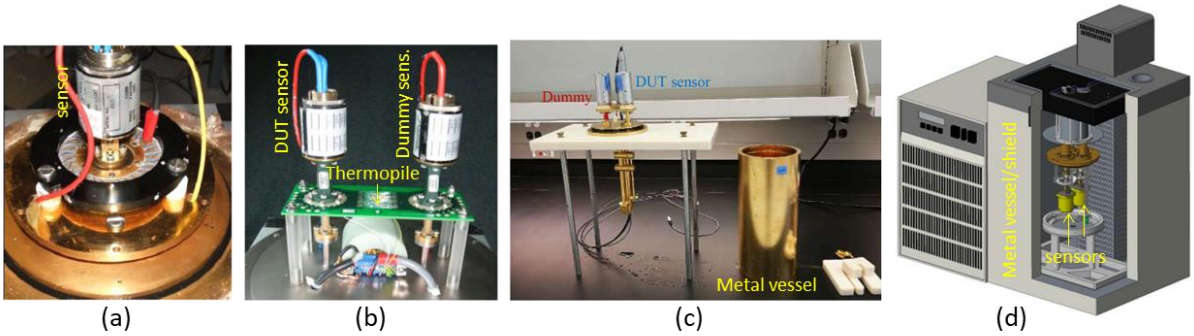

Figure 1.4 Single load calorimeter setup containing: (a) commercial thermistor mount [31], and twin load calorimeter setup containing: (b) commercial thermistor mount [31], (c) custom-manufactured power sensor [15], (d) commercial VDI-Erickson PM5 power sensor [26].

It shall be noted that the calorimeter set-up is used not just for accurate power measurement but also to characterise the reference/transfer standards. It includes finding the effective efficiency and correction factor (g-factor) [13]. The calorimeter meter has two configurations: single load and twin load. The calorimeter requires a reference temperature to analyse heat rise on the mount. Therefore, a thermocouple is placed between the load and the metallic reference ring [31]; this configuration is called a single-load. However, the reference ring could not have the same thermal mass as the mounted sensor and would suffer from longer heat settling time or time required to reach equilibrium. Therefore, the twin load configuration has been more widely adopted as a primary standard. The twin load consists of two similar sensors; one will be active, and the other will be a dummy that replaces the reference ring. Twin load structure reduces temperature drift [32].

The production of commercial reference standards based on thermistor mounts has been stopped because of manufacturing challenges [19], [23]. Individual institutions are developing their methods for power measurement above 100 GHz, as in Table l.1. The de-facto standard available above 100 GHz is the VDI-Ericson PM5 calorimetric power meter [10]. There is a need for an alternative portable transfer standard above 100 GHz with competitive performance.

1.3.2 Schottky diode detectors

Schottky diode is a unipolar, nonlinear device made of a metal-semiconductor junction. The majority of charge carriers are electrons, giving rise to a fast switching time of a few picoseconds when the voltage across it is reversed and vice versa. A conventional p-n junction diode is a bipolar device which has a large reverse recovery time and recombination time when the bias voltage is switched from forward to reverse and vice versa. The Schottky diode’s fast switching speed makes it attractive at mm-wave and terahertz frequencies and can work at ambient temperature. It also has a low forward voltage drop (0.3 V) [36]. The nonlinearity of the Schottky diode is used for the detection/sensing application.

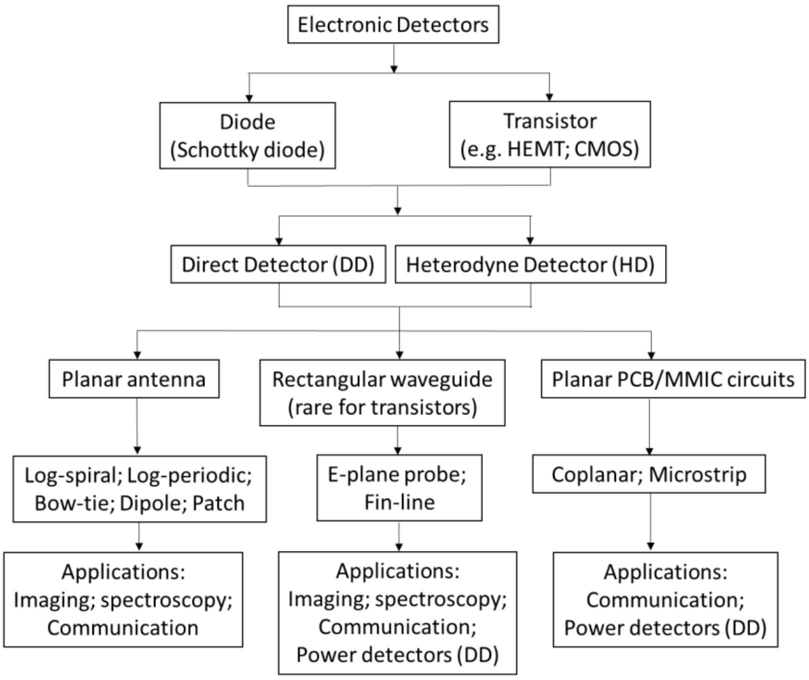

Figure 1.5 Electronic detector types.

The Schottky diode has a wide range of applications and can be divided, as shown in Figure 1.5. The Schottky diode is employed in heterodyne and direct detection schemes where it works as a mixer and square law detector, respectively. Transistors are also used in these applications; however, they are not as common as the Schottky diode at terahertz frequency. The direct and heterodyne detectors are further divided depending on diode mounting, such as planar antenna-based, rectangular waveguide-based, and MMIC (millimetre-wave monolithic integrated circuit)/PCB (printed circuit board) circuit-based.

The literature on the diode and transistor-based detection application in direct and heterodyne modes is summarised in Table 1.2. Imaging applications can be concealed weapon detection for security and earth or planetary remote sensing for weather forecasting. Both direct detectors (planar antenna-based [37]–[39]) and heterodyne detectors (planar antenna-based [40], [41] and waveguide-based [42]) are used in concealed weapon detection or terahertz imaging applications above 100 GHz. The waveguide-based direct detectors [43] are used for the earth's weather monitoring. Several examples of direct detectors are shown in Figure 1.6.

Table 1.2 Electronic detector types.

	Applications	Diode			Transistor		
		Planar Antenna	Rectangular Waveguide	PCB/MMIC Circuits	Planar Antenna	Rectangular Waveguide	PCB/MMIC Circuits
Direct Detectors (DD)	Imaging	[37]–[39]	[43]–[46]		[47], [48]		[49]–[51]
	Spectroscopy	[52]					
	Communication		[53]				[54]
	Power detection		[55], [56]	[57]–[60]			[61]–[64]
Heterodyne Detectors (HD)	Imaging	[40], [41]	[42], [65], [66]				[67]
	Spectroscopy		[68], [69]		[70]		
	Communication		[71]				[72]

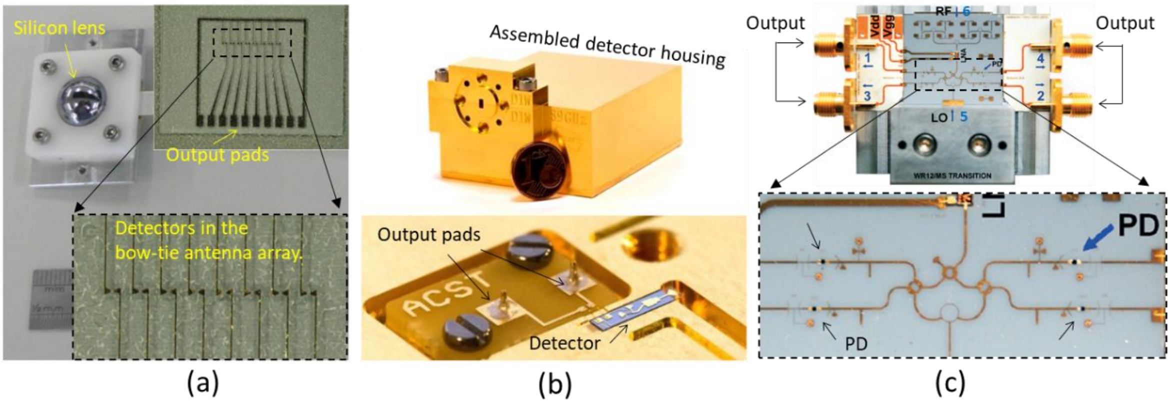

Figure 1.6 Direct detectors (a) planar antenna-based detector for terahertz imaging [39], (b) waveguide-based detector for radiometric imaging [43], [73], (c) PCB/MMIC-based power detector in six-port communication receiver [59], [74].

Spectroscopic applications are about detecting the absorption/emission line of atoms/molecules present in the targeted object. The waveguide-based heterodyne detectors [68], [69] are used in chemical species monitoring in the earth and planetary atmosphere and astronomy. The quasi-optical (planar antenna-based) direct detectors also find applications in spectroscopy and particle accelerators for detecting coherent synchrotron radiation [52], [75]. High-speed, short-distance terahertz communication links are often formed using waveguide-based heterodyne [71] and direct detectors [53].

Although all square law detectors are power detectors, the latter term can be used for a device used explicitly for RF power measurement, such as waveguide-based power meters [55]. Power detectors are also found in six-port MMIC chips for communication [74] and RADAR (radio detection and ranging) [76] applications. The transistor-based power detectors can be seen in communication systems where they are integrated with LNA (low noise amplifier) on the same MMIC to control the gain [61]–[64].

The heterodyne detector gives high sensitivity and spectral resolution; however, complexity increases at high frequencies. On the other hand, direct detectors in receivers consume less power as it does not require a local oscillator [53], [77]. Direct detection is getting more and more attention, especially for space applications, as it allows denser packaging/integration and is being pushed above 100 GHz [78], [79].

1.4 Novelty and Contribution to Knowledge

The thesis primarily focuses on the bolometric power transfer standard for metrology applications. The novelties and key features of the work are:

1) A novel resonance-type sensor covering the whole D-band. Resonant matching generally has poorer matching and narrowed bandwidth than matched load. A folded-line structure is used to generate more matching points so as to increase the bandwidth to cover the whole D-band;

2) Fast response time suitable for use as a transfer standard. This is achieved through a compact design and effective thermal isolation. We have used quartz substrate and polyimide (Kapton) insulation. The sensor body is made of low thermal conductivity plastic (polyether ether ketone or PEEK). All help reduce the thermal time constant;

3) A temperature compensation mechanism using a compact dual-sensor configuration. This is to remove the impact of ambient temperature on the power measurement. These features and the portability of the sensor make it highly suitable as a transfer standard, which is used to establish traceability between the primary standard at the metrology organisation and industrial users. The sensor has been comprehensively characterised, and the capability has been experimentally verified.

4) The thesis also demonstrated a D-band Schottky diode power detector for six-port and radiometry applications. The work has highlighted the challenges of achieving high wideband responsivity using nonlinear devices at high frequencies.

1.5 Organisation of the Thesis

This thesis has a total of six chapters, as follows:

- **Chapter 1** overviews the theme of the thesis. It highlights the motivation and objective, novelty and contribution to the knowledge.
- **Chapter 2** is a detailed literature review on bolometric and Schottky diode power detectors. This chapter explains the research gap, especially in the bolometric power transfer standards. It discusses the typical designs for Schottky diode detectors.
- **Chapter 3** is dedicated to the theoretical aspect of the thin-film waveguide mount for the bolometer and is a base for the next chapter. It proves how the dual line structure can offer a broadband solution and discusses the equivalent circuit and its validation.
- **Chapter 4** is dedicated to the practical aspect of thin-film mount for the bolometer. It presents the design challenges for making the device a reality. The fabrication and measurement of the device are presented toward the end.
- **Chapter 5** is dedicated to an electronic power detector based on the Schottky diode. It starts with a brief theory of the Schottky diode. Then, it discusses the design of the power detector and presents the fabrication and measurement of the device.
- **Chapter 6** concludes the thesis by highlighting this PhD work’s contribution to metrology and possible future endeavours.

CHAPTER 2

LITERATURE REVIEW

This chapter has two parts: the bolometric power detector and the Schottky diode power detector. Both parts have a similar flow, distinguishing the respective detectors based on matching types and then discussing the earlier work in the respective field. The first part of bolometric power standards focuses explicitly on the sensor element's mounting arrangement inside the power standards. The second part talks specifically about Schottky diode power detectors based inside the rectangular waveguide.

2.1 Operating Principles

2.1.1 Thermal Detectors

Thermal detectors are detectors that transduce temperature change in a meaningful quantity. They are used in RF power measurement as the applied RF power heats the sensor element, which changes its physical properties, that is, resistivity (in the case of bolometer) or generates an electromotive force (e.m.f.) (in the case of thermocouple or thermoelectric detector) which can be calibrated to measure power.

Bolometers: Thermistor and Thin film barrator:

The bolometers are temperature sensors whose resistance changes due to temperature changes. The sensor material whose resistance increases due to an increase in temperature is termed a material with a positive temperature coefficient of resistance (PTC). The material whose resistance decreases with a temperature rise is categorised as a negative temperature coefficient of resistance (NTC). There are two types of bolometers: thermistors and barrators. Thermistors are typically made of NTC materials (metal oxides) and barrators of PTC materials (e.g. platinum). The typical thermistor bead schematic is shown in Figure 2.1 (a). The semiconductor bead of diameter 50-70 µm is protected under the glass film with platinum wire of diameter 25 µm for electrical connection [80]. The RF power is absorbed by the bolometer element or by the absorber connected to the bolometer element, causing the temperature to rise and, in turn, the resistance to change.

Bolometers are used in one of the branches of the Wheastone Balanced Bridge, as shown in Figure 2.1 (b). The bridge is self-balanced; the bias voltage changes to bring the unbalanced bridge back to a balanced position. Initially, with no microwave power, the power meter bias current heats the thermistor, which brings its resistance in balance with the internal reference resistance (R_o) and, in turn, establish the DC equilibrium. The applied microwave power reduces the thermistor's resistance (increases in the case of the barretter) and disturbs the bridge, causing more current (less in the case of the barretter) to flow through the thermistor. The self-balancing mechanism reduces (increases in the case of the barretter) the DC bias voltage to bring the bridge back to balance. This reduced DC voltage is equivalent to the RF power incident on the thermistor, called the DC substitution.

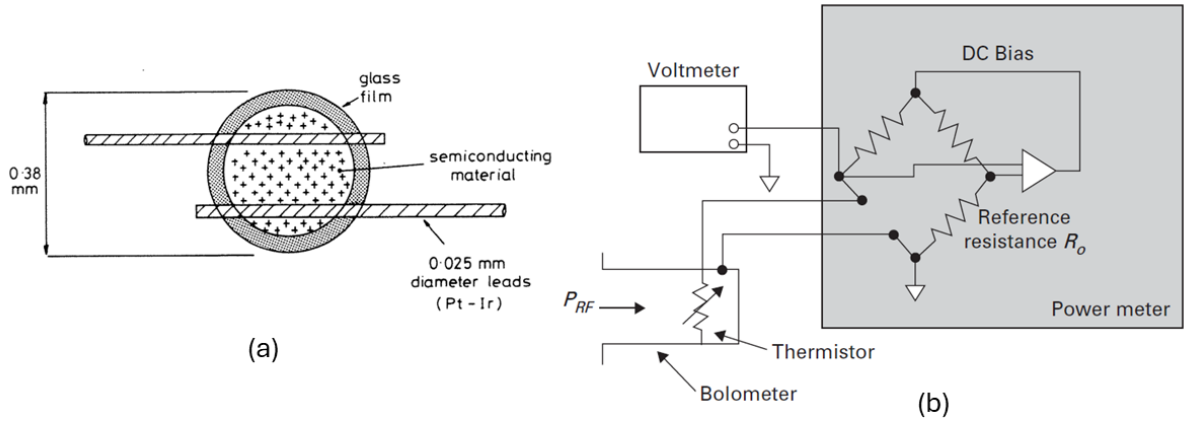

Figure 2.1 (a) Bead thermistor schematic [80] (b) bolometer power detector schematic [81].

Historically, the RF circuit with 50 Ohm load termination is typically designed for coaxial thermistor mount. It consists of two parallel 100 Ohm resistances. However, these resistances are in series for the DC circuit in the power meter, which makes the operating resistance in each branch of the bridge equal a popular number of 200 Ohm [82]. The modern and commercial circuits are designed with operating resistance from 50 to 400 Ohm [83], [84]. So, it is common to design the bolometer element in the waveguide mount with resistance between 200 to 500 Ohm [85], [86], [87].

Thermolectric bolometer:

Thermoelectric bolometers, or thermocouples, are temperature sensors formed from two dissimilar metals attaching both ends. Three interrelated phenomena occur in the thermocouple: the Thomson effect, the Peltier effect, and the Seebeck effect. When one end of the metal rod is heated, the electrons escape the atom and travel towards the other. This process is opposed by Columb’s force of attraction between the diffused electrons and the positive ion left behind. The net electric field inside the metal rod is called Thomson electromotive force. The phenomenon is known as the Thomson effect [80], [82].

Similarly, when two dissimilar metals with different electron densities are connected in a loop, as shown in Figure 2.2 (a), electrons diffuse from a higher-density metal to a lower one, creating an e.m.f. called Peltier e.m.f. Combining the previous two phenomena, heating one junction of the dissimilar metals and keeping the other cold, the net e.m.f. is generated called Seebeck e.m.f. [80], [82].

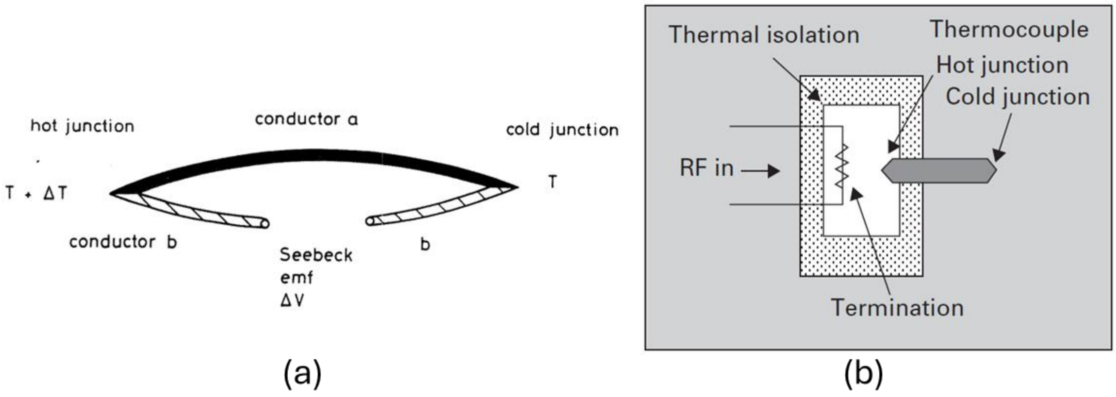

Figure 2.2 (a) Thermocouple element [80] (b) Thermocouple power detector schematic [81].

This e.m.f depends on the temperature gradient between the two junctions, and the concept is used in the power measurement where one of the junctions is kept in contact with the heat absorber, and the other is maintained as a cold junction, as shown in Figure 2.2 (b). The RF power absorbed raises the temperature of the hot junction, giving rise to a proportionate current representing the RF power.

2.1.2 Electronic Detectors

Diode detector:

The diode-based power detectors can be used in applications where absolute power measurement is not necessary. They are used in vector network analysers and communication systems where fast response is necessary. The conventional diode is made of semiconductor p-n junction, which is limited to lower frequencies due to minority charge storage and large junction capacitance. The Schottky diode made of a metal-semiconductor junction is preferred at high frequencies as it is the majority carrier device, and no charge storage occurs. It also has low junction capacitance [88], [89]. The diode has nonlinear current-voltage (IV) characteristics, as shown in Figure 2.3 (a). Change in voltage across the diode changes the current nonlinearly. The typical diode power detector is shown in Figure 2.3 (b). It consists of matching resistance $R_{matching}$ and the RF bypass capacitance (C_b). The RF power going into the diode generates DC current components, creating a voltage drop across the load resistance, which can be measured. The rest of the frequency components are filtered out through C_b. The detected DC voltage relative to input RF power is called the responsivity of the diode power detector, and its unit is V/W or mV/mW. Figure 2.3 (c) shows the detected voltage (V_o) versus the input power curve in which the square law region is from the noise floor of -70 dBm to -20 dBm. Above -20 dBm diode enters into linear region. More is discussed in Chapter 5.

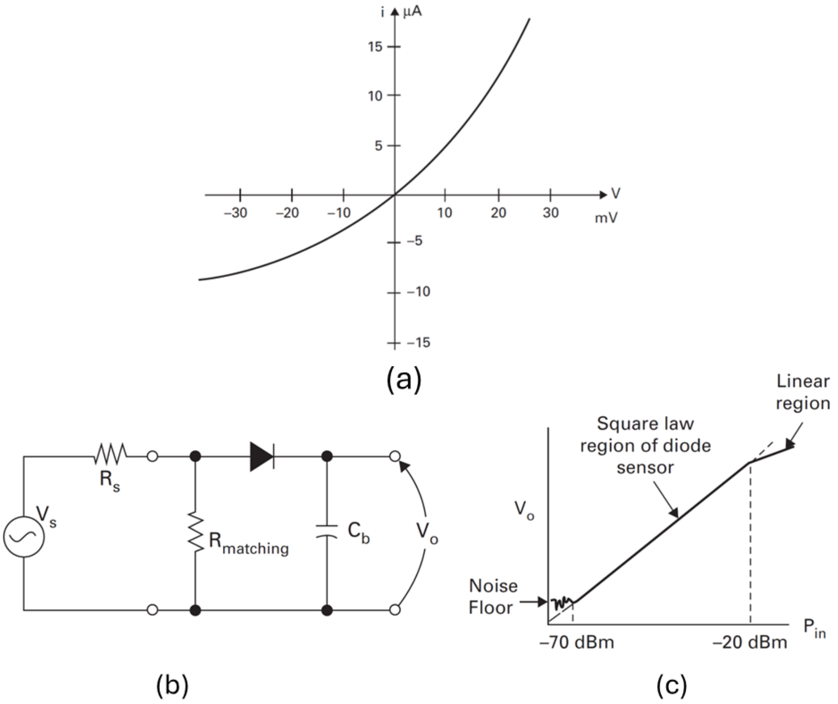

Figure 2.3 (a) Typical current-voltage characteristic of the diode (b) power detector circuit (c) detected voltage versus input power [81], [82].

2.2 Bolometric Power Detector

The basic mounting structure/arrangement of the sensor element (bolometric or thermoelectric) in or around the waveguide can be categorised based on the matching types [90], as shown in Figure 2.4. The first matching type is a resonance match, and the second is a matched load type match. The mount where a sensor element is inserted into the E-plane of the waveguide and becomes part of the matching structure is typically a resonance match. The approach is also called the ‘bolometric technique’ [2] or bolometer mount [91]. It is a narrowband match as the sensing element inside the waveguide modifies the input impedance, which can be matched over a limited frequency and causes reflections to the other frequency. However, the advantage of the resonance match is that the sensor element is relatively thin and has low thermal mass, making it respond fast to the rise in temperature. Scaling up the frequency is challenging as the waveguide size reduces at higher frequencies, increasing the challenges of inserting the sensor element inside the waveguide. The bolometer mount can be a bead thermistor [92] or a thin film with a negative temperature coefficient, identified as a thermistor mount. In contrast, a barrater mount consists of a wire or a thin film [87], [93] with a positive temperature coefficient [91]. The reflection coefficient (Γ or S_{11}) of such mounts depends on the thin film dimension and distance from the back short [85], [93]. In the bolometric approach, the RF energy incident directly on the sensor element and resistance change due to heat is represented/calibrated as incident RF power. Moreover, a thermoelectric sensor (thermocouple/thermopile) can also be placed at the centre of the thin film to calibrate the generated voltage in terms of power [85], [86], [93]. The commercial thin-film barrator mount can be seen in [86], and the thermistor mount in [21].

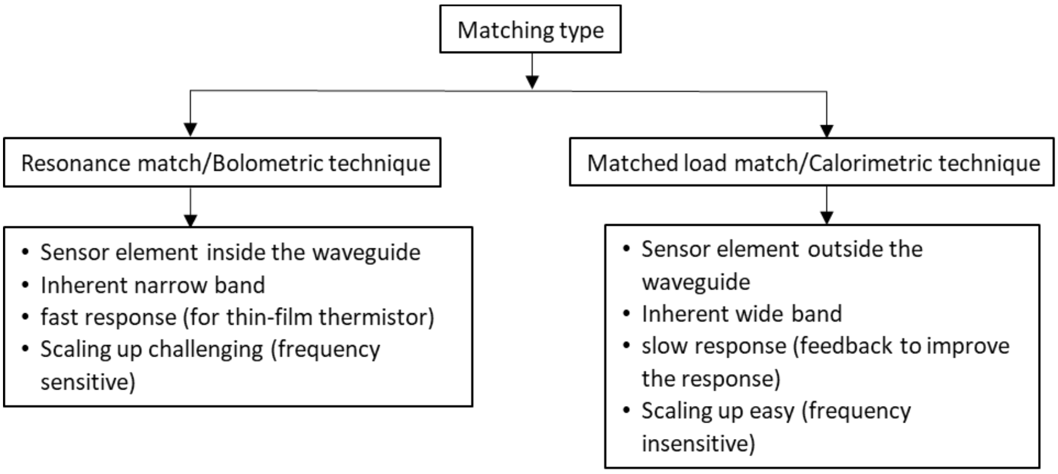

Figure 2.4 Power standard matching types and attributes.

The second type of matching is a matched load type match. The mount where a separate absorber is placed on the waveguide's taper section, which matches the waveguide's input, is called matched load type matching. The sensor element is placed on/around the absorber of the tapered waveguide and is not part of the matching. The approach is also called the 'calorimetric technique' because the heat rise of the absorber is measured [2], [11]. It is a wideband match as the tapered waveguide gradually transforms the waveguide characteristic impedance to the load, the absorber giving a smooth impedance transition over a wider bandwidth. The absorber is large, hence the large thermal mass, which results in a longer response time to heat the absorber and, therefore, a slow response to an instantaneous temperature change. Scaling up the frequency is relatively easy as the sensor element and absorber are outside the waveguide. The sensor element could be bolometric (thermistor [30], thin-film [24]) or thermoelectric [16]; both are widely used on the absorber, as in Table 1.1 of Chapter 1. The reflection coefficient depends on the taper angle and the absorber material. It is frequency insensitive and easier to match than resonance match. Using the calorimetric technique, RF energy is incident on the absorber, not the sensor element, causing its temperature to rise. The sensing element measures this temperature rise and then is represented/calibrated as RF power. The commercial calorimetric power transfer standard using platinum (Pt) thin film can be found in [10], [94] and thermoelectric in [22]. The different types of sensing elements at low and high frequencies in the respective matching types are shown in Figure 2.5. In resonance match, at lower frequencies (<100 GHz), thermistor mounts, thin film and thermocouples are used. Whereas in matched load match at those frequencies, a waterflow calorimeter, absorber with a thermistor, a thin film or thermocouples are used. Waveguide to Coplanar waveguide (W-to-CPW) matched load transition is also used for power measurements. At higher frequencies (>100 GHz), matched load is very common and absorber chip with thin film or thermocouple also W-to-CPW matchd load transition are used. However there is no resonance match technique at higher frequencies, this is the only work based on thin film bolometer.

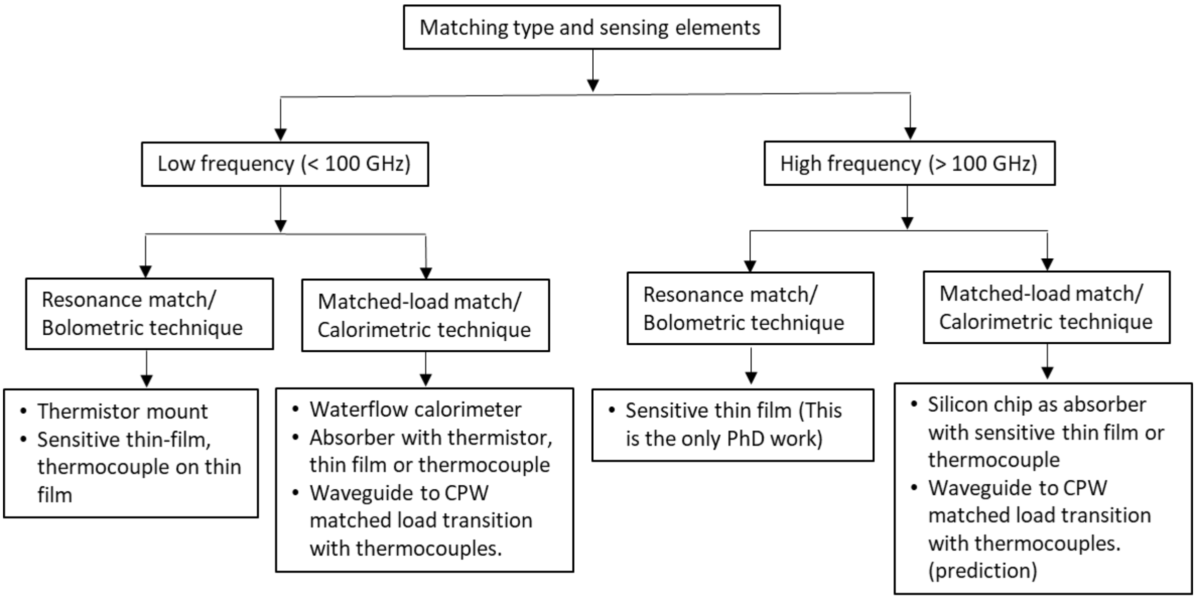

Figure 2.5 Power standard matching type and sensing elements.

The commercial thermistor mounts [21] were available only up to the W-band (75-110 GHz) waveguide in the market due to manufacturing challenges [15], but that was also discontinued [19], [23]. Above 100 GHz, the thermistor beads cannot fit into the waveguide, and losses increase significantly. This has led researchers to create their own power measurement methodologies above 100 GHz [19] based on a calorimetric technique with either thin-film or thermoelectric sensors, as shown in Figure 2.6.

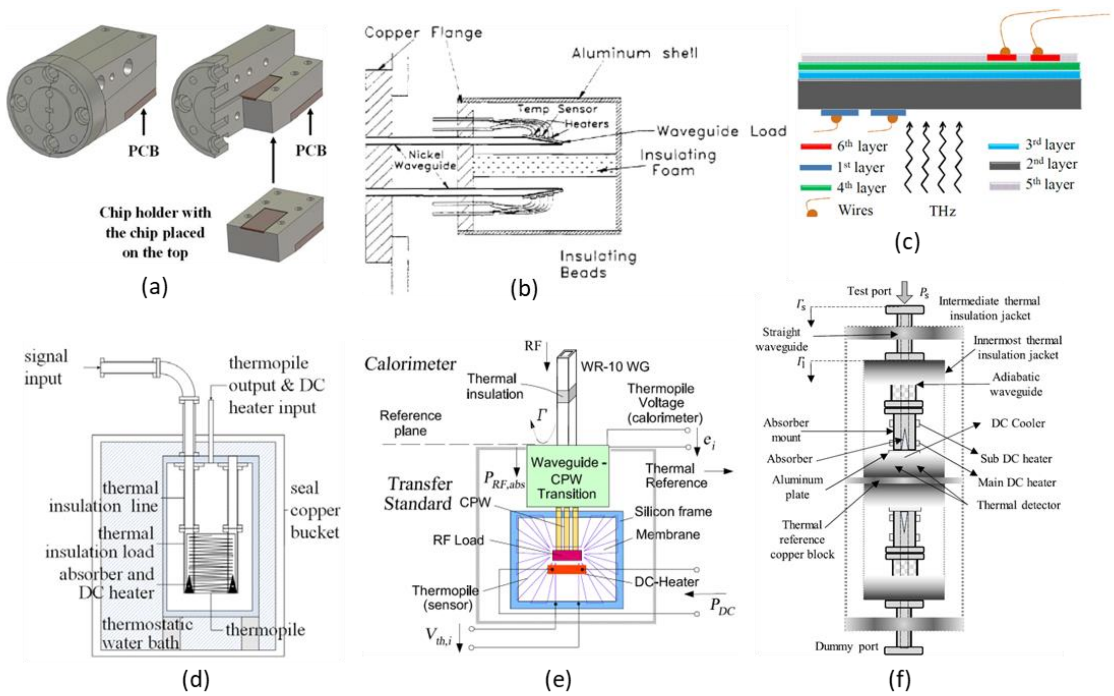

Figure 2.6 Matched load type power sensor (a) silicon chip with thin film sensor on WR06 waveguide taper [24], (b) silicon chip with thin film sensor on WR10 waveguide taper [11], (c) multilayer chip with platinum thin film for WR06 waveguide [25], (d) pyramid shape absorber in WR06 with thermoelectric sensor [27], (e) WR10 waveguide to microstrip (W-to-M) transition with thermoelectric sensor [16], (f) pyramid shape absorber in WR05 with thermoelectric sensor [95].

In Figure 2.6 (a), the silicon chip is placed as an absorber on the tapered waveguide section with a platinum (Pt) thin-film sensor in the WR06 (110-170 GHz) waveguide [24] and WR10 (75-110 GHz) waveguide in Figure 2.6 (b) [11]. The multilayer chip consisting of the RF absorber and Pt thin-film sensor is placed on the taper section of the WR 06 (110-170 GHz) waveguide, as shown in Figure 2.6 (c), to create a reference standard [25]. However, such loads suffer from a large time constant due to poor thermal isolation and large thermal mass, and feedback electronics are involved in improving the response time [11]. The sensor mount in [11] is adopted by commercial Erickson PM1B [19], [94] and their recent VDI-Erickson PM5 [10]. It has the basic mount in the W-band, and waveguide tapers are used to cover the higher frequency bands. ELMIKA has also developed a similar type of commercial power sensor [96].

In Figure 2.6 (d), the pyramid-shaped absorber is inserted into the WR06 [27] and WR05 (140-220 GHz) (Figure 2.6 (f)) [95] waveguide and thermoelectric/thermopile sensors around it, measuring the heat rise with respect to the reference waveguide in [27] or with respect to the reference aluminium plate in [95]. The arrangement in [95] is called a quasi-twin calorimeter [28]. The thermoelectric transfer standard in Figure 2.6 (e) [16] consists of the waveguide (WR10) to coplanar waveguide transition terminated with 50 Ω RF load (two parallel 100 Ω resistors), and thermoelectric sensors measure the heat rise with respect to the surrounding silicon frame. This concept is adopted in commercial Rohde & Schwarz power transfer standards [22].

As discussed earlier, thermistor beads and platinum wire elements in the bolometric technique are challenging to build in the waveguide at frequencies above 100 GHz. Losses reduce the efficiency at millimetre and submillimetre wavelengths [90]. Thermistor mount introduces significant errors in power measurement at high frequencies because of loss in mount structure, lead-wire, tuning screw, and poor contacts [2]. A metallic thin-film sensor element is the only better alternative for high-frequency waveguide resonance-type mounts [97]. Also, the calorimetric technique has matched load absorber design, which, in principle, is limited by their longer settling time due to the large heat capacity (high thermal mass) of the absorber [11], [24], [29]. The bolometer based on thin film, with the highest noted frequency of 94 GHz, was reported in 1985 [87] and shown in Figure 2.7 with other bolometric structures.

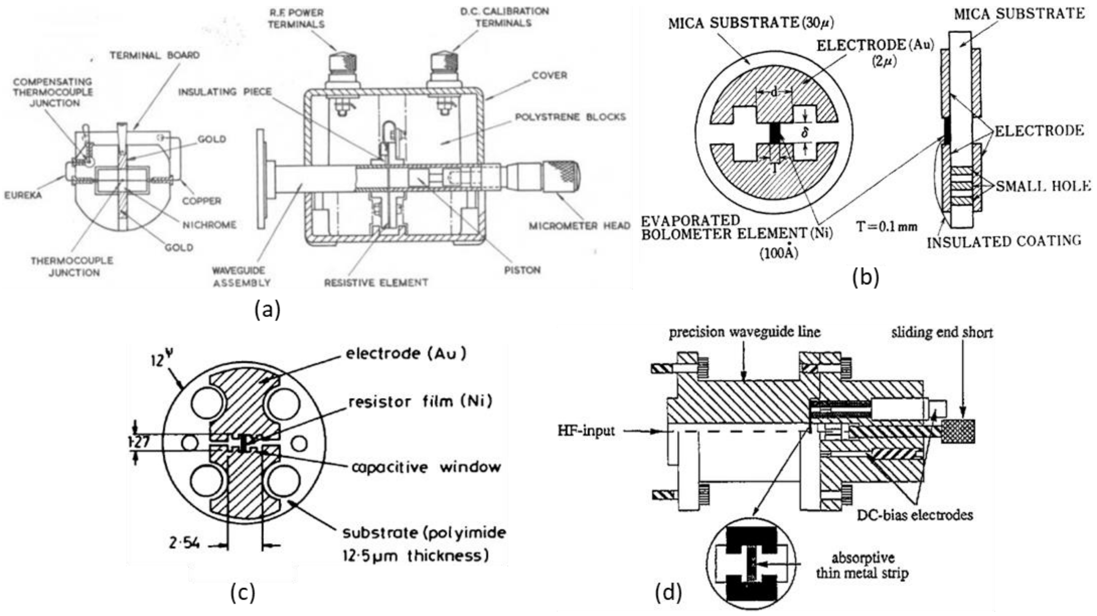

Figure 2.7 Resonance type matching (a) Milliwattmeter working at 8.2-12.4 GHz [86] (b) Re-entrant shape thin film in WR28 (26.5-40 GHz) waveguide [90], (c) Thin film barretter mount along with a capacitive window in WR10 (75-110 GHz) Waveguide [87], (d) Bolometer mount in WR28 (26.5-40 GHz) waveguide [98].

The use of a metallic thin film sensor element in the waveguide was first stated in [93]. The thin film is made by depositing platinum on a mica substrate and gold at the ends for DC contact. The film is placed transversely parallel to the narrow wall of the WR90 (8.2-12.4 GHz) waveguide. This bolometer works at 9.2 GHz and can measure power from 1 to 100 mW. In Figure 2.7 (a), this concept of a thin film bolometer is adopted for the commercial version of milliwattmeters [86] but uses nichrome (NiCr) film on the glass substrate in the WR90 and WR62 (12.4-18 GHz) waveguides. An attempt was made to develop nichrome film for WR28 (26.5-40 GHz) waveguide but could not succeed due to fabrication challenges; hence, a 'resistance card' was used. Nickel (Ni) is used due to its high-temperature coefficient and stability for the thin film on mica, as shown in Figure 2.7 (b) [90], and polyimide (Kapton), as shown in Figure 2.7 (c) and (d) [87], [98] substrates.

The matching of bolometer elements is essential, along with the material choice. Matching solutions to a thin film facing the input port of a waveguide are given in [85], [87], [90], [99]. In [99], the relation between the metallic thin film's reactance and the width is stated. In [85], a matching condition is defined, which states the relation between thin film impedance and back-short length. Many experimental analyses have been conducted in [90] to study the re-entrant shape thin film, a narrow resistive film between the two broad electrodes. The thin film is built in the WR28 (26.5-40 GHz) waveguide, and later, the new designs by replacing it with a bead thermistor between the electrodes experimented. In [87], the capacitive window is designed on the same substrate to cancel the thin film's inductive effect and improve bandwidth. The capacitive window concept is adopted in [97], [98] but at lower frequencies, 26.5-40 GHz. Despite many efforts, the bolometers have still been challenging to achieve the total waveguide bandwidth and used movable back-short to get the optimum reflection coefficient at each frequency at a time. A broadband solution is still required to cover the entire waveguide bandwidth, and the work toward this goal will be covered in Chapter 3.

Table 2.1 compares the power standards intending to cover those above 75 GHz. The sensor's response time needs to be in the seconds range for commercial use of power transfer standards [19], for example, characterising the transceiver system [100], [101]. The sensor's response time is the time required to reach 90 % of the sensor's steady-state value after applying input RF power [91]. The time constant of a thermistor mount is 60-90 min [14] or ~ 60 min [31]. Calorimeter manufacturers have achieved the time constant for the PM1B sensor of 7 s [94] and 0.4 or 0.45 s with the thermal feedback circuit [11], [19]. The VDI-Ericson has a basic sensor time constant of 6 s [102] and 0.2 s with the thermal feedback circuit [10].

Most of the power standards in Table 2.1 are based on matched load. Some lower frequency sensors [33], [86], [93] are also included as examples of resonant-type sensors. However, not all the key parameters (such as settling time) are provided in the literature. Some comparisons may be further qualified depending on the power level and scale used in the measurement. Some of the response time data were taken as an estimate from the figure provided in the literature. The resistances of the sensing element are less than 609 Ω for most of the sensors; only one has 1000 Ω used for the thin film meander line layer. The values of resistances are used as per convenience, as it depends on the measurement setup. It is also a matching problem, especially in the case of resonance matches. The resistance of the sensor element in this research work is 1600 Ω. The commercial sensor's power measurement scale affects the response time as the electronics around the sensor modify the feedback and offsets to reduce the response time and the noise.

Table 2.1 Power standards comparison.

Ref. Year	**Freq (GHz)**	**Time (s)**	**Resistance (Ω)**	**Matching Type**	**Remarks**
This work	110-170	< 2.6	1600	Resonance	90% Response time; Bolometric Transfer Standard; Input power ~ 22.5 mW
[24] 2022	110-170	2400	205.5	Matched Load	Rise Time; Microcalorimeter; Input power ~ 31.5 mW
[95] 2021	140-220	~300	-	Matched Load	90% Response time (graph); Calorimetric; Reference Standard
[25] 2018	110-170	-	1000	Matched Load	Calorimeter element
[33] 2018	50-75	-	200	Resonance	Calorimeter; Thermistor mount
[26] 2018	75-110	-	-	Matched Load	Calorimeter using VDI Erickson PM5
[27] 2017	110-170	-	-	Matched Load	Calorimeter; Thermocouple
[10] 2016	75-110	0.2	-	Matched Load	90% Response time (20 mW scale); VDI Erickson PM5 with feedback
[20] 2015	75-110	-	50	Matched Load	Calorimetric Transfer Standard; Waveguide to CPW Transition
[30] 2015	110-170	-	-	Matched Load	Microcalorimeter
[31] 2010	75-110	~ 3000	-	Resonance	90% Time constant (graph); Thermistor Mount
[35] 2006	110-170	30	-	Matched Load	Response time (at 5 mW); Calorimeter with Feedback
[19] 2006	75-110	0.4	-	Matched Load	90% Response time (scale 20 mW); Calorimeter PM1B with feedback
[11] 1999	75-110	0.45	-	Matched Load	Time constant (scale 20 mW); Calorimeter with Feedback
[103] 1974	60-90	< 0.8	200	Matched Load	Response time of practical transducer; Thermocouple at resistive strip
[86] 1960	26.5-40	~ 15	609	Resonance	Time constant; Bolometer-Milliwatmeter
[93] 1958	8.20-12.40	15, 3	480-500	Resonance	Time constant of system (≥ 10 mW); 9.2 GHz; Thermocouple at the centre of film

The power transfer standard is required for absolute power measurement for metrology and device/system characterisation purposes above 100 GHz with a shorter response time of less than a few seconds.

2.3 Diode Power Detector

Power detection using a nonlinear electronic device is common in applications where absolute power measurement is unnecessary. As shown in Figure 2.8, the electronic power detectors can be active or passive. The square-law characteristics of the diode and transistor (at the Base-Emitter junction in the case of CMOS, complementary metal oxide semiconductor, and Gate contact in the case of HEMT, high-electron-mobility transistor) are used for power detection purposes. Transistor-based power detection can be active or passive. The active is when the transistor is used with the operating point near pinch-off or threshold voltage. The passive is when the transistor is modified to two terminal devices, where the Gate acts as an anode, and the Source and Drain are connected to form a cathode [104]. The HEMT power detector circuit in active or passive types can be found in [54], requiring biasing. Zero-bias passive power detectors based on HEMT technology can be seen in [50]. The CMOS transistor-based active power detectors are in [62], [105], [106]. However, transistor-based detectors have complex circuits and need biasing. Also, transistors above 100 GHz are rare due to technological challenges at those frequencies. The diode-based power detector comes under the passive type. It has a simple circuit, and biasing is not always necessary.

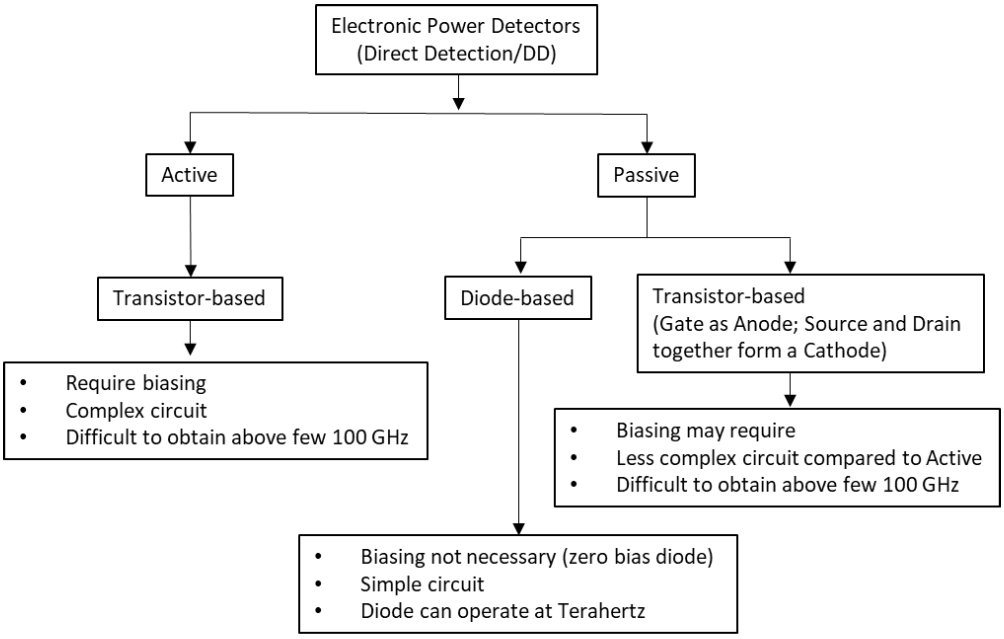

Figure 2.8 Electronic power detectors and their main attributes.

Electronic components/devices suffer from parasitic loss as the wavelength becomes comparable to their dimension at higher frequencies. In the case of the Schottky diode, it has junction capacitance, junction (dynamic/differential) resistance, and series resistance as the core of the equivalent circuit and then the parasitic capacitance and inductance arising from the physical structure of the diode. More details on this will be covered in Chapter 5. The diode's junction capacitance and junction resistance are utilised for the multiplication and the detection application, respectively. The junction resistance is typically in the order of a few hundred Ω [107]. Therefore, matching the 50 Ω transmission line to the high input impedance and the parasitics becomes difficult. Matching is necessary to transfer the maximum input power to the junction resistance for detection. It is important to mention that the performance of the diode-based device depends not only on the external circuit but also on the diode structure. Techniques to reduce the parasitic have been extensively studied [5]. The matching can be divided into resistive and reactive [108], [109], as shown in Figure 2.9. The resistive matching uses a resistor parallel to the diode at the input; this gives a wideband frequency response but affects the detector's responsivity. Reactive matching uses capacitors, inductors, stubs, and impedance transformers. This gives a narrow-band frequency response, but responsivity is comparatively higher than the resistive match. The components in the matching circuit could be lumped elements or distributive elements depending on the frequency, size constraints and cost [108], [110].

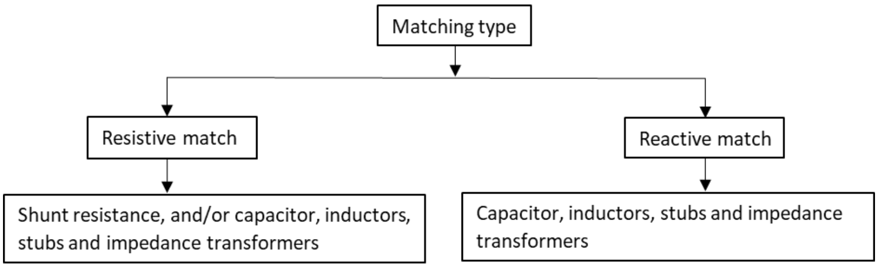

Figure 2.9 Electronic power detectors matching types.

As discussed in Chapter 1, the power detector circuit can be for PCB/MMIC-based- or waveguide-based applications. The power detector circuits on PCB/MMIC for two matching types are shown in Figure 2.10. The lumped elements (capacitors or inductors) are rare in the matching circuit at the input of the diode-based detectors. The detectors have distributive elements such as taper lines, radial stubs, open stubs, quarter-wave impedance transformers, and short stubs, all with various combinations. In Figure 2.10 (a) and (b), the lumped elements at the input are shunt resistors in the resistive match [59], [111], except for an additional coil (inductor) used in [112]. In [111] and [112], they have a 51 Ω SMD (surface mount device) resister and 50 Ω thin film resistor (placed in a unique T-shape arrangement), respectively, that helps with matching and also serves as a DC return path. However, [59] has a 100 Ω thin film resistor (titanium oxide layer with a sheet resistance of 100 Ω/Sq) for matching, and a separate high-impedance quarter-wavelength (λ/4) shorted line through radial stubs provides the return path. In Figure 2.10 (d), a lumped element at the input of the diode-based power detector [57], which is a MIM (metal-insulator-metal) capacitor; however, it is used for RF coupling, not matching. The current return path is required at the input of the detector to form a complete DC closed loop to have the voltage drop across the load resistance. The return path in [58] is maintained by shorting the diode's cathode. In Figure 2.10 (c) [57], it is provided through a high-impedance line with a pad at the end for connection.

The detector consists of a lowpass filter (LPF) at the output to block/short the undesired high frequencies from the diode and only read the detected DC voltage. The filters can be just a single (Figure 2.10 (a)) [111] or multiple capacitors with a coil [112], a type of CMRC (compact microstrip resonant cell) filter (Figure 2.10 (d)) [57], a pair of quarter-wave reflectors (Figure 2.10 (b)) [59] and just a thin film RF choke (Figure 2.10 (c)) [58]. The RF choke (inductor) in [58] is realised using a nichrome (NiCr) thin film resistor, preferred over the spiral choke (inductor), due to size restriction. It has a sheet resistance of 100 Ω/Sq, and the measured total resistance is ~ 8 kΩ.

The DC voltage is measured across output load resistance, which can be on board or external (resistance of voltmeter, typically 1 MΩ), depending on the requirement. The SMD (surface mount device) resistor is used in [111], a thin film resistor of 4 kΩ in [59], a metal film resistor of 500 kΩ [58] and no load resistors in [57], [112].

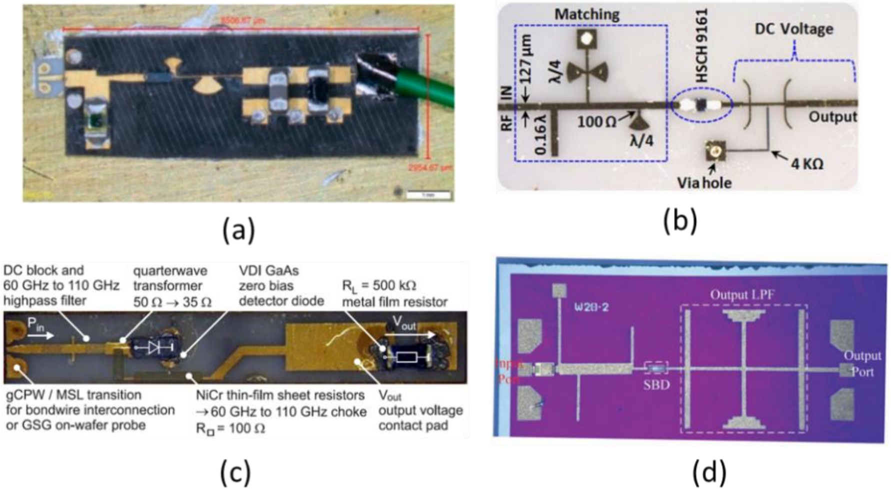

(a) (b)

(c) (d)

Figure 2.10 PCB/MMIC-based diode power detectors (a) resistive match serving return path [111], (b) resistive match with separate return path [59], (c) reactive match with cathode shorted [58], (d) reactive match and MIM coupling capacitor at the input [57].

The Schottky diode power detectors are also implemented in waveguide-based applications. In these devices, RF power is coupled to the detector circuit using a waveguide to microstrip (W-to-M) transition consisting of a probe in the E-plane of the waveguide at approximately λ/4 distance from back-short. The transition can be a microstrip probe or a fin-line. The size of the substrate, hence the available design space, depends on the W-to-M transition structure. The substrate size can sometimes be larger to accommodate the circuit elements. The T-shape substrate is used in the WR28 (26.5-40 GHz) waveguide [113], and a large round substrate in the WR12 (60-90 GHz) waveguide [114].

Detectors with two matching types are shown in Figure 2.10. Resistive matching is rare in waveguide-based detectors. The resistive match in Figure 2.10 (a) used a NiCr thin-film (100 nm thick) shunt resistor and radial stubs [43], [107]. It should be noted that this particular detector is designed for meteorology applications where partial temperature compensation is achieved with another NiCr thin film resistor in series with the diode, which also contributes to matching. The reactive matching in Figure 2.10 (b) prefers impedance transformers and radial stubs but no transmission line stubs (short/open) due to size limitations. Lumped elements such as capacitors and inductors are not preferred because of parasitic losses and size limitations. Lumped elements are seen in transistor-based power detectors where the MMIC process allows MIM capacitors and planar inductors. However, they are not very common for waveguide-based power detectors, possibly due to the fabrication cost and complexity, and they might need biasing. So, a waveguide-based detector circuit has only a handful of options.

In the W-to-M probe transition, the current return path (CRP) can be achieved by protruding/extending the substrate to the bottom wall of the waveguide [115] or parallel (to diode) high impedance (inductive) line on the RF main line as shown in Figure 2.10 (a) and (b) [43], [56] or shorting the cathode of the diode (rectifier circuit) [113]. The detectors having fin-line W-to-M transitions [45], [46] can also have a DC return path by shorting the fins to the waveguide wall [116], [117]. The output filters are mostly stepped impedance [45], [115], CMRC [56], and radial stub filters [46], [113], [114], [118].

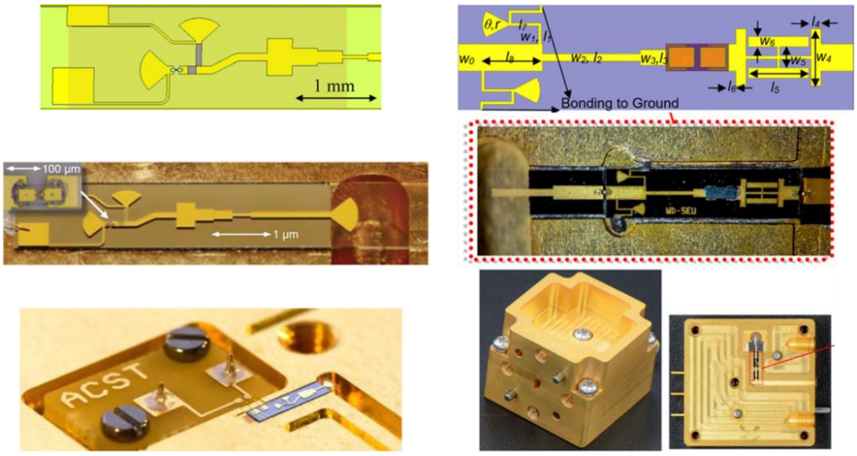

(a) (b)

Figure 2.11 Waveguide-based diode power detectors (a) resistive match [43], [73], [107], (b) reactive match [56].

The waveguide-based power detectors are summarised in Table 2.2, comparing the diode used, frequency band, return loss and responsivity. The reported power detectors mainly operate in the W-

Table 2.2 Waveguide-based diode power detectors comparison.

Reference	**Diode used**	**Frequency (GHz)**	**Return Loss (dB)**	**Responsivity (V/W)**	**Responsivity Difference (V/W)**
This work	Teratech ZBD	D-band	> 2.5	1900-9000 @ -20 dBm, 130 – 160 GHz	7100
[119]	VDI ZBD	D-band	-	2500-4000 (graph)	1500
[120]	Aeroflex MZBD-9161 GaAs	D-band	4 (typical)	Typical 600, Highest 1600	~1600
		W-band	5 (typical)	2000-11800 @ 80 – 104 GHz	~9800
[115]	InGaAs/InP SBD	340-400	-	100-800 (graph)	700
[53]	ZBD	315-357	-	910~2210	1300
[52]	InGaAs ZBD	W-band	-	800-3000 (graph) @ 75-105 GHz	2200
[43]	ACST ZBD	78-97	> 10	8600 @-30dBm, 89 GHz (amplification gain = 10)	-
[118]	Sb-heterostructure InAs/GaAlSb	W-band	-	2000-11000 (graph)	~9000
[121]	Aeroflex/Metelics MZBD-9161	W-band	-	125-1000 (graph)	875
[56]	VDI ZBD	W-band	~ 4.4 (Smith chart, $\Gamma = 0.6$)	6000-9500 @-30 dBm	3500
[122]	Agilent HSCH-9161 GaAs	W-band	~ 3 (graph)	>1000 for 75 to 104.5 GHz Peak 3800 @ 88.5 GHz 500-3800 over full band	3300
[123]	VDI ZBD	W-band	~ 4 (graph)	>1000 for 80 ~ 100 GHz 500 – 7000 over full band	6500
[124]	Agilent HSCH-9161 GaAs	W-band	> 7 (graph, 88-104 GHz)	> 550	-
[125]	HSCH-9161 GaAs	W-band	13.87 (@ 94.6 GHz)	850 for 84 – 102 GHz Peak 2200 @ 94 GHz 600-2200 over full band	1600

band or below and only a few in the D-band. Some of the return loss and responsivity data are taken as an estimate from graphs provided in the literature. The return loss for most of the detectors is less than 10 dB, and the typical value is around 4 dB. Two detectors are working above 300 GHz; one has a responsivity of 800 V/W at around 381 GHz, and the other has 1200 V/W at around 332 GHz, respectively. The Virginia Diodes (VDI)'s detector operating in the D-band (110 - 170 GHz) has the highest reported responsivity of 4000 V/W. The last column shows the difference between maximum and minimum responsivity, and it should be as small as possible to reduce frequency dependence. The commercial Virginia Diodes (VDI) detector has a responsivity difference of 1500 V/W. In W-band, the highest responsivity can be seen as 9800 V/W.

The detector presented in this work has a responsivity of between 1900 V/W and 9000 V/W for frequencies 130 to 160 GHz. The responsivity of the designed detector is higher (9000 V/W) at lower frequencies; however, the difference between maximum and minimum responsivity is large (7100 V/W).

Applications are emerging in D-band, such as waveguide-based compact six-port technology [12], waveguide filters [126], and horn antenna arrays [127]. There is a need for a power detector above 100 GHz with a typical responsivity of at least 1000 V/W [78].

2.4 Summary

It is seen that absolute power measurement techniques are struggling to achieve traceability above 100 GHz, and individuals are coming up with their own variations of the calorimetric power detection method but suffer long response times, and some are bulky in size. The commercial calorimetric power meter PM5 has been the only transfer standard with a response time of 0.2 sec improved by external feedback electronics. This work focuses on developing alternative portable transfer standards using bolometric techniques. Chapter 3 discusses the theoretical aspect and is the base for Chapter 4, where the power standard is realised.

For non-metrology applications, it is seen that the electronic power detector can be realised in transistors and diodes. However, the transistor power detector is only used in PCB/MMIC-based applications. Diode power detectors can be found in both PCB/MMIC and waveguide-based applications. The diode power detectors are simple, cheaper than transistor-based and widely used. The detectors in the D-band application require a minimum responsivity of 1000 V/W. Therefore, this work will also investigate diode power detectors for waveguide-based applications. Details will be reported in Chapter 5.

CHAPTER 3

THIN FILM IN A WAVEGUIDE

This chapter focuses on the theoretical aspect of thin metallic film/line in the E-plane of the waveguide. It starts with the basics of the waveguide and thin film, then discusses the design of a single line in the waveguide using equivalent circuit analysis. The double line structure is then introduced for wider bandwidth, and the validation is done using the equivalent circuit. In the end, the material choices for thin film are discussed.

3.1 Rectangular Waveguide

A rectangular waveguide is a hollow metallic structure which can carry electromagnetic energy. They are used at the microwave and higher frequencies. At lower frequencies, current travels through the conductor cross-section. However, as frequency increases, the current starts flowing over the conductor's surface with penetration equal to skin depth [128]. A low skin depth would effectively mean a low cross-section area, causing a higher loss in the conductor. The waveguide is a hollow structure with a large surface area, so there is lower loss at these frequencies. Figure 3.1 shows a schematic of a rectangular waveguide.

The rectangular waveguide does not carry transverse electromagnetic (TEM) mode and DC signal as it is a single hollow conductor. Only transverse electric (TE_{mn}) and the transverse magnetic modes (TM_{mn}) travels through the waveguide. A waveguide's broader wall (width) is on the x-axis, the narrow wall (height) is on the y-axis, and the waveguide length is on the z-axis. The subscript m and n indicate the number of half wavelengths in the x and y direction, respectively. The TE_{10} is the dominant or fundamental mode with the lowest cut-off frequency and is commonly used in practice.

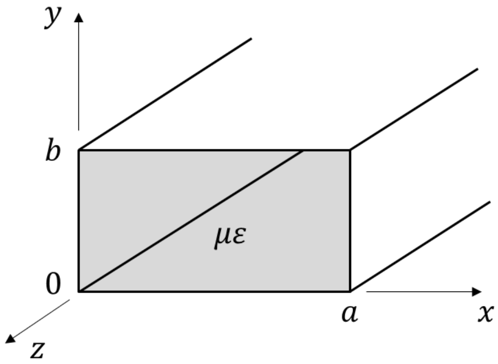

Figure 3.1 Rectangular waveguide, adapted from [128].

The general formula for cut-off frequency in the rectangular waveguide is given by [128],

$$f_c = \frac{1}{2\sqrt{\mu\varepsilon}}\sqrt{\left(\frac{m}{a}\right)^2 + \left(\frac{n}{b}\right)^2} \tag{3.1}$$

where a is the width of the waveguide, b is the height of the waveguide, μ is the permeability of the material, and ε is the permittivity of the material. In free space $\frac{1}{\sqrt{\mu\varepsilon}}$ becomes equal to the speed of light (c).

The propagation constant in a waveguide can be expressed as [128],

$$\beta = \sqrt{k^2 - \left(\frac{m\pi}{a}\right)^2 - \left(\frac{n\pi}{b}\right)^2} \tag{3.2}$$

where $k = \omega\sqrt{\mu\varepsilon}$, is a propagation constant of the medium. In free space $k = \frac{\omega}{c}$, where c is the speed of light in free space.

The guided wavelength is the wavelength in the waveguide different from the free space and can be calculated as follows,

$$\lambda_g = \frac{2\pi}{\beta} \tag{3.3}$$

The characteristic impedance of the waveguide is [128],

$$Z_g = \frac{k\eta}{\beta} \tag{3.4}$$

where, $\eta = \sqrt{\frac{\mu}{\varepsilon}}$ is the intrinsic impedance of the material inside the waveguide.

3.2 Thin Film and Sheet Resistance

The object with one of the dimensions infinitesimally smaller or negligible than the other two is called a 'Sheet' or a 'Film', and the smallest dimension is the thickness, as depicted in Figure 3.2. The application of the sheet depends on the material and its characteristics. For example, the flexible plastic thin film is used for biomedical applications [129], and the transparent oxide thin film is used for LCD (liquid crystal display) touchscreen displays [130]. The resistive thin film is used for bolometric power detection devices, as discussed in Chapter 2.

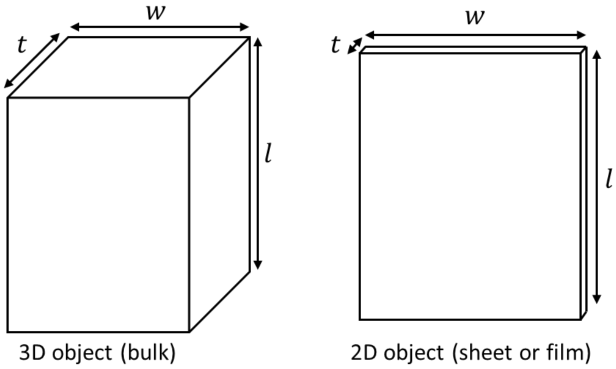

Figure 3.2 Sketch of 3D (three-dimensional) and 2D (two-dimensional) objects.

The electrical characteristic of resistive bulk material is defined using conductivity (σ) or resistivity ($\rho = 1/\sigma$), while the resistive film is defined using sheet resistance (R_S). The sheet resistance depends on the thickness (t) of the sheet and the material used. The other two dimensions, the width (w) and the length (l), can give the total resistance (R) of the film. The sheet resistance (R_S) and the total resistance (R) of the thin metallic film can be calculated as [131],

$$R_S = \rho \cdot \frac{1}{t} \tag{3.5}$$

$$R = \rho \cdot \frac{l}{A} = \rho \cdot \frac{l}{w \cdot t} = R_S \cdot \frac{l}{w} \tag{3.6}$$

where A is the cross-section area of the conductor, in this case, the thin film when current flowing along its length.

3.3 Single Line Thin Film Design

A thin film can be placed in the E-plane of the waveguide facing the input port or the narrow side wall, as shown in Figure 3.3. A thin film in the E-plane of the waveguide at an approximately quarter wavelength from the back-short gives a resonance match. The solution for a single thin film facing toward the input port in the E-plane is given in [85]. In this thesis, the same solution is applied to a narrow wall-facing configuration. This is one of the novelties. Thin film mounts in waveguides were unpopular mainly because the waveguide got much smaller, above 100 GHz, increasing fabrication challenges, as discussed in Section 2.2. The last thin film structure (facing input port) reported was in 1985, working at 95 GHz. This new configuration allows adding more than one film in the same plane to improve bandwidth, which is covered later in Section 3.5. The equivalent circuit of a thin film in a waveguide is shown in Figure 3.3 (c). The thin film acts as an inductor of reactance *X* and resistance *R* parallel to the input port.

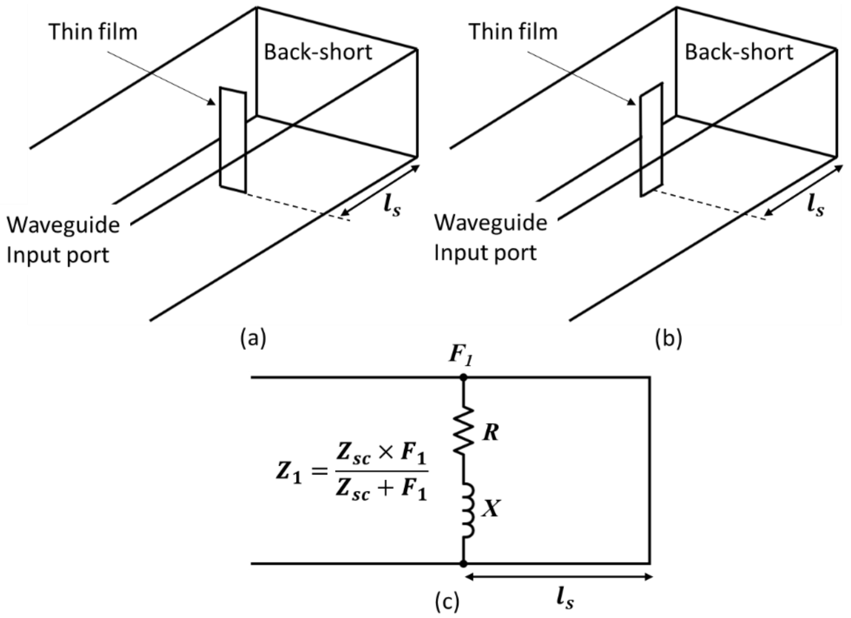

Figure 3.3 Thin film in a waveguide (a) facing input port, (b) facing narrow side wall, (c) equivalent circuit of the thin film in the waveguide.

The general equation of transmission line (TL) input impedance is [128],

$$Z_{in} = Z_0 \frac{Z_L + j \cdot Z_0 tan(\beta l)}{Z_0 + j \cdot Z_L tan(\beta l)} \tag{3.7}$$

where Z_0 is the characteristic impedance of the TL, Z_L is the load, β is the propagation constant, and l is the length of the TL.

Equation (3.7) for the special case of shorted waveguide having short circuit impedance Z_{SC} at a distance l_S from the shorted end of the waveguide is,

$$Z_{sc} = +j \cdot Z_0 tan(\beta l_S) \tag{3.8}$$

where Z_0 $(= Z_g)$ is the characteristic impedance of the waveguide, β is the guided propagation constant.

The equivalent impedance after adding the thin film at a distance of l_S from the back-short is,

$$Z_1 = Z_{sc} \parallel F_1 = \frac{Z_{sc} \times F_1}{Z_{sc} + F_1} = \frac{Z_{sc} \times (R + j \cdot X)}{Z_{sc} + R + j \cdot X} \tag{3.9}$$

where F_1 $(= R + jX)$ is the impedance of the thin film impedance.

Equation (3.9) can be simplified to get real and imaginary parts separately,

$$Z_1 = \frac{Z_{sc}^2 \cdot R}{R^2 + (X + Z_{sc})^2} + j \cdot \frac{Z_{sc} \cdot R^2 + Z_{sc} \cdot X^2 + Z_{sc}^2 \cdot X}{R^2 + (X + Z_{sc})^2} \tag{3.10}$$

To get no reflection at the input port, the equivalent impedance Z_1 must equal the waveguide's characteristic impedance. This results in two matching conditions: firstly, the real part of (3.10) must be equal to the waveguide's characteristic impedance and secondly, the imaginary part to zero. Equating the imaginary term of (3.10) to zero gives,

$$Z_{sc} = \frac{-(R^2 + X^2)}{X} \tag{3.11}$$

Equating the real term of (3.10) to characteristic impedance and using (3.11) gives,

$$Z_0 = \frac{Z_{sc}^2 \cdot R}{R^2 + (X + Z_{sc})^2} = \frac{R^2 + X^2}{R} \tag{3.12}$$

From (3.8), (3.11), and (3.12), an important relationship is obtained between the back-short length and the impedance of thin film as,

$$\tan(\beta l_s) = \frac{-R}{X} \tag{3.13}$$

The thin film in the waveguide can be designed using the process shown in Figure 3.4. The first step is essential as the DC resistance of the sensor element (thin film or thermistor) connected to the self-balancing bridge circuit is typically 200 Ω [97], [4]. The thin film resistance used in [85], [86], and [87] is between 200 Ω and 500 Ω.

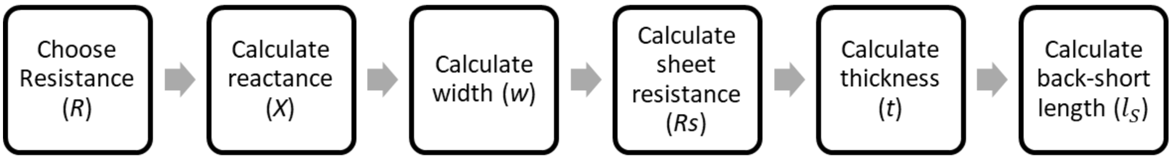

Figure 3.4 Flow chart for the single-line design.

The reactance (*X*) of the film can be calculated by (3.12) for the required thin film resistance (*R*). The relation between the reactance (*X*) and the width (*w*) of the thin film when placed in the E-plane of the waveguide is [99],

$$\frac{X}{Z_0} \approx \frac{a}{2\lambda_g}\left[\ln\left(\frac{8}{\pi e^2}\frac{a}{w}\right) + \frac{4}{27}\left(\frac{a}{\lambda}\right)^2\right], \qquad \{\mathrm{w/a} \le 0.15 \text{ and } \mathrm{a}/\lambda \le 1\} \qquad (3.14)$$

where $\lambda = \frac{2\pi}{\mathrm{k}}$ is the wavelength in free space.

The sheet resistance (R_S) for the thin film of width (*w*) can be calculated by (3.6), where the length (*l*) of the thin film inside the waveguide is equal to the height of the waveguide (*b*). The film thickness (*t*) can be calculated depending on material conductivity using (3.5). In the end, as the reactance and resistance of the thin film are known, the back-short length (l_S) can be calculated by (3.13). The value of the calculated back short length may come much smaller, closer to the waveguide shorted end; in that case, an integer multiple of half-guided wavelength can be added.

All the parameters discussed in the design process are calculated for four resistances (100 Ω, 200 Ω, 300 Ω, and 400 Ω) at 140 GHz (D-band centre frequency), as detailed in Table 3.1. The D-band standard WR6 waveguide dimensions (*a* = 1.651 mm *b* = 0.8255 mm) are used in the calculation. Platinum material is currently considered for thickness estimation; more materials will be covered in Section 3.7. It is seen that the sheet resistance, thickness, and back short lengths are smaller for higher resistances.

Table 3.1 Calculated design parameters for four different resistances at 140 GHz.

Chosen Film resistance (Ω)	100	200	300	400
Width (µm)	152.23	112.26	112.98	155.85
Sheet Resistance (Ω/Sq)	18.4	27.2	41	75.5
Film Thickness (Platinum) (nm)	6	5	2.6	1.4
Back-short length (µm)	1199.4	1100	1009	908

The trend of width initially being high, then reducing and again increasing, is due to the matching condition in (3.12). To understand this, the X versus R graph is plotted as shown in Figure 3.5 for the waveguide characteristic impedance (Z_0) of 495 Ω (at 140 GHz), and the thin film resistance R varied from 0 to 495 Ω. The trend shows that the X increases as R value increases until 250 Ohm, and then above 250 Ω, the X values decrease. The w versus R value is also plotted, showing the opposite trend; as the R increases, the width decreases to the lowest value, 108.73 µm and above 250 Ω, the width starts increasing.

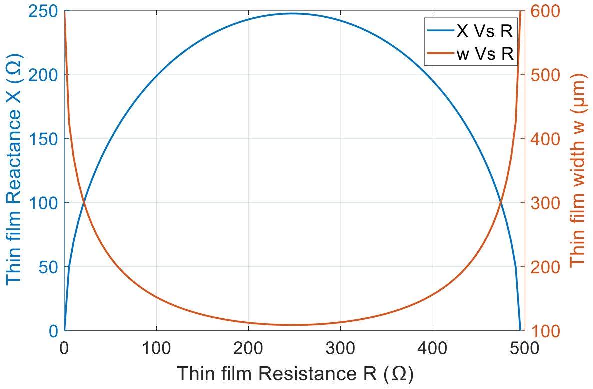

Figure 3.5 Fig A Reactance Vs Resistance and Width Vs Resistance plot.

The thin film structure with two different orientations, one facing towards the input port and the other towards the narrow wall, is investigated in the CST (Computer Simulation Technology) Microwave Studio, as shown in Figure 3.6. The substrate used in all the simulations in this chapter has relative permittivity (ε_r) of 4.2 and a thickness of 50 µm. The waveguide is extended one guided wavelength from the centre of the thin film to the input port.

Each design is simulated for different sheet resistance values from Table 3.1. From the initial simulation using the calculated parameters, the minima of the reflection coefficient were not at the designed (central) frequency of 140 GHz in both cases of the thin film-facing input port and narrow wall. The offset in S_{11} minima from the design frequency of 140 GHz can be attributed to the equivalent circuit equation used to design the structure, especially (3.14), which is an approximation. The effect of substrate is not significant here. The back short length has to be varied to get the minima at the centre of the D-band. The values of back-short lengths before and after optimisation in Table 3.2 are the same for both cases (film-facing input port and narrow wall), and their difference shows that mathematical equations used in the design could not give precise results. The film resistance (R) changes if the width is optimised; therefore, sheet resistance (R_S) is preferred (which is independent of the width) to compare the graphs.

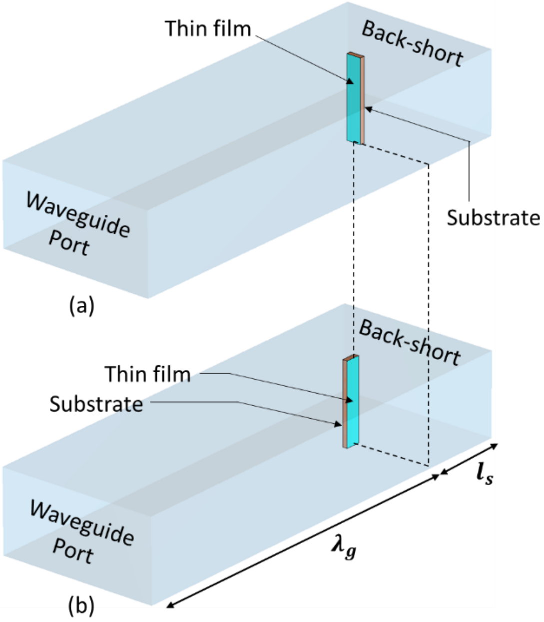

Figure 3.6 Single thin film in a waveguide (a) facing the input port, (b) facing the narrow side wall.

Table 3.2 Back-short lengths (l_S) before and after optimisation.

	l_S before optimisation (μm)	l_S after optimisation (μm)	Difference (μm)
R_S = 18.4 Ω/Sq	1199	1178	-21 (-1.75 %)
R_S = 27.2 Ω/Sq	1100	1084	-16 (-1.45 %)
R_S = 41.0 Ω/Sq	1009	994	-15 (-1.5 %)
R_S = 75.5 Ω/Sq	908	892	-16 (1.76 %)

The reflection coefficient (S_{11}) plotted for the thin film facing toward the input port for two sheet resistances 27.2 Ω/Sq and 75.5 Ω/Sq, as shown in Figure 3.7 (a). The minimas of S_{11} before optimisation are slightly away from the centre of the D-band (140 GHz). The S_{11} is better at 75.5 Ω/Sq compared to 27.2 Ω/Sq. Figure 3.7 (b) shows the same plots for the film facing the narrow wall of the waveguide. It is seen from Figure 3.7 (a) and (b) that the design equations (3.12)- (3.14) can be used for both the film structures (facing input port and narrow wall). This is because the electric field is parallel to the film in either case, giving a similar S_{11} response.

The reflection coefficients (S_{11}) for the four different sheet resistances (18.4 Ω/Sq, 27.2 Ω/Sq, 41.0 Ω/Sq, and 75.5 Ω/Sq) are shown in Figure 3.8. It is observed that the S_{11} at the centre frequency reduces as the film resistance (R) or sheet resistance (R_S) increases. This is because higher sheet resistance thin film has large attenuation to the resonating current on the thin film, giving rise to less reflection of the RF power.

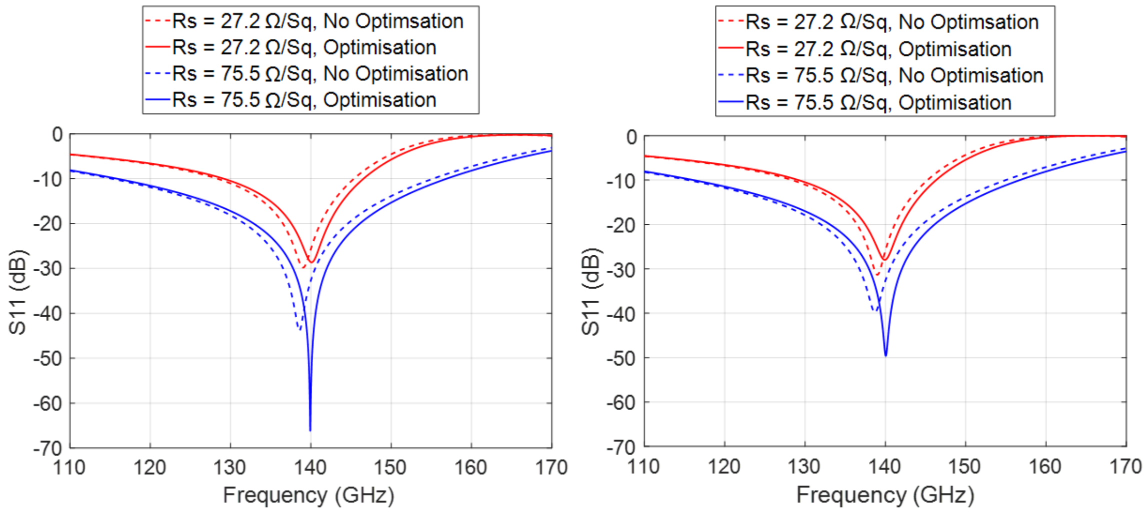

(a) (b)

Figure 3.7 S_{11} of the film (a) facing the input port of the waveguide, (b) facing the narrow wall of the waveguide.

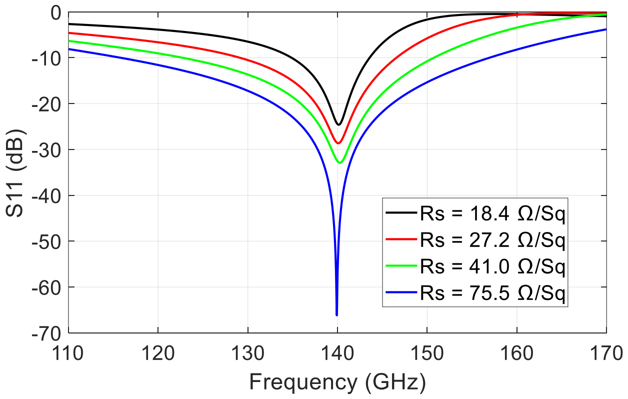

Figure 3.8 S_{11} of the single thin film facing the narrow wall.

The effect of substrate thickness on the reflection coefficient is investigated. The substrate thickness (SubT) is increased to 200 μm in steps of 50 μm. In Figure 3.9, it is observed that, in both cases (film facing the narrow wall and the port), the minima in the reflection coefficient shifts to a lower frequency from the centre (140 GHz). This is due to an increase in the capacitance after adding the excessive substrate inside the waveguide, which lowers the resonance frequency.

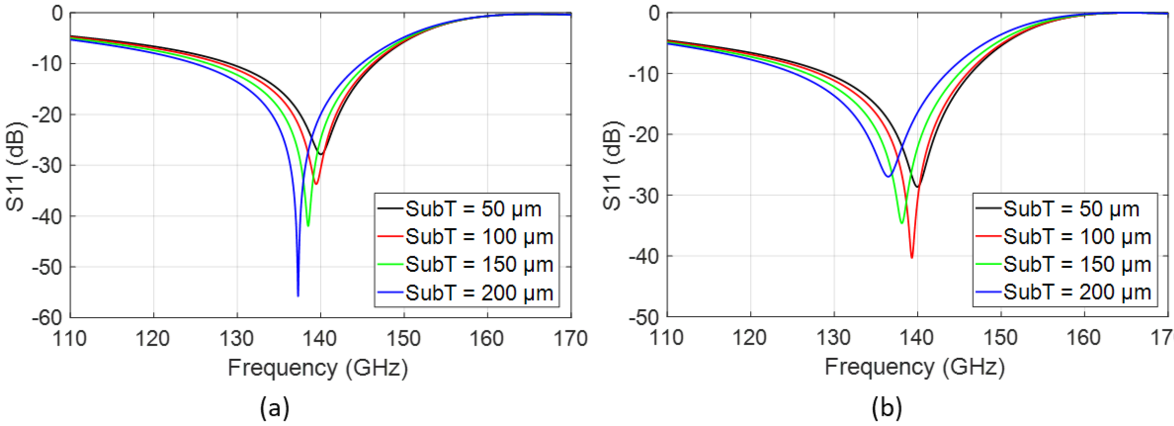

Figure 3.9 Effect of substrate thickness on (a) film facing narrow wall and (b) film facing the port.

3.4 Extracting Impedance of Thin Film

The impedance extraction is essential to establish the characteristics of the thin-film line before moving to the folded line design in Section 3.5. In Section 3.3, it is studied that the back short length is calculated if the impedance of the film is known. The impedance can be extracted from the reflection coefficient obtained from CST simulation for a thin film placed at the centre of a matched waveguide to calculate back-short length.

The thin film with a certain sheet resistance and width is placed at the centre of the waveguide, as shown in Figure 3.10. It also shows the equivalent circuit for the structures. The ports are assigned to the waveguide, where Port 1 is the input port, and Port 2 is treated as a matched load. The film is at one guided wavelength from the matched and input ports. This is because the impedance at an integer multiple of half-guided wavelength remains the same. The guided wavelength (λ_g) must be calculated and used in the simulation at the frequency for which impedance is to be extracted.

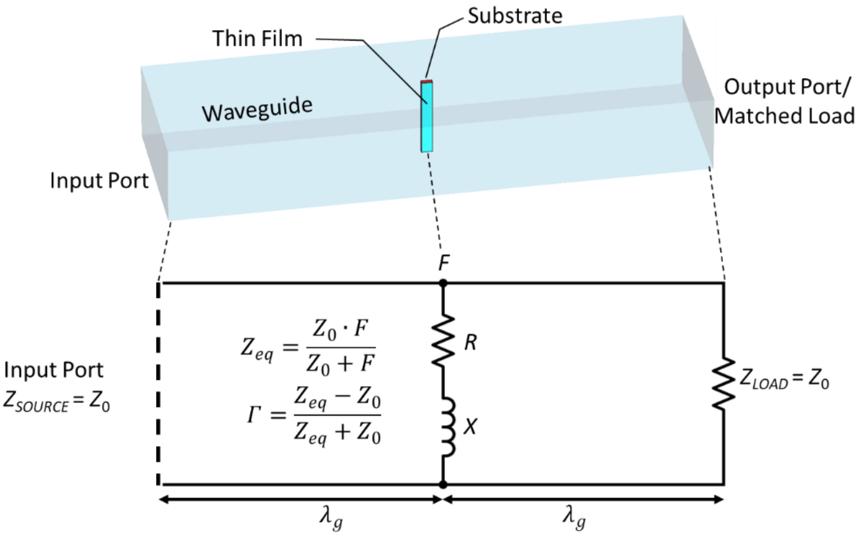

Figure 3.10 The equivalent circuit of a thin film at the centre of the matched waveguide.

The equivalent impedance is a parallel combination of load impedance ($Z_{LOAD} = Z_0$) and thin film impedance (F). The equivalent impedance at the film is,

$$Z_{eq} = \frac{Z_0 \cdot F}{Z_0 + F} \tag{3.15}$$

The waveguide having a length of an integer multiple of half wavelength gives the same impedance point on the Smith chart. Therefore, Z_{eq} is the same at Port 1 and at the film as it is separated by one guided wavelength, hence the reflection coefficient. The reflection coefficient at the film is,

$$\Gamma = \frac{Z_{eq} - Z_0}{Z_{eq} + Z_0} \tag{3.16}$$

Putting the value of Z_{eq} from Equation (3.15) into (3.16) gives,

$$F = -\frac{(1+\Gamma)}{2 \cdot \Gamma} Z_0 = R + jX \tag{3.17}$$

Equation (3.17) is used to calculate thin film impedance F if Γ is known. Here Γ is the linear reflection coefficient, and it is expressed as,

$$\Gamma = A \cdot \cos(\Phi) + j \cdot A \cdot \sin(\Phi) \tag{3.18}$$

where, A is the linear magnitude, and Φ is the phase of the reflection coefficient extracted from CST at a frequency.

3.5 Folded/Double Line Thin Film Design

The double-line design here is based on a CST simulation and optimisation and uses the knowledge gained in Sections 3.3 and 3.4. Challenges to the direct solution for double film design will be discussed later in Section 3.6.

In the design process, the two frequencies, 120 GHz and 160 GHz, are arbitrarily chosen which are at equidistance from the centre of the D-band (140 GHz). Equations (3.6), (3.12) and (3.14) are used to calculate the design parameters at 120, 140 and 160 GHz to get the initial dimensions of the thin film, as detailed in Table 3.3.

Table 3.3 Design parameters for 200 Ω resistance at three different frequencies.

Design Frequency (GHz)	120	140	160
Chosen DC Film resistance (Ω)	200	200	200
Width (μm)	64.4	112.3	156.5
Sheet Resistance (Ω/Sq)	15.6	27.2	38

The film width at the centre frequency is 112.3 μm, and the sheet resistance is 27.2 Ω/Sq. The thin film is built in the waveguide for these ($w = 112.3$ μm and $R_S = 27.2$ Ω/Sq) parameters in CST simulation to extract impedance (F), as discussed in Section 3.4. The back-short lengths (l_S) are calculated from the extracted impedance at three frequencies and detailed in Table 3.4.

Table 3.4 Extracted impedance at the three frequencies and corresponding calculated back short lengths.

	120 GHz	140 GHz	160 GHz
Reflection coefficient (Γ), Magnitude (A) and Phase (Φ)	$0.53 \angle 160.54^0$	$0.46 \angle 154^0$	$0.42 \angle 137.32^0$
Reflection Coefficient (Γ), real and imaginary	-0.5+j0.18	-0.42+j0.2	-0.31+j0.28
Film impedance (F) in Ω	225+j181.4	231+j233.42	173.65+j371.3
Back short length (l_S) in μm	1370	1059	980

The double line design is implemented in the CST using the back short lengths of 1370 µm (120 GHz) and 980 µm (160 GHz), as shown in Figure 3.11. The sheet resistance of 27.2 Ω/Sq (140 GHz) is taken from Table 3.3 for both films. The smaller widths (< 100 µm) were observed to improve return loss (S_{11}); therefore, the lowest width of 64.4 µm is selected from Table 3.3. The thickness of the substrate is 50 µm with a permittivity (ε_r) of 4.2. The connecting strip is added between the lines as the structure would carry the direct current (DC) during the power measurement application covered in Chapter 4. The size of the substrate is 50 µm × 465 µm × 825.5 µm (thickness × width × length).

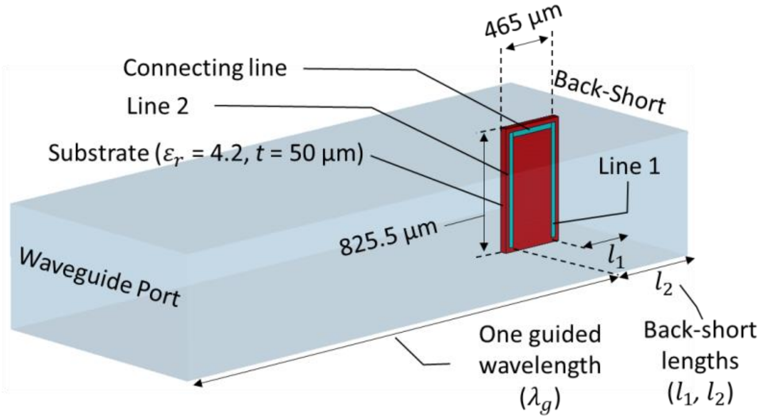

Figure 3.11 Two thin films are built in CST.

Table 3.5 shows the parameters before and after optimisation without connecting the strip. The simulated reflection coefficient (S_{11}) response of the double film structure is shown in Figure 3.12. The S_{11} in black is generated before optimisation. The S_{11} in red is the best that could be achieved after the first manual optimisation. The two main parameters of the films, the back-short length and width, are optimised to get a better S_{11} response.

Table 3.5 First manual optimisation for the double film without the connecting strip.

All in µm	Before Optimisation	First optimisation	Difference
Back-short length (l_1)	980	533	-447 (-45.6 %)
Back-short length (l_2)	1370	903	-467 (-34 %)
Film width	64.4	32	-32.4 (-50.3 %)

The parameters after the second manual optimisation with a connecting strip attached are given in Table 3.6. The width of the connecting strip is kept the same as that of both films during the simulation.

The S_{11} response obtained is shown in Figure 3.12. Then, the structure is manually optimised for the second time to get the lowest S_{11} around 140 GHz.

Table 3.6 Second optimisation for the double film with the connecting strip.

All in µm	No optimisation	Second optimisation	Difference
Back-short length (l_1)	533	403	-130 (-24.4 %)
Back-short length (l_2)	903	773	-130 (-14.4 %)
Film width	32	35	+3 (+9.4 %)

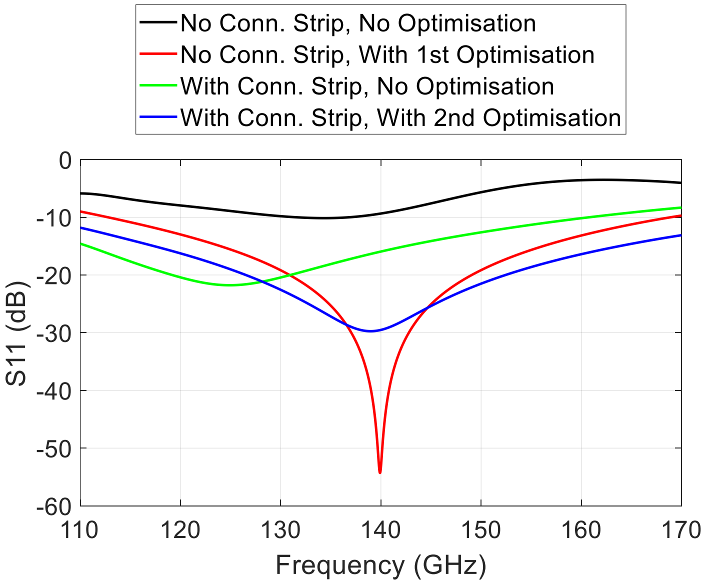

Figure 3.12 S_{11} of two film structures, $R_S = 27.2\ \Omega$/Sq.

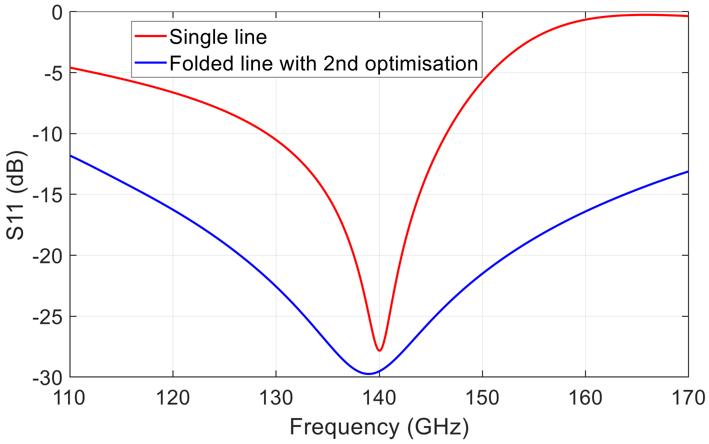

Figure 3.13 S_{11} of single and double film structures, $R_S = 27.2\ \Omega$/Sq.

The reflection coefficient (S_{11}) of the single and the double film with the connecting strip is plotted in Figure 3.13. It is observed that return loss (S_{11}) is much improved by using the double line structure. The -10 dB bandwidth of a single film structure is less than 20 GHz, but the entire band is covered with a two-film structure. The maximum return loss at 140 GHz remained around 28 dB for both structures. This is the basis design for the bolometer design in Chapter 4.

3.6 Equivalent Circuit and Equations

The equivalent circuit for a single film structure is already studied in Section 3.3 and can be extended for a double film structure to validate the latter design.

The equivalent circuit for a double-film structure with no substrate and connecting strip in between for simplicity is shown in Figure 3.14. The first thin film, with impedance F_1, is placed at a back-short distance of l_1. The thin film has resistance *R* and inductive reactance *X*. The waveguide is shorted at the end. The impedance Z_1 seen from the open end of the waveguide is a parallel combination of thin film impedance F_1 and short circuit impedance Z_{SC} at that distance (l_1). Equations for impedance Z_{SC} and Z_1 are already given in (3.8) and (3.9), respectively.

The impedance Z_1 is transferred to Z_1' at a distance l_2 from the short end. The second film of the same impedance F_2 (= F_1) is added at that location (l_2). The total impedance of the structure Z_2 is the parallel combination of the impedance of the second film F_2 and Z_1'. The impedances Z_1' and Z_2 are introduced in (3.19) and (3.20), respectively.

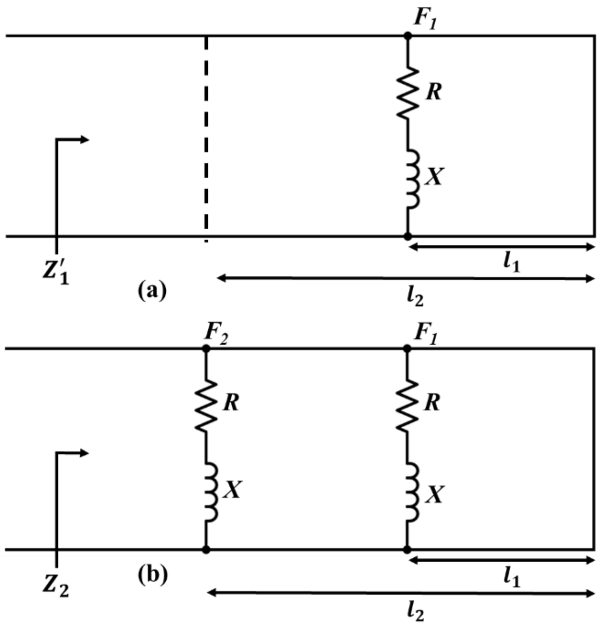

Figure 3.14 Equivalent circuit of two films (a) before adding the second film and (b) after adding the second film.

$$Z_1' = Z_0 \frac{Z_1 + jZ_0 tan\beta(l_2 - l_1)}{Z_0 + jZ_1 tan\beta(l_2 - l_1)} \tag{3.19}$$

$$Z_{eqi} = Z_2 = \frac{Z_1' \times F_2}{Z_1' + F_2} \tag{3.20}$$

Using (3.8), (3.9), (3.19), and (3.20) gives,

$$Z_{eqi} = \frac{Z_0\{jtan\beta l_0 \times F_1 - Z_0 tan\beta l_0 \times tan\beta(l_2 - l_1) + jF_1 \times tan\beta(l_2 - l_1)\} \times F_2}{Z_0\{jtan\beta l_0 \times F_1 - Z_0 tan\beta l_0 \times tan\beta(l_2 - l_1) + jF_1 \times tan\beta(l_2 - l_1)\} + F_2\{jZ_0 tan\beta l_0 + F_1 - tan\beta l_0 \times F_1 \times tan\beta(l_2 - l_1)\}} \tag{3.21}$$

Separating real and imaginary parts of (3.21) is challenging, as done in (3.10) for single-line design. Also, turning (3.21) into quadratic form is difficult as there is more than one variable, and the variable necessary in this case is the frequency '*f*', which is not explicitly available. The propagation constant can represent frequency, but it is in the angle of the tangent function. However, alternatively (3.20) can be solved for the known structure to validate the design, as discussed in the following section.

Verifying Equivalent Circuit

The double film structure can be validated using an equivalent circuit or vice versa by comparing the simulated reflection coefficient of the structure in CST to the analytically calculated in MATLAB. The double-film structure without a connecting strip is built in CST, as shown in Figure 3.15. Also, there is no substrate in the space between the films to make the structure closer to the equivalent circuit. The substrate is only present behind the films; however, this is not necessary and is believed not to affect S_{11} significantly. The design parameters are w = 40 µm, l_1 = 513 µm and l_2 = 883 µm. The design parameters are chosen to get the minimum reflection coefficient away from 140 GHz to distinguish it from the single-line design while comparing it in the same graph.

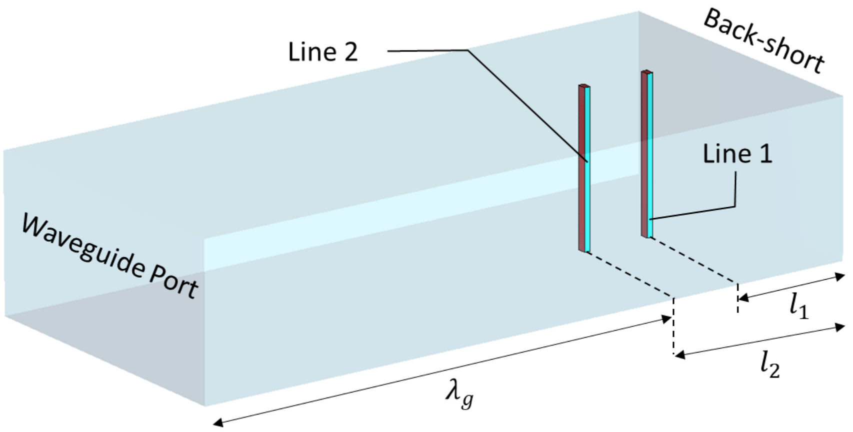

Figure 3.15 Double line structure built in CST to compare with MATLAB result.

Equation (3.21) can be solved for the design parameter of the structure in Figure 3.15. Prior to that, the impedance of thin film must be known and can be obtained in two ways: first, by calculating from (3.6) and (3.14) and second, by extracting from the simulation, as discussed in Section 3.4. The impedance for the single-line structure is also considered for comparison. The calculated and extracted impedance for thin film width of 112.3 µm and 40 µm at 140 GHz and R_S = 27.2 Ω/Sq are given in Table 3.7.

Table 3.7 Extracted Impedance and calculated impedance.

	The calculated impedance of the film (*F*) Ω	The extracted impedance of the film (*F*) Ω	Difference
Single line structure: *w* = 112.3 µm	200 + j243.11	231 + j233	31-j10.11
Double line structure: *w* = 40 µm	561.34+j398.36	592.2+j340.2	30.86-j58.16

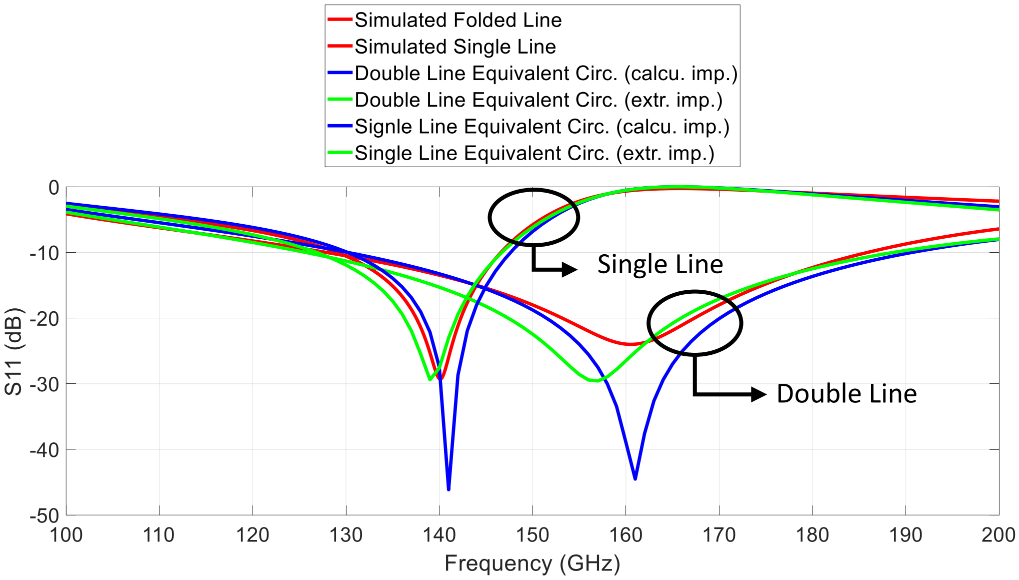

Figure 3.16 Comparison of S_{11} curves obtained from CST and MATLAB.

The impedances in Table 3.7 are used in (3.21) to find the total equivalent impedance Z_2. Equation (3.16) for reflection coefficient (Γ) can be updated for double line design as,

$$\Gamma = \frac{Z_2 - Z_0}{Z_2 + Z_0} \tag{3.22}$$

The S_{11} response from the simulation and equivalent circuit is plotted in Figure 3.16. It is seen that S_{11} of CST and MATLAB are in good agreement as the trend of the graphs is similar. This shows that the equivalent circuit can be used to describe the working of double (and more) film structures in the waveguide as a first-order approximation.

3.7 Choice of Material

The use of a particular material for the thin film becomes important as its resistivity directly affects the choice of the film thickness for a given sheet resistance. Also, the temperature coefficient of the material needs to be high enough to sense the absorbed heat. As discussed in Section 2.2, some commonly used materials for thin film are nichrome [85], [86], nickel [87], [90], and platinum [93]. The film thicknesses for the materials mentioned above calculated using (3.17) are given in Table 3.8. Not all are for temperature sensing; some are for absorbing and heating purposes only, such as nichrome [85], [86], due to low-temperature coefficient and highest resistivity. Platinum has a suitable temperature coefficient out of available materials and is used for sensing. However, the low resistivity of platinum gives lower film thickness, which might challenge the fabrication. Nickel would have an even lower thickness value.

It has been reported that titanium has been used to detect terahertz [132] and infrared [133] radiations. It has a temperature coefficient similar to platinum but has higher resistivity and gives a larger thickness than platinum and nickel. The double film structure has a sheet resistance of 27.2 Ω/Sq; the corresponding thickness for using platinum is only 4 nm, but for titanium, this is increased to 15 nm. So, titanium would be a better choice over platinum and nickel.

Table 3.8 Film thickness for different sheet resistances and materials.

Material Name	Resistivity (nΩm)	Temperature Coefficient (1/ºC)	Thickness (nm)			
			R_S=18.4 Ω/Sq	R_S=27.2 Ω/Sq	R_S=41.0 Ω/Sq	R_S=75.5 Ω/Sq
Nichrome (NiCr)	1300 [134]	0.0004 [134][135]	70.5	48	32	17
Nickel (Ni)	69.9 [135][136]	0.00641 [134]	4	2.6	2	1
Platinum (Pt)	106 [135][137]	0.003927 [134][136]	6	4	2.6	1.4
Titanium (Ti)	420 [135]	0.0035 [136]	23	15.5	10	5.6

Moreover, the metal's resistivity at a small thickness (a few nm) is higher than the bulk, according to [138]. Therefore, the thickness must be larger than the calculated to get the required sheet resistance. The resistivity arises from the electron scattering in the atoms in the lattice. The atoms in the lattice vibrate due to the thermal energy. Electron scatters from these atoms, giving rise to finite conductivity. The electron mean free path is the average distance electrons travel before scattering from the next atom or boundaries [139].

In the thin film, the low conductivity is due to small grain size, a large number of grain boundaries, and surface roughness [140]. The grain size and surface roughness depend on fabrication conditions or the process. For example, the grain size will be larger if a high temperature is used during sputtering or evaporation. Similarly, the surface roughness depends on the ion energy; if the ion energy is higher, the surface roughness will be higher [141]. When the grain size and surface roughness are comparable to the electron mean free path, electrons scatter at these boundaries and surfaces, increasing the resistivity [142].

Also, the skin depth affects the resistivity. Skin depth is the penetration of the electric field inside the metals from the surface at which the electric field's magnitude drops to 36 %. When the film thickness is comparable to the surface roughness, the distance electrons travel becomes larger, increasing the resistivity [143]. It is always preferred to have film thickness at least five times the skin depth at working frequency [144].

Therefore, the thickness must be larger than the calculated to get the required sheet resistance. Trials of depositing metal thin film and measuring its sheet resistance have been shown to be essential to achieve the targeted sheet resistance and, ultimately, the expected reflection coefficient (Γ or S11) or the impedance match.

3.8 Summary

The placement of a thin film in a waveguide is a resonance type matching problem. The direct solution is available for single-line design to find the dimension of the line and the distance from the waveguide back-short. The same solution can be used for both types: film facing waveguide input port and facing the narrow wall. The latter is convenient for adding more films in the E-plane of the waveguide to improve bandwidth and is used in this thesis. The solution for the double line design is challenging as the equivalent circuit equation becomes complex to obtain matching conditions. The double line design is a simulation-based intuitive method for broader bandwidth. However, the structure has been validated by using the design parameter in the equivalent circuit equation. The equivalent circuit for the double line structure agrees with the simulation results. The material choice is discussed where the material with both high-temperature coefficient and resistivity, such as titanium, is chosen as the sensing material from a fabrication point of view. The double line structure will be used in Chapter 4 to realise the bolometric power detector.

CHAPTER 4

THIN FILM BOLOMETRIC POWER DETECTOR

This chapter discusses utilising the double-line design from Chapter 3 and developing the complete bolometric power detector as a portable power transfer standard. The chapter starts with a discussion about the necessity of fine-tuning the structure of the design with practical consideration and analyses the effect of such changes on the reflection coefficient. Then, the dual sensor design with double-layer thermal shielding is presented for ambient temperature compensation. In the end, the fabrication and characterisation of the power detector are presented and compared with the commercial power sensor.

4.1 Concept Design of the Thin Film Bolometer

The double-line design can be transformed into a bolometer. The two essential considerations are the DC readout arrangement and thermal isolation. The first contributes to defining the substrate dimension, whereas the latter contributes to determining the channel/recess dimension that opens into the waveguide. Such structural changes affect the reflection coefficient.

4.1.1 Substrate shape for DC readout consideration

The basic double film structure discussed in Chapter 3 has substrate dimensions of 825.5 µm ×465 µm ×50 µm (length × width × thickness) without DC biasing pads. The pads must be added to the sensor chip for DC readout arrangement. Two approaches can be anticipated: the first would form the substrate in a T-shape, and the second would be rectangular, as shown in Figure 4.1 (a) and (b). The T-shape substrate has two pads on either side (horizontally aligned), and the central section will go into the waveguide. Whereas for the rectangular substrate, the pads are one on top of the other (vertically aligned), and the sensing element is at the bottom. The width of the substrate going into the waveguide is less for a T-shape substrate than for a rectangular one. Therefore, the first approach will have less effect on the reflection coefficient (Γ or S_{11}). However, it must be noted that the T-shape substrate is difficult to cut and handle. Thus, the rectangular shape is selected to proceed with the design. Also, the substrate thickness is increased to 100 µm for ease of fabrication and handling.

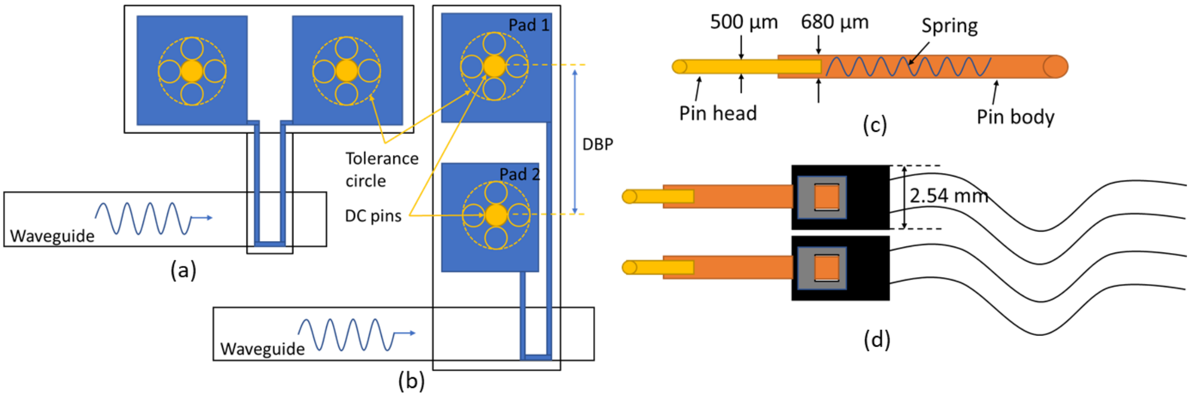

Figure 4.1 Sketch of (a) T-shape substrate, (b) rectangular shape substrate, (c) spring-loaded pin for DC connection, (b) spring-loaded pins in the Dupont wires.

The pad size, hence, the substrate width, primarily depends on the dimension of the spring-loaded pins used to make the connection to the readout device. The sketch of the spring-loaded pin is shown in Figure 4.1 (c). The pin head can move in and out of the body with the help of an internal spring. This mechanism protects the surface against which the pin is pressed and makes contact safe and secure. The diameter of the pin head is 500 µm, and that of the body is 680 µm. It must be noted that when the pin touches the pad surface, it might have offsets from the original/expected position. Therefore, the pad size should be larger than the pin head diameter. A tolerance circle of diameter two times the pin head diameter (2 × (0.5 mm) = 1 mm) can be drawn to get a rough estimation of the pad dimension; the pad should be at least 1 mm × 1 mm in size or more if possible. Therefore, a substrate width of 2 mm is preferred to accommodate larger pads and thin-film elements.

The substrate height and the distance between the DC pins (DBP) or the centre of the pads primarily rely on the dimension of the Dupont jumper wire head, as shown in Figure 4.1 (d). The width of the Dupont wire head is 2.54 mm, and when the two wires are placed closely, the DBP will be 2.54 mm (~ 3 mm). Therefore, the pads are set at a 3 mm distance apart from their centre. The spring-loaded pin should fit in the Dupont wires. The design progressed through the following stages to realise this concept.

Stage 1: Increasing substrate width

The folded-line structure is built in the waveguide with increased substrate dimension, a width of 2 mm and a thickness of 100 µm, as shown in Figure 4.2 (a). The substrate protruded from the top broad wall of the waveguide. The pads are not added in this early-stage design. The clearance gap between the substrate edge and the top waveguide slot is initially chosen as 20 µm. Table 4.1 lists updated parameters compared to the previous design in Chapter 3. The sheet resistance of 27.2 Ω/Sq is used for the thin film during simulation.

Table 4.1 Updated parameters for Stage 1.

All in µm	Earlier Design Ch 3	Stage 1	Difference
Substrate width	605	2000	1395 (230 %)
Film width	35	40	5 (14.3 %)
Back-short length (l_1)	773	773	0
Back-short length (l_2)	403	403	0
The gap at the left, right, front and bottom	-	20	-

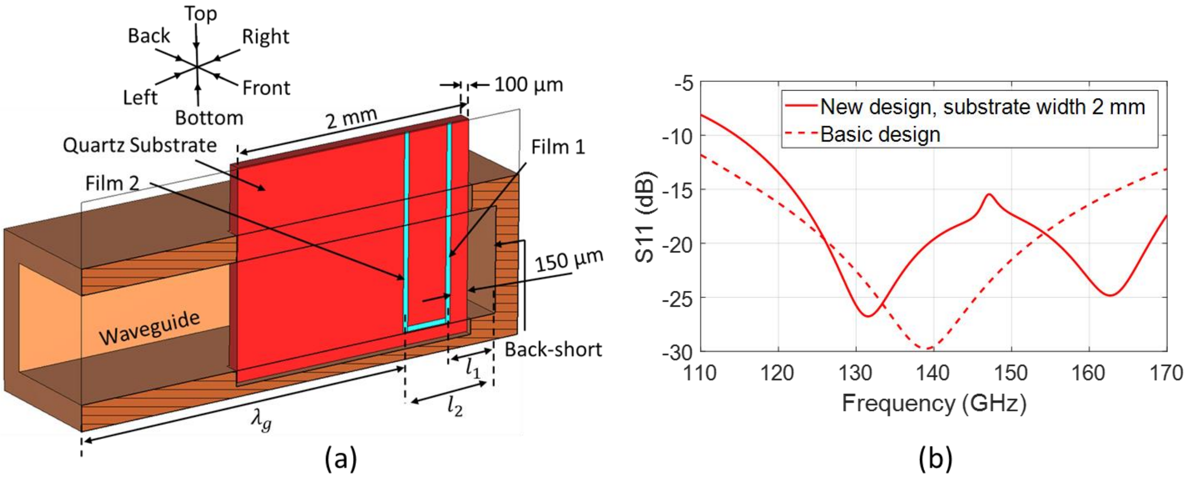

Figure 4.2 Design stage 1 (a) Double film structure with increased substrate width, (b) S_{11} for the design stage 1 and the basic design from Chapter 3.

The effect of increased substrate dimension is shown in Figure 4.2 (b). The reflection coefficient (S_{11}) of the new design is compared to the basic folded-line design from Chapter 3. It shows that the modified structures have introduced another minima (matching point in the band) in the S_{11} at 162.5 GHz; the first is at 131.5 GHz. The new design has a - 15 dB bandwidth of nearly 50 GHz (170-120

GHz), which is 83.3 % (50 GHz/60 GHz ×100). Henceforth, each stage's solid red-coloured S_{11} graphs are followed in the next consecutive stages and are shown in dashed lines for comparison.

Stage 2: Adding pads for DC connection

The structure is further modified by adding two pads above the sensor element, and it is placed in the metallic body, as shown in Figure 4.3. The size of Pad 1 and Pad 2 is 2 × 1.7 mm and 2 × 1.51 mm, respectively. The DC pins are also modelled in the design with a distance between their centre of 3 mm. Hereafter, the substrate with two pads and a sensor element (folded-line) can be called a sensor chip. A metal body surrounds the sensor chip from all sides (left, right, top, bottom, front and back) with a clearance gap of 20 µm chosen initially. The gap at the front is required to avoid a short circuit of metallic thin-film features on the chip to the housing. In the current design, the front gap is maintained at 20 µm. The sheet resistance used for the gold pad during the simulation is 0.244 Ω/Sq, which corresponds to a thickness of 100 nm.

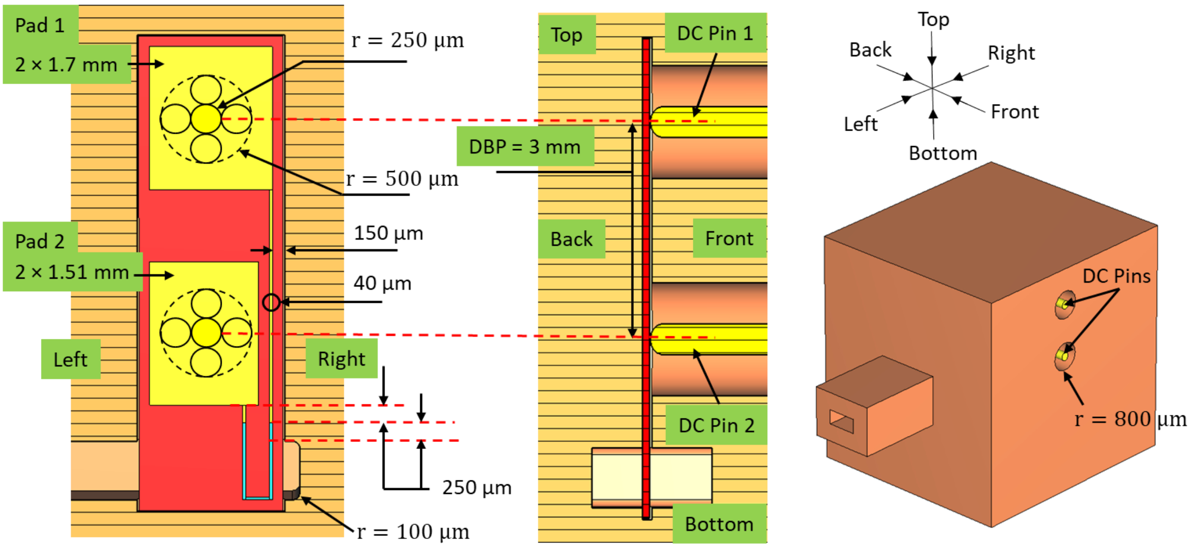

(a) (b) (c)

Figure 4.3 Design stage 2 (a) front view shows two pads, (b) left view shows DC pins, (c) metal housing for simulation.

The stage 2 structure is simulated with and without DC pins. The simulation in Figure 4.4 shows that, in both cases, the results are identical, which indicates minimum leakage. The results are also compared with the stage 1 design; the S_{11} of the stage 2 design has weak resonances and can be attributed to the recess/slot in the waveguide.

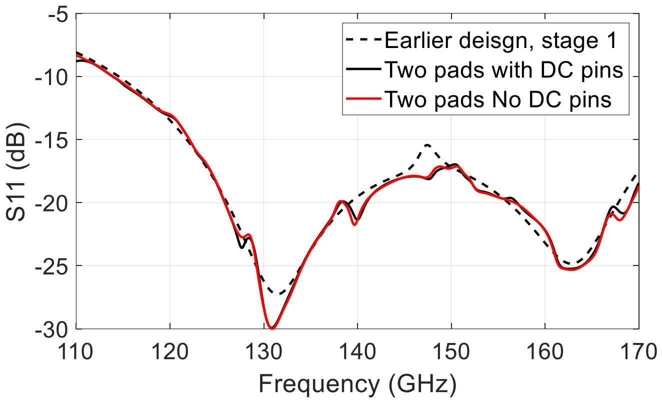

Figure 4.4 S_{11} for the design stage 2.

Stage 3: Adding a cavity above the pads and a reflecting strip on the chip

The design is further modified by adding the empty cavity in the metal body above the pads and the reflecting strip on the sensor chip, as shown in Figure 4.5 (a), (b) and (c). The width of the thin film (FW) is increased to 45 µm. The empty cavity is produced above the pads to avoid the closeness of metal and pad surfaces. The reflecting strip is primarily introduced to block RF leakage to the region of the extended substrate with the pads; it would also help align polyimide tape after fabrication (Section 4.3). The clearance gaps are maintained at 20 µm on all sides. The DC pins are removed, and a relatively small metallic body around the sensor chip is designed to reduce the simulation time.

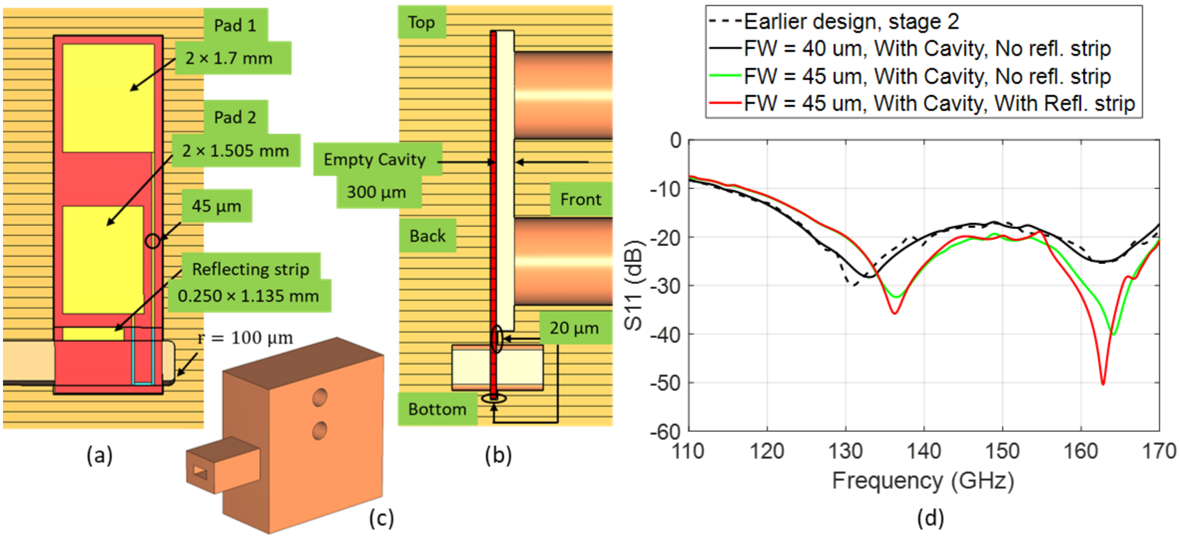

Figure 4.5 Design stage 3 (a) front view shows reflecting strip, (b) left view shows empty cavity, (c) metal housing, (d) S_{11} for the design stage 3.

The simulated results in Figure 4.5 (d) show that the position of S_{11} minima remains the same and has no significant impact after adding the empty cavity above the pads. Increased film width (FW) has slightly shifted the curve to a higher frequency and improved return loss. This is essential for compensation, as a large clearance gap to be added in Stage 4 would do the opposite. It is observed that the reflecting strip has no significant impact on the S_{11}.

4.1.2 Polyimide tape for thermal insulation considerations

Thermal insulation of the chip is essential to reduce the heat leak into the metal body. The heat can also flow from the metal body to the sensor chip due to environmental or ambient temperature variation. The heat leakage introduces additional settling time in the sensor, which is the time required for the sensors' response to reach the thermal equilibrium. Therefore, insulating the sensor chip from the surroundings is vital to improve response time and reduce temperature drift. Polyimide (Kapton) is an excellent thermal insulator and has been modelled in the design to analyse its effect on the reflection coefficient (S_{11}). The polyimide has a dielectric constant of 3.5, a dissipation factor of 0.0026 and an electrical resistivity of 1.5×10^{17} Ωm [145]. The structural modification continues in stages, with the numbering followed from earlier stages.

Stage 4: Adding polyimide tape under the pads

The empty cavity is built under the pads so the substrate can be designed in that space, as shown in Figure 4.6 (a). The depth of the cavity is chosen as 300 µm initially to see the effect on the reflection coefficient. A wall of 250 µm is maintained between the cavity and waveguide to avoid a large opening into the waveguide. As shown in Figures 4.6 (b) and (c), polyimide is added under the pad. The thickness of polyimide tape could be 50 µm or 100 µm in practice. However, a thickness of 110 µm (an additional 10 µm assuming tolerance) is used for simulation. More space is added around the chip by increasing the clearance gaps from 20 µm to 100 µm on the left, right, and front sides and 50 µm on top and bottom, as detailed in Table 4.2.

Table 4.2 Updated parameters for design stage 4.

All in µm	Stage 3	Updated Design Stage 4	Difference
Film width	45	45	0
Back-short length (l_1)	773	803	30 (4 %)
Back-short length (l_2)	403	433	30 (7.44 %)
The gap at the left, right and front	20	100	80 (400 %)
The gap at the top and bottom	20	50	30 (150 %)

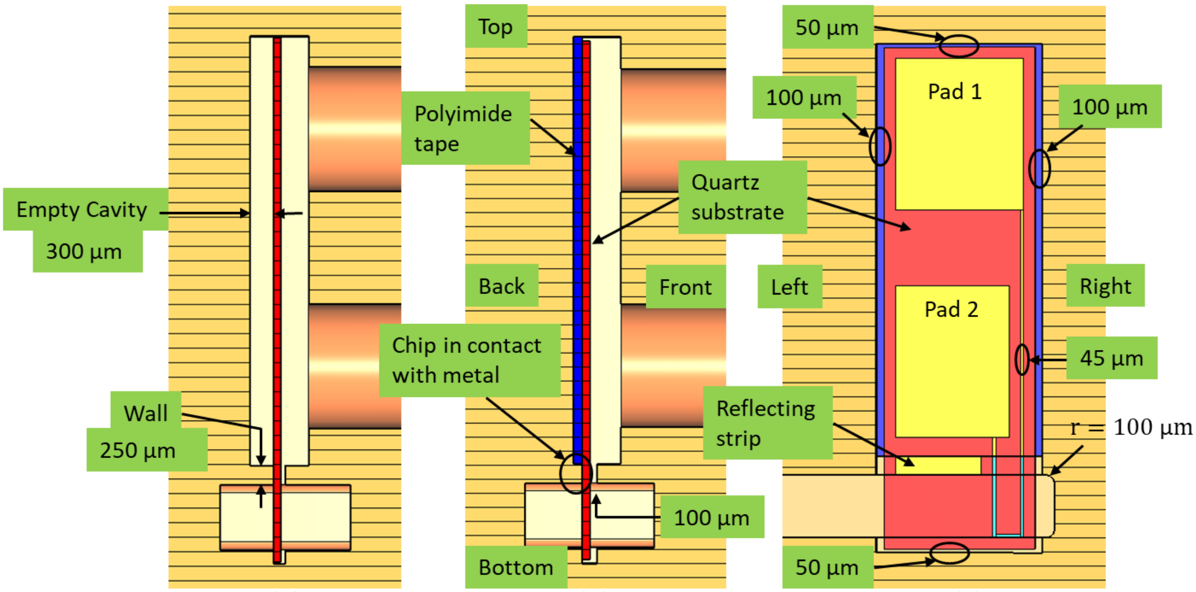

(a) (b) (c)

Figure 4.6 Design stage 4 (a) empty cavity under pads, (b) left view showing polyimide under pads, (c) front view showing gap around the chip.

The empty cavity has affected the second minimum in S_{11} (black), around 162 GHz; that is, return loss is reduced approximately to 20 dB from 40 dB, shown in Figure 4.7. The large opening in the waveguide due to increased clearance gaps has added spurious resonances, as seen in green and red. The large opening in the waveguide due to the clearance gaps has also shifted the green and red graphs towards the lower frequencies, compensated for the shift due to increased film width in Stage 3. It is observed that the sensor chip with a reflecting strip slightly improved the return loss at higher frequencies and did not have significant effects on overall S_{11}. This structure could obtain a 15 dB return loss between 120 GHz – 170 GHz.

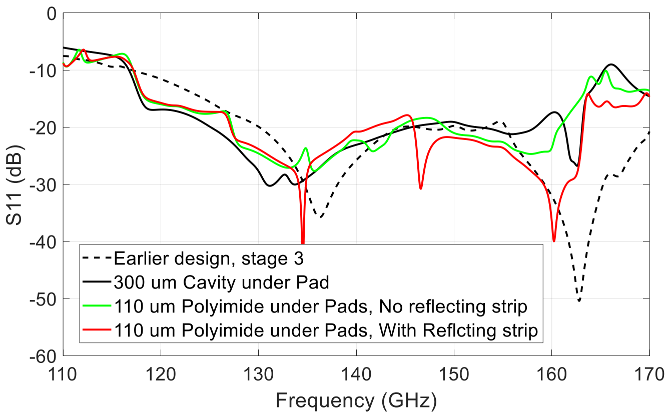

Figure 4.7 S_{11} for the design stage 4.

Stage 5: Wrapping chip with polyimide tape

In this stage, the chip was further isolated from the surroundings by keeping none of its areas in contact with the body. The slot for the polyimide is opened into the waveguide under the chip, as shown in Figure 4.8 (a). The polyimide tape comes up from the sides (left, right and top) and wraps over the chip, as shown in Figure 4.8 (b) and (c). All the gaps at the chip's left, right, front, top and bottom are increased to 110 µm, the same as the polyimide thickness. Another essential modification is based on the dimension of the drilling bit for machining. The smaller the drill bit's diameter, the shorter its length is, limiting the depth it can reach. The detector body would be designed in an E-plane split block, and the drill bit, which can reach the half waveguide width (b/2), has a diameter of 300 µm. Therefore, all the corners/edges parallel to the drill bit must be rounded or be in a Micky-mouse ear shape with a radius of 150 µm. The Micky-mouse ears are designed at all four corners of the sensor chip, and the radius of the rounded edges of the waveguide is increased to 150 µm.

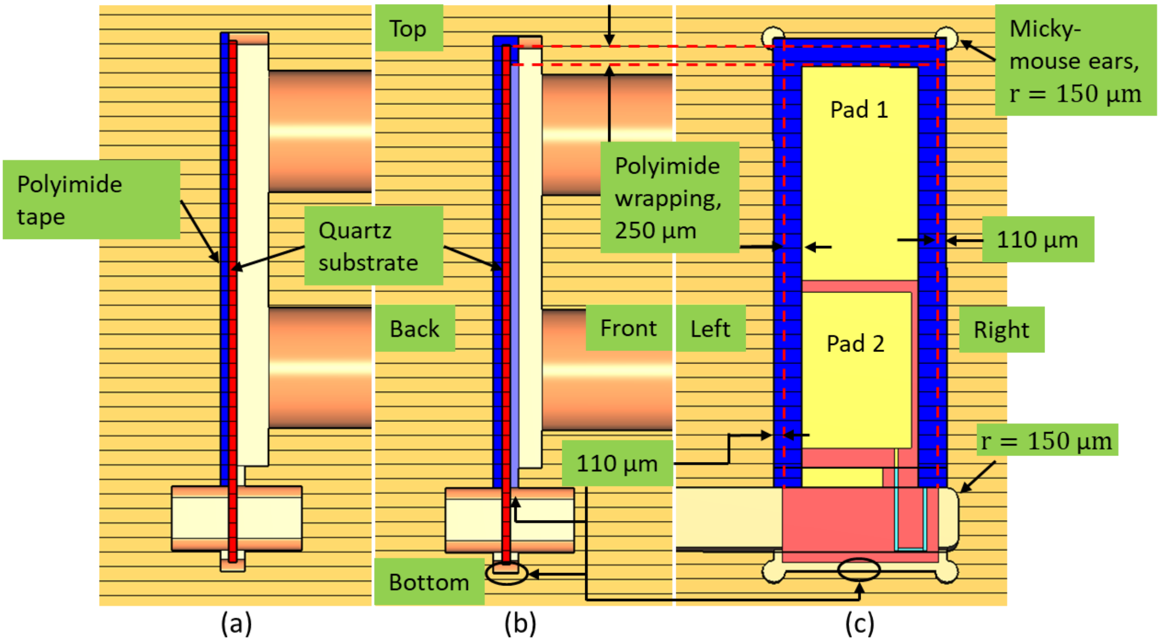

Figure 4.8 Design stage 5 (a) polyimide tape is open in the waveguide, (b) left view shows polyimide coming up from sides, (c) front view shows Micky-mouse ears and other cavities.

In Figure 4.9, the second minima in S_{11}, around 160 GHz, disappears after increasing gaps on the top and bottom of the chip, the newly added Micky-mouse ears, and round edges. The S_{11} for polyimide wrapping widths of 0, 250 and 500 µm over the sensor chip are plotted in Figure 4.9, which are the final results for the detector. Specifically, the S_{11} for polyimide width 250 µm is regarded as the final as it is the average width. In practice, the sensor chip can not be wrapped entirely, as the electrical contacts have to be maintained.

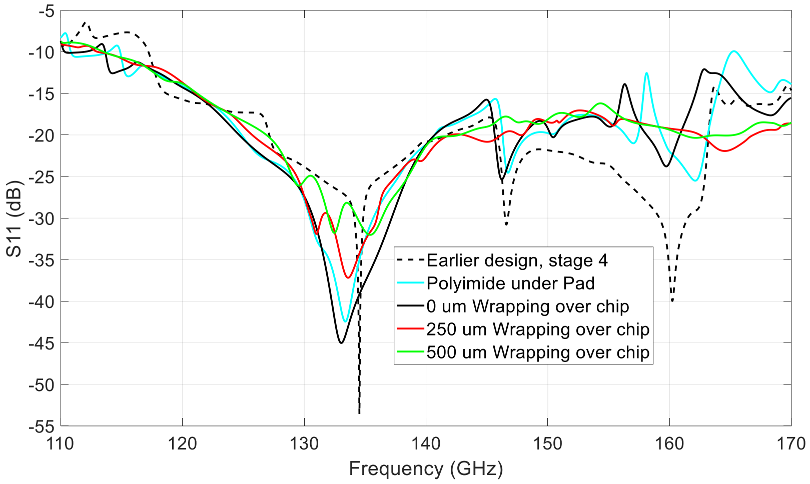

Figure 4.9 S_{11} for the design stage 5.

The plot for the starting design and all modification stages are plotted in Figure 4.10 using dashed lines except for the latest stage 5, indicated with a solid line. These dashed lines are the final selected S_{11} (red-coloured) from the respective stage for comparison. This shows that the reflection coefficient has remained below -15 dB from 125 GHz to 170 GHz for all five design stages. It can also show that although the plots vary at various stages, they remain close to the first stage, where the substrate width is selected to be 2 mm. This reveals that the substrate width inside the waveguide defines the S_{11} of the final design. The other structures in the design, such as open cavities in the waveguide, do not significantly affect the S_{11} trend; however, they only introduce weak resonances.

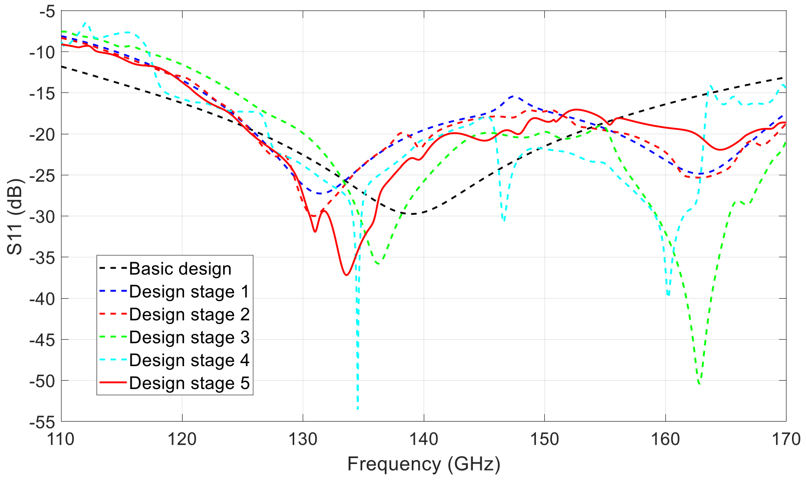

Figure 4.10 The S_{11} comparison of all design stages.

4.2 Detector Packaging

The detector packaging is the housing around the sensor chip for electrical connection and protection from the surrounding environment; the latter means ease of handling and thermal insulation. It gives the detector the dimensions to be used in desired metrology applications.

4.2.1 Sensor chip and mask details

The layout of the sensor chip and the polyimide around it is shown in Figure 4.11. The dimension of the chip is 6.6255 mm × 2 mm × 100 µm (length × width × thickness). As discussed in Section 3.7, the suitable material for the thin film to get the required sheet resistance of 27.2 Ω/Sq is titanium of 15.5 nm due to ease of fabrication. The material for the pad is gold, with a thickness of 100 nm. The polyimide tape wraps the chip from all sides except at the front for the DC connection. The thickness of polyimide is 110 µm. The bottom edge of the reflecting strip aligns with the polyimide.

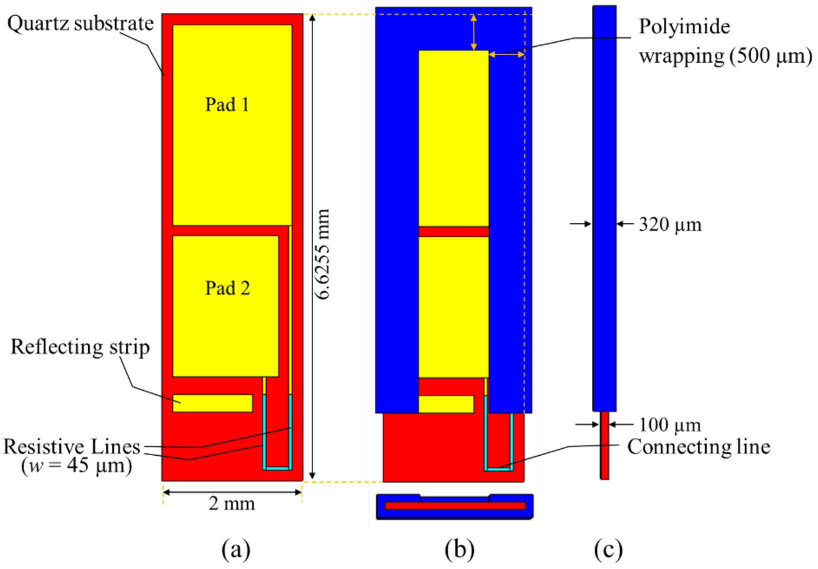

Figure 4.11 (a) sensor chip, (b) front view and bottom view, (c) side view of chip wrapped in polyimide.

The 20 mm × 20 mm masks are designed for the titanium layer and gold layer deposition on the quartz wafer, as shown in Figure 4.12 (a) and (b), respectively. It contains four sensor chips and markers to align the mask. The 50 µm thick frame at four corners is for cutting the sensor chip after fabrication; the dashed orange line indicates the cutting plane, as shown in Figure 4.12 (c). The total length of the resistive titanium line can be calculated from the dimensions shown in Fig 4.12 (c). The length of one of the vertical resistive lines is 1.0755 mm, and the length of the horizontal resistive line (connecting strip) is 0.325 mm. The thin film has a width of 45 µm. The total length of the resistive line, calculated along the centre of the line, is 2.476 mm (2 × (1.0755 + 0.045/2) mm + (0.325 + 2×0.045) mm). Therefore, the total resistance of the resistive line can be calculated as 1.5 kΩ using (3.6). After the deposition of titanium and then gold, a single structure will be seen, as in Figure 4.12 (c).

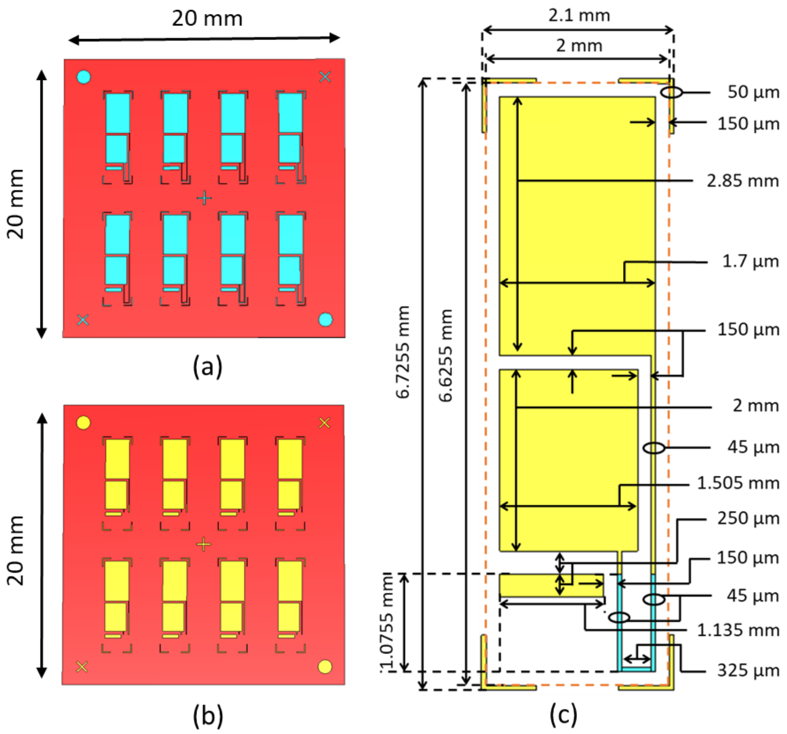

Figure 4.12 (a) Masks for 15.5 nm titanium (Ti) layer deposition, (b) mask for 100 nm thick gold (Au) layer deposition, (c) a unit structure.

4.2.2 Single-sensor housing

The detector body with the UG-387 flange is developed in two blocks, split in the E-plane of the waveguide, as shown in Figure 4.13. The split is at an offset of 0.11 mm from the centre, which aligns the folded polyimide tape over the sensor chip, maintaining the chip at the centre of the waveguide in the E-plane. The total width of the square block at the back of the flange is 12 mm (6.11 mm + 5.89 mm). The sensor chip is in the left block, and the spring-loaded DC pins with PCB (printed circuit board) are on the right. The detector body behind the flange has two holes for alignment pins, three for the screws on the body and two for the PCB. The PCB has a thickness of 1.6 mm, and the two square copper patches are designed on the PCB around the DC pins as a base for soldering.

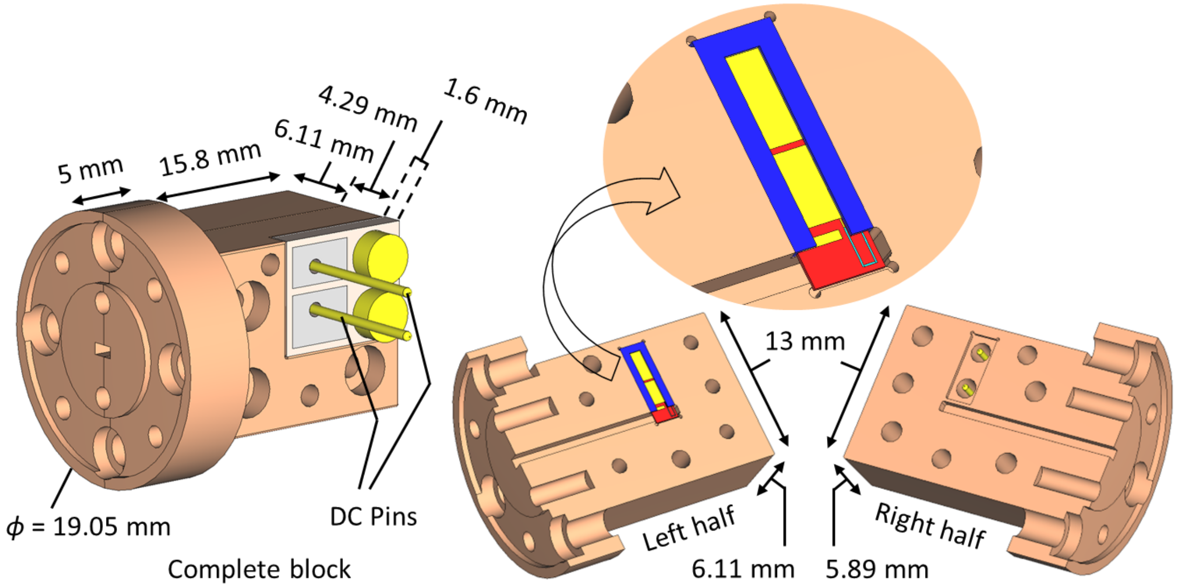

Figure 4.13 Detector housing with chip and DC connection.

The detailed dimension of recesses or cavities in the detector body is given in Figure 4.14. The CNC (computer numerical control) machines utilise drill bits with a certain radius that will make the corners curved. The corners of the recess where the sensor chip would be placed are modified with Micky-mouse ears having a radius of 150 µm. The corners of the waveguide are rounded with the same radius. The radius of the spring-loaded pin is 240 µm, and that of the hole it is coming out from is 800 µm.

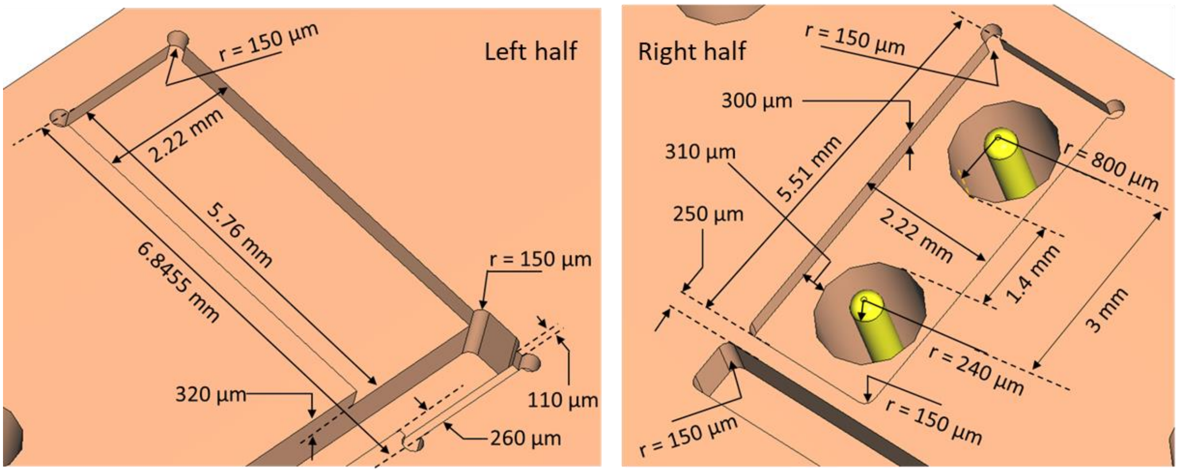

(a) (b)

Figure 4.14 Cavities in (a) left half, (b) right half of the detector body and their dimensions.

4.2.3 Dual-sensor housing

The sensor will be used in an ambient temperature environment, so removing the effect of temperature drift on the power measurement is essential. Therefore, a dual sensor configuration is adopted to compensate for the ambient temperature variation. It consists of the main/active sensor (sensor A) for detecting incident microwave power and the dummy sensor without a flange (sensor B) for detecting ambient temperature variation, as shown in Figure 4.15 (a). Four spring-loaded DC pins touchdown on the pads can be seen in Figure 4.15 (b).

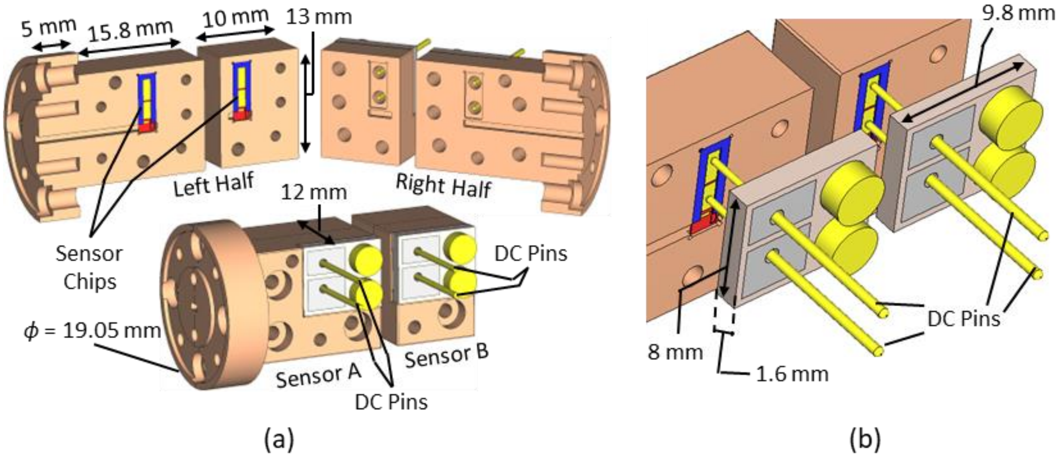

Figure 4.15 Design of (a) dual sensor configuration, (b) spring-loaded DC pins and PCBs contacting pads on the sensor chips.

Shielding

The sensors are also found to be very sensitive to handling and airflow, so they are shielded, as shown in Figure 4.16. The inner shielding is made of low thermal conductivity PEEK (polyether ether ketone), a plastic material, and the outer one is made of aluminium. The two sensors (A and B) are placed together to ensure the sensing of the same ambient temperature and simultaneously be thermally isolated.

The sensor bodies (sensor A and sensor B) have an air gap of 2 mm between them. The sensor bodies and the PEEK shielding have a 1 mm air gap at the central region. The shielding is designed to hold the sensor bodies at the corners and eight headless M2 screw holes (for four sides of each sensor body) for support in the central region. There are seven headless M2 screw holes for tightening where the sensor body and shielding are in contact, two in the flange, three in the front (for sensor A) and two in the back (for sensor B). All this ensures the sensor bodies are firmly fixed in the inner PEEK shielding. The shielding has four through holes for M1.6 screws to hold itself together.

The outer aluminium shielding surrounds the PEEK shielding. This gives the final dimension to the power detector. It has ten M2 screws, six for holding itself and four for tightening the inner PEEK shielding. This ensures the inner shielding consisting of sensor bodies remains fixed in the outer shielding and is easy to handle.

The window is designed to access the four spring-loaded DC pins. It has two rectangular sub-windows; the first one is for sensor A and the second for sensor B. The second sub-window is kept larger as sensor B can be moved/placed closer to sensor A; hence, the DC pins need more space. However, sensor B would be placed at a fixed distance of 2 mm during measurement.

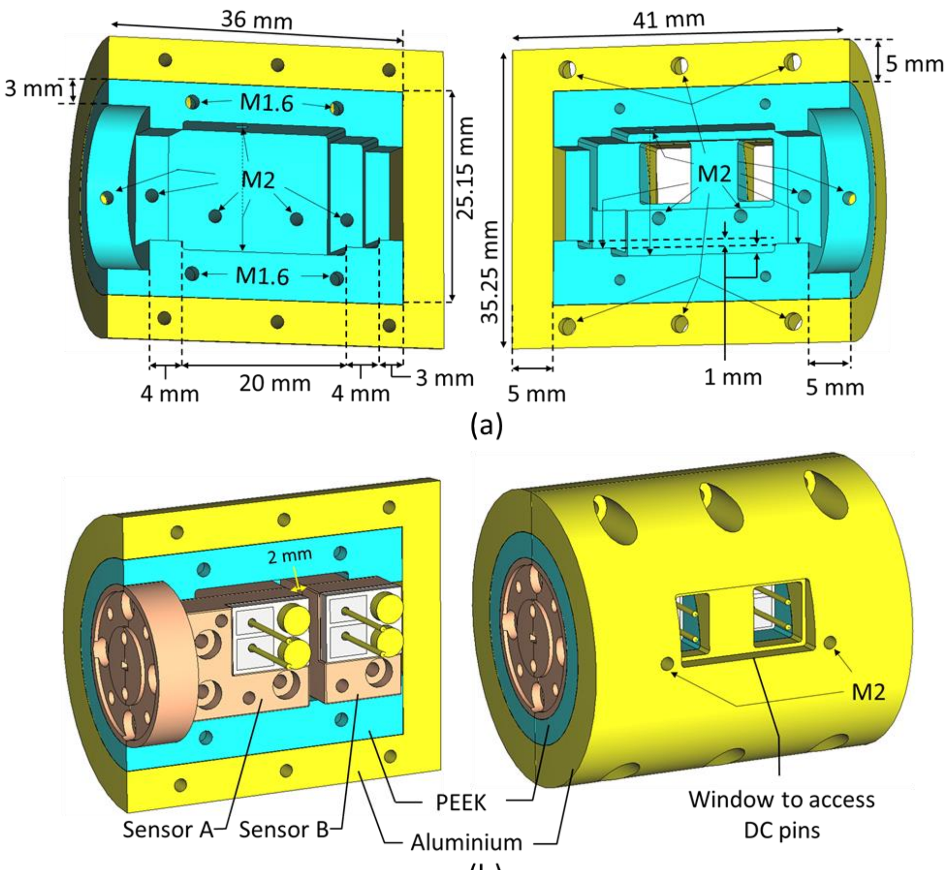

Figure 4.16 Design of (a) inner and outer shielding, (b) Sensor A and Sensor B assembled in shielding.

4.3 Fabrication and Assembly

The fabricated sensor chips are shown in Figure 4.17 (a). The titanium thin film was evaporated on the quartz substrate. At the nominal thickness of 15.5 nm, the measured sheet resistance is 79.3 Ω/sq, about three times higher than the design requirement. The film thickness is therefore increased to reach 27 Ω/sq. The DC pads were coated with gold of 100 nm. The sensor chips were diced using a dicing saw. The measured resistance of the folded line is ∼1.6 kΩ, which is consistent with the design.

50-μm-thick polyimide tape was used to wrap and fit the chip into the housing. The polyimide does not significantly affect the sensor response as it is not into the waveguide; hence, the available 50 μm thick polyimide tape is used while assembling instead of the 110 μm thick used in the simulation. Also, it is convenient to use 50 μm thick polyimide with a sensor chip that can easily fit in the 110 μm space. The polyimide tape was applied to the sensor chip at the back by holding the long tape horizontally 90^0 to the chip at a distance, then precisely landing on the chip while aligning to the edge of the reflecting strip. The extra tape around the chip is then cut using an angled cutter tool (curved scalpel blade) without damaging the thin chip. As the polyimide tape is manually handled, the wrapping width over the chip cannot be controlled/cut precisely; instead, the tape is cut closer to the chip edge.

As shown in Figure 4.17 (b)–(d), the sensor bodies are made out of the thermoplastic polymer PEEK, which has a low thermal conductivity of 0.25 W/m·K, to reduce the effect of surrounding temperature drift. The body of sensor A is initially coated with 4 μm of copper as a base layer, also called ‘copper flash’, then goldplated with 0.1 μm thickness. In contrast, sensor B is not plated and does not carry any microwave signal. The absence of the gold coating also helps with thermal isolation.

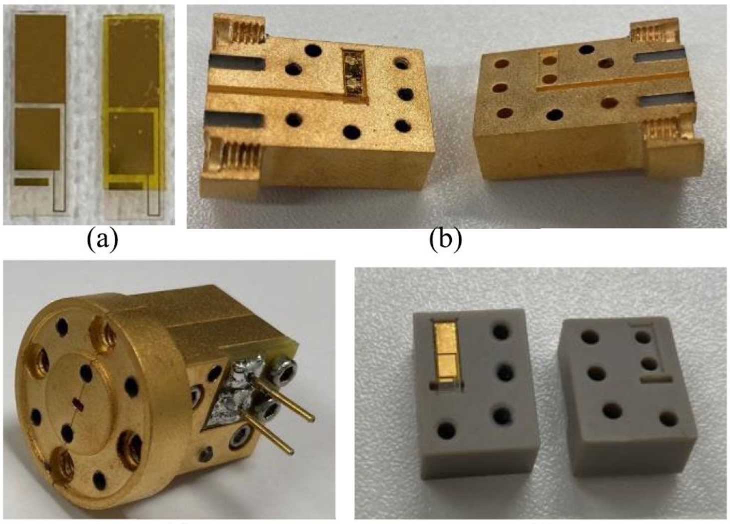

(a) (b)

(c) (d)

Figure 4.17 Fabricated (a) the first sensor chips before and the second after wrapping with polyimide, (b) Sensor A in split blocks, (c) assembled Sensor A, (d) Sensor B in split blocks with the chip installed.

The insides of the fabricated shieldings are shown in Figure 4.18 (a). Sensors A and B are placed inside the shielding, as shown in Figure 4.18 (b), which helps with the handling and reduces the effect of ambient temperature fluctuation. The shielding also ensures a similar ambient environment for both sensors. The sensor bodies are held inside the PEEK shielding only at the corners. There is an air gap of 1 mm surrounding it for thermal isolation. The air gap between the sensors is kept at 2 mm. This will minimise the amount of heat exchange between sensors A and B. All these measures aim to reduce the correlation between the two sensors so that sensor B can only trace the ambient temperature. The size of the cylindrical aluminium shielding is 35 × 41 mm (outer diameter × length), which is comparable to that of the commercially available PM5 (51 × 48 × 76 mm) [102].

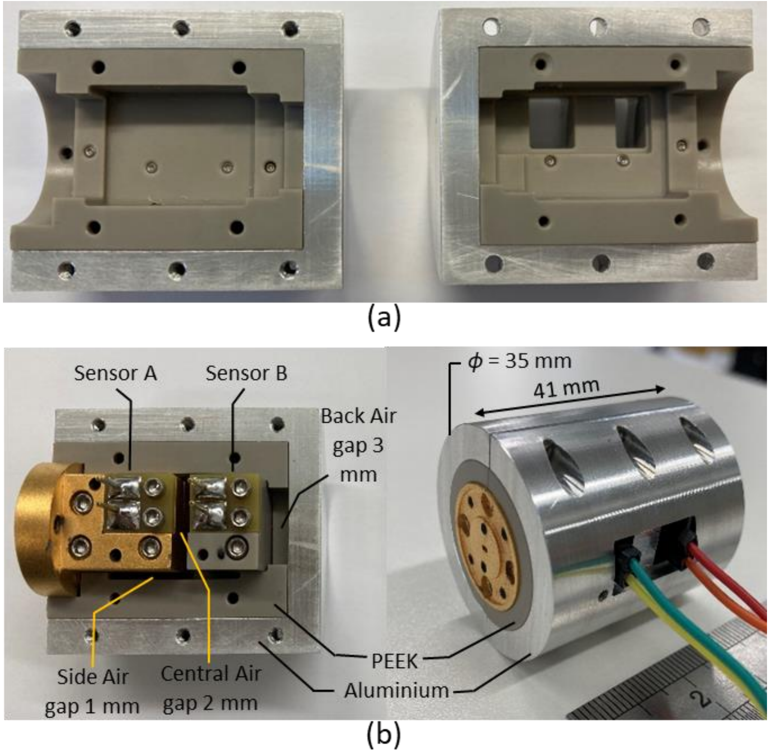

Figure 4.18 Fabricated (a) inner and outer shielding, (b) Sensors A and Sensor B assembled in shielding.

Fabrication challenges

The fabricated sensor mask and the sensor A body before gold plating are shown in Figure 4.19. It is observed that some of the sensor chips are broken into two halves, some have debris stuck, and most of them have sharp quartz at the edges. The debris sticking on some sensor chips could not be cleaned, so they are not used as this may not have good electrical contact. Sharp quartz at the edges is cut manually using a curved scalpel blade. It is observed that the sensor A body has residue plastic threads at the edges and corners, which are cleared before gold plating. The fabrication of sensor B and both shieldings have not shown such threads.

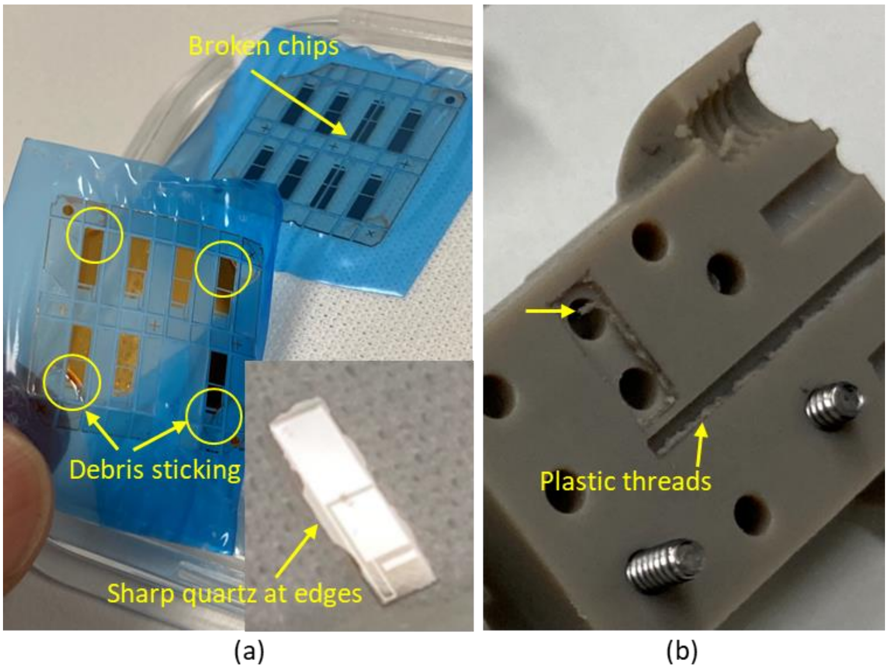

Figure 4.19 Fabricated (a) sensor chips, (b) sensor A body before plating.

4.4 Measurements and Discussion

The detector/sensor characterisation is thoroughly performed at NPL, London. This includes the measurements of reflection coefficient, short-time response, long-time response, frequency response and linearity as described in [24].

4.4.1 Reflection coefficient measurements

The Vector Network Analyser (VNA) with a D-band extender module is used for the measurement of the reflection coefficient (Γ or S_{11}). The VNA-extender combination was first calibrated using a D-band calibration kit using through-reflect-line standards. The detector is connected to the extender waveguide port. The reflection coefficient measurement is performed over the full D-band frequency range. The detector DC outputs were not connected to any instrument during measurement. The measured S_{11} is plotted in Figure 4.20. The reflection coefficient is - 4.2 dB at 110 GHz and remains below - 15 dB for frequencies above 120 GHz. The simulated S_{11} is also plotted for comparison and shows good agreement. The ripples in the reflection coefficient are seen due to standing waves formed in the waveguide due to imperfection in the connection (boundary or discontinuity), causing interference between reflected and transmitted waves. The interference is frequency dependent, and so is the reflection coefficient, causing periodic patterns or ripples.

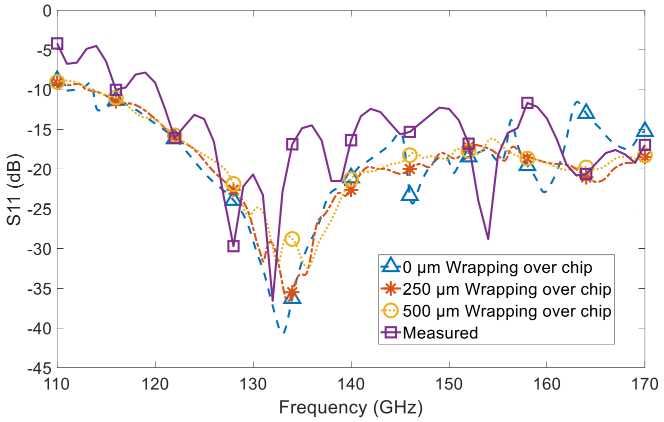

Figure 4.20 Measured reflection coefficient (S_{11}).

4.4.2 Short-term time measurement

The short-term time measurement is performed to analyse how the designed sensor responds soon after the power is applied. The response of the reference/commercial PM5 sensor is also analysed simultaneously. A comparison is drawn between the two to validate the working of the designed sensor.

The measurement setup is shown in Figure 4.21. The signal generator and frequency multiplier module produce the required microwave power controlled through an attenuator. The 10 dB directional coupler is used to couple the part of the input power to the commercial sensor-meter combination (VDI Erickson PM5) [10] connected at Port 3, indicating a reference power. The shielded sensor A and B are connected at Port 2. The Ohm-meters are connected to sensors A and B to measure the resistance. The setup is the same for all the following measurements. The sensor and measurement setup were connected 24 hrs prior to the measurement to reach and settle down at the thermal equilibrium.

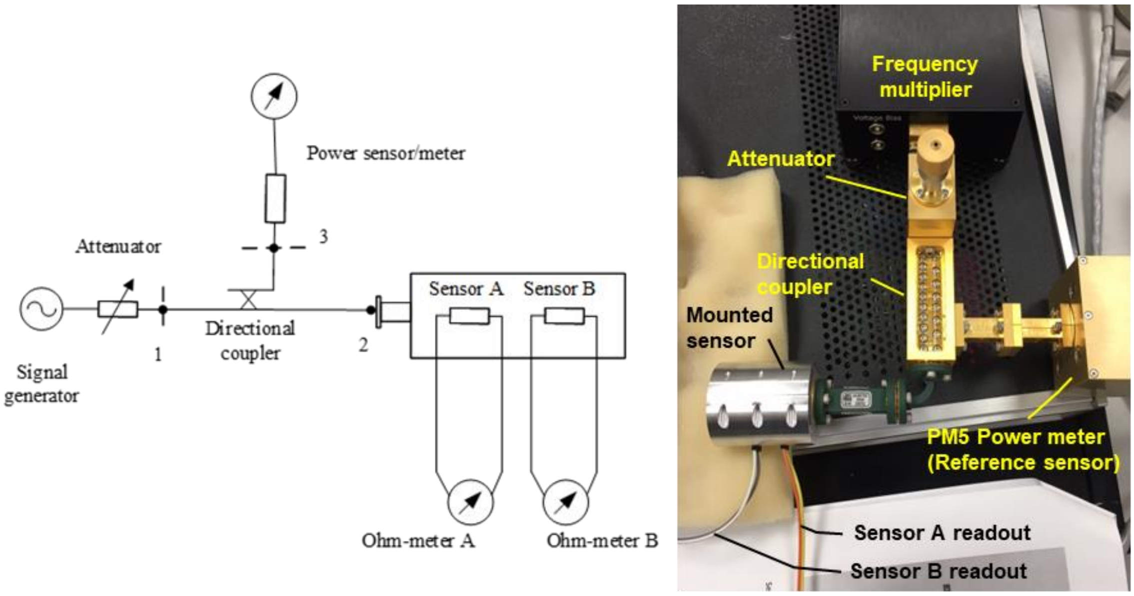

(a) (b)

Figure 4.21 Measurement setup (a) schematic, (b) actual.

The measurement is undertaken for power off and on sequence, respectively, at 140 GHz. The centre frequency of 140 GHz is chosen due to the relatively low S_{11}. The measurement process started by recording the resistance of sensors A and B using Ohm-meters for approximately 175 minutes with the power off. Then, the power is applied, and the reading from the Ohm-meter and the power meter is observed. The measurements are recorded with a time interval of 2.6 s. It should be noted that the time interval is the shortest time the measurement system can reach and is limited by the response of the Ohm-meters, computer, and cable delays.

The resistance ratio of sensor A to sensor B (A/B) is taken to remove any ambient temperature effect [24] on sensor A due to the surrounding environment so that pure dependence on input power can be obtained. The resistance ratio (A/B) is the ratio of resistance shown by sensor A to the sensor B. The resistance ratio and reference power with respect to time are plotted in Figure 4.22. With the typical measurement time being 2 minutes, the test interval of approximately 125 s is opted to estimate sensor response time and the deviation.

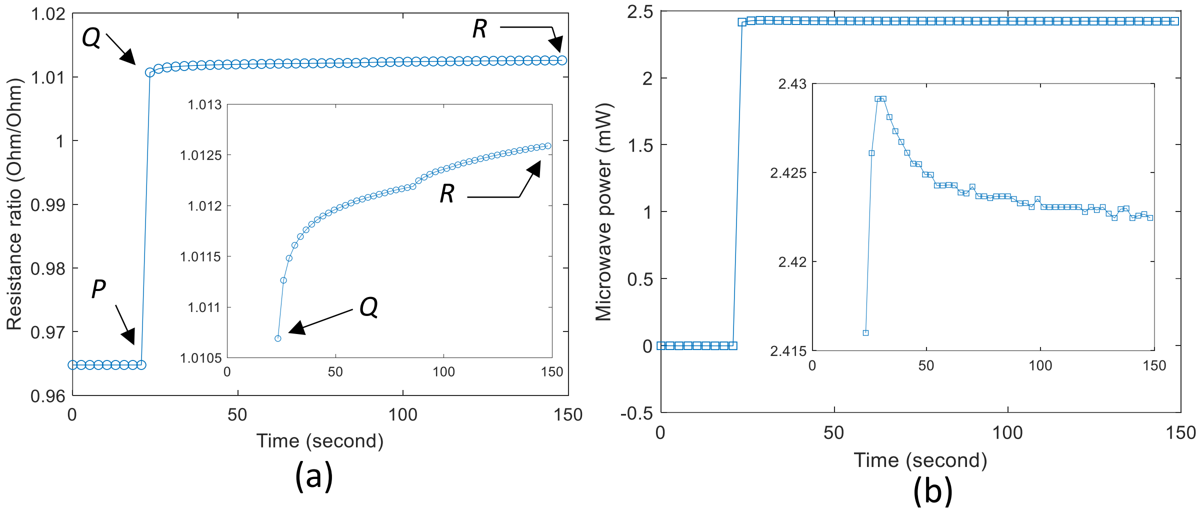

Figure 4.22 Short-term time response: (a) mounted sensor. The inset shows the resistance ratio for the power-on period. (b) the commercial sensor. The inset shows the microwave power for the power-on period.

The three data points are monitored in short-term time response to estimate the sensor's response time. Point *P* indicates the resistance ratio before the power was applied, the next point *Q* indicates the resistance ratio immediately after power is applied (at ~ 25 s), and point *R* indicates the ratio when the sensor is settled (at ~ 150 s). The three data points have values as $P = 0.9648\ \Omega/\Omega$, $Q = 1.0107\ \Omega/\Omega$ and $R = 1.0126\ \Omega/\Omega$.

The time interval between *P* and *Q* data points is 2.6 s, the measurement system limit. The resistance ratio for 90 % of the response can be calculated as,

$$\left[(R-P)\times\frac{90}{100}\right]+P = 1.00782\ \Omega/\Omega \tag{4.1}$$

The resistance ratio for 90 % of the response falls between points *P* and *Q*, indicating the sensor's response time is shorter than 2.6 s.

The 90 % response time for the PM5 power meter is 0.2 sec (20 mW scale) [102][10]. However, the basic sensor in PM5/PM5B has a time constant of 6 s, and feedback electronics have been utilised to improve the response time [102]. In contrast, the designed sensor is raw, and the estimated response time (< 2.6 s) is competitive with commercial PM5.

To further understand the short-term time response of the mounted sensor compared to commercial PM5 sensor, the deviation in response during power on time interval of 125 s (150 s - 25 s) is calculated using (4.2) and given in Table 4.3.

$$Deviation = \frac{Final\,Measurement - Initial\,Measurement}{Initial\,Measurement} \times 100 \tag{4.2}$$

Similarly, the deviation for the commercial sensor is also calculated and presented in Table 4.3. The mounted sensor shows a resistance ratio of 1.0107 **Ω/Ω** and 1.0126 **Ω/Ω** at 25th and 150th s, respectively. The commercial sensor measures power of 2.415999 mW and 2.422447 mW at 25th and 150th s, respectively. The deviation in the resistance ratio and the measured power calculated using (4.2) are 0.19 % and 0.27 %, respectively. This shows that the mounted sensor's deviation is similar to the commercial sensor, and the mounted sensor is working excellently.

Table 4.3 Deviation in short-term time response of the mounted and commercial sensor.

Time (sec)	Mounted sensor resistance ratio (A/B) (Ω/Ω)	Commercial sensor power (mW)
25	1.0107	2.415999
150	1.0126	2.422447
Deviation (%)	0.19	0.27

4.4.3 Long-term time measurement

The long-term time measurements are performed to analyse how the mounted sensor behaves over multiple power on-off switching with longer time periods. The setup for this measurement is the same as shown in Figure 4.21. The measurement sequence is powering off-on-off-on-off, respectively, with a power-on time duration of 175 min and a power-off time duration of 175 minutes.

As before, the resistance ratios are recorded for mounted sensors with a time interval of ~ 2.6 sec. The reference sensor (PM5 power meter) also recorded the power simultaneously. The behaviour of both sensors over multiple on-off cycles is plotted in Figure 4.23.

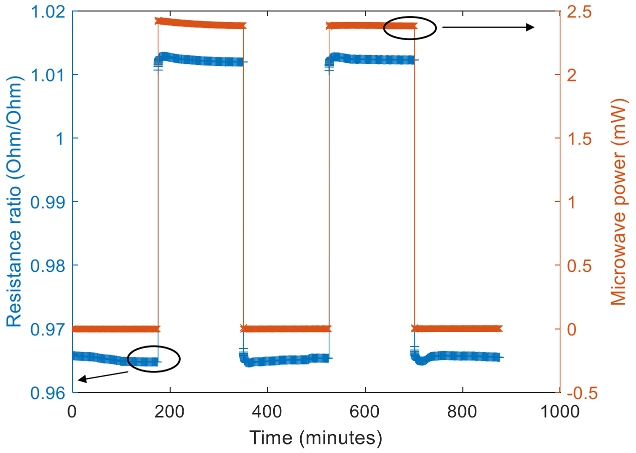

Figure 4. 23 Long-term time response of the mounted sensor and commercial sensor.

To evaluate the working mounted sensor in comparison to the commercial sensor, the average or mean ($\bar{x}$) and standard deviation (s) are calculated by (4.3) [146], [147]. There are 4050 measurement data points or samples (n) in each power-on and power-off sequence (of 175 min). The calculated average and standard deviation for the designed and commercial sensors are given in Table 4.4.

$$s = \sqrt{\frac{\sum_{i=1}^{n}(x_i - \bar{x})^2}{n-1}} \tag{4.3}$$

where,

x_i is each value from the sample,

$\bar{x} = \frac{x_1+x_2+\cdots+x_n}{n}$ is the sample mean or average,

n is the size of the sample.

Table 4.4 Average and standard deviation in long-term time response of the mounted and commercial sensor.

	Average ($\bar{x}$)		Standard deviation (s)		Standard deviation ratio	
Sequence (175 min. each)	Reference sensor microwave power (mW)	Mounted sensor resistance ratio (Ω/Ω)	Reference sensor microwave power (mW)	Mounted sensor resistance ratio (Ω/Ω)	Reference sensor (%)	Mounted sensor (%)
Power off-1	-0.00198	0.96516	0.00028	0.00035		
Power on-1	2.39733	1.01226	0.01162	0.00028	0.484	0.594
Power off-2	-0.00080	0.96506	0.00049	0.00023		
Power on-2	2.38455	1.01240	0.00149	0.00016	0.062	0.338
Power off-3	0.00101	0.96559	0.00043	0.00024		

The difference between the on and off parameters in the average ($\Delta\bar{x}$) is more meaningful. This difference is 0.04709 Ω/Ω and 0.04734 Ω/Ω for mounted sensors in the first and second on-off sequences, respectively. It is 2.39931 mW and 2.38535 mW for the reference sensor in the first and second on-off sequences. However, the average ($\bar{x}$) or the difference in average ($\Delta\bar{x}$) is not directly peer-to-peer comparable as the mounted sensor measures resistance ratio (in Ω/Ω) and the reference sensor measures power (in mW), which are two different quantities having different units. Similarly, just a standard deviation is not directly comparable. Instead, the ratio of standard deviation in power on sequence to the calculated differences ($\Delta\bar{x}$) is a more meaningful indicator for directly comparing performances between the reference sensor and mounted sensor. The standard deviation ratio (SDR) is calculated as follows,

$$SDR = \frac{s}{\Delta\bar{x}} \times 100\% \tag{4.4}$$

The standard deviation ratios for the mounted sensor are 0.594 % and 0.338 % in the first and second power-on sequences, whereas 0.484 % and 0.062 % for the reference sensor. This shows that the deviation of the mounted sensor is less than 0.6 %, similar to the commercial PM5 sensor.

4.4.4 Frequency response

The frequency response (F_R) measurements are performed to analyse how the sensor responds to the applied input power at different frequencies. The frequency response is the transfer function of the mounted sensor derived by NPL, London, for the system setup in Figure 4.21. It is defined as the change in resistance ratio (ΔR) with respect to the incident power on the mounted sensor (P_{MS}). It takes into account the frequency-dependent parameters that affect the input power reaching the mounted sensor and given as,

$$F_R = \frac{\Delta R}{P_{MS}} = EE \frac{\Delta R}{P_{STD}} \frac{|S_{31}|^2}{|S_{21}|^2} \frac{(1 - |\Gamma_{STD}|^2)}{(1 - |\Gamma_{MS}|^2)} \frac{|1 - \Gamma_2 \Gamma_{MS}|^2}{|1 - \Gamma_3 \Gamma_{STD}|^2} \tag{4.5}$$

where,

P_{STD} is a measured microwave power from the power sensor/meter,

ΔR is a difference between resistance ratios for microwave off and on for sensor A and sensor B,

EE is an effective efficiency of the power sensor/meter combination,

S_{31} and S_{21} are voltage transfer coefficients from Port 1 to Port 3 and Port 1 to Port 2, respectively,

Γ_{MS} is a voltage reflection coefficient of the mounted sensor,

Γ_{STD} is a voltage reflection coefficient of the power sensor/meter,

Γ_2 and Γ_3 are voltage reflection coefficients for Port 2 and Port 3 of the directional coupler, respectively.

Initially, for the power off, sensor A and sensor B resistances and reference microwave power are measured with 150 samples and averaged. Then, the power is applied with incremental frequency from 110 to 170 GHz at 5 GHz steps. The parameters mentioned above are measured at each frequency point after 3 minutes of waiting time. The resistance ratio for sensor A and sensor B is calculated, including power off. The difference in the resistance ratio between power on and off at respective frequency points is calculated as ΔR parameter. Figure 4.24 illustrates the measured change in resistance ratio (ΔR) and the measured reference power (P_{STD}).

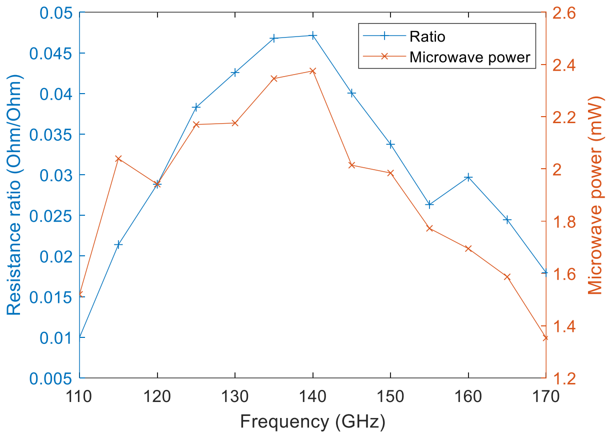

Figure 4.24 Change in resistance ratio and microwave power indicated by mounted and commercial sensors, respectively.

The measurements are repeated for more waiting time intervals consisting of 1, 3, 5, 30, 60, and 120 minutes to quantify the deviation in the transfer function. Sensor A and B resistance and reference power are recorded during the measurement. The difference in resistance ratio ΔR and the measured reference power (P_{STD}) are used in (4.5) to calculate the frequency response. Figure 4.25 (a) shows the frequency response at different waiting time intervals. The average of all the measurements at each frequency point and the standard deviation is calculated and plotted in Figure 4.25 (b). The minimum standard deviation is 0.36 % at 115 GHz, and the maximum one-sigma standard deviation is 0.66 % at 135 GHz. This shows the mounted sensor has a very good reproducible frequency response between 1 minute and 120 minutes.

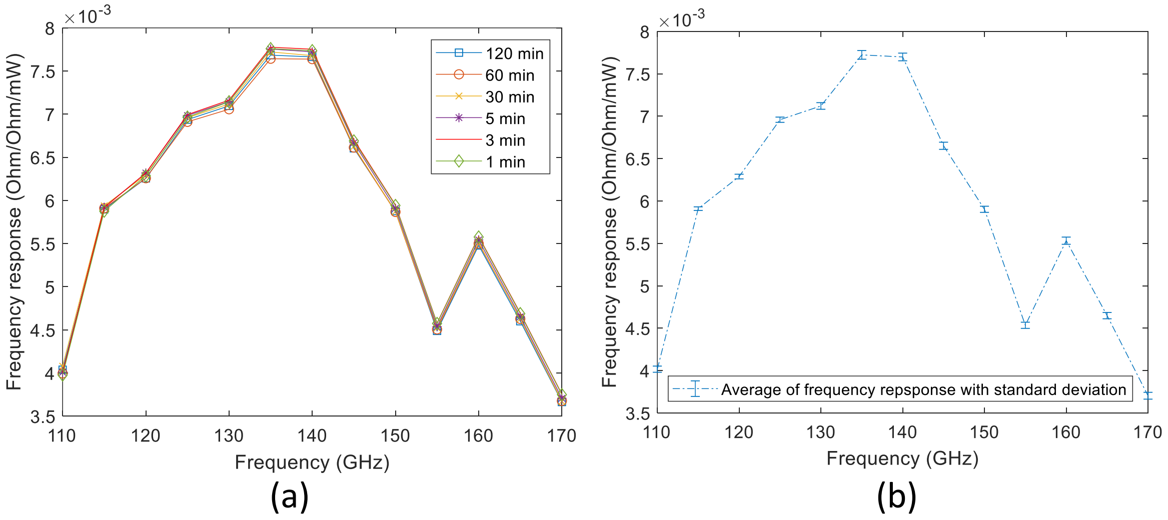

Figure 4.25 Frequency response of mounted sensor (a) at different waiting time intervals, (b) its average with standard deviation.

4.4.5 Linearity

The linearity measurement is performed to analyse how sensors respond to various power levels at a single frequency. This reveals the dynamic range of the sensor with certain deviations from linearity. The measurement setup is the same as in Figure 4.21.

The microwave power is applied from -10 dBm to +9 dBm (indicated by reference sensor at 140 GHz) at each frequency from 110 GHz to 170 GHz at 5 GHz steps. The resistance of sensor A and sensor B and reference microwave power P_{STD} are measured at each frequency point. The microwave power incident upon the mounted sensor is calculated from the measured resistance ratio and already-known frequency response (Figure 4.25 (b)) using (4.5).

The difference between measured reference microwave power P_{STD} and the corresponding calculated incident microwave power P_{MS} is a more meaningful response of the mounted sensor. This response is plotted with respect to an arbitrarily chosen reference microwave power of +5 dBm, and the deviation from the reference can be seen in Figure 4.26. The deviation ranges between ±1.5 dB and ±0.6 dB for the power level between -10 dBm and -3 dBm. It remains within ±0.25 dB for power levels above -3 dBm. A similar deviation can be observed at higher power (> 0 dBm) if the reference point of -5 dBm is chosen. The deviation is highest at 110 GHz due to the relatively high reflection coefficient.

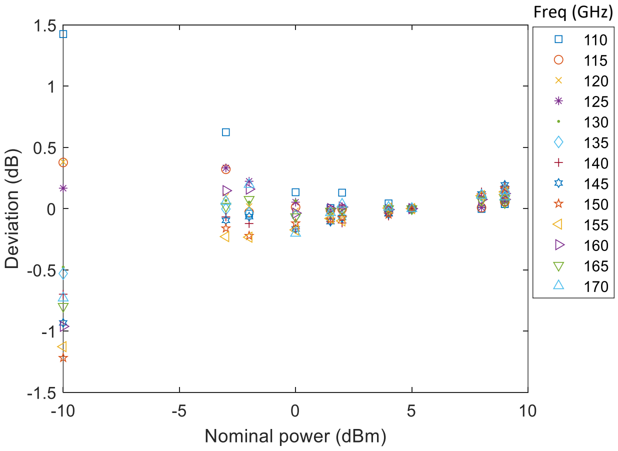

Figure 4.26 Linearity of the mounted sensor.

4.5 Summary

The double-line design progressed in five stages toward the final design while analysing the effect of structural changes on the reflection coefficient (Γ or S_{11}). The rectangular shape substrate is chosen over a T-shape for ease of fabrication. The spring-loaded DC pin and Dupont wire head mainly define the dimensions of the rectangular substrate. The width of the substrate or sensor chip determines the S_{11} of the final design, and the gaps around it introduce spurious resonances.

The dual sensor configuration is implemented for ambient temperature compensation, where the resistance ratio eliminates ambient temperature dependence. The sensor bodies are covered in double-layer shielding (PEEK-inner, aluminium-outer) to reduce ambient temperature effects and for ease of handling. The polyimide tape is applied to the sensor chip, and detector bodies are fabricated in PEEK; all these measures are for better thermal insulation. The aluminium shielding gives the final dimension to the detector, which has a size of 35 mm × 41 mm (outer diameter × length) and is comparable to the commercial PM5 sensor of size 51 mm × 48 mm× 76 mm [102][10].

The designed bolometric power detector/sensor (sensors A and B inside the shielding) is characterised and compared with the commercial power sensor, PM5 [102][10]. The reflection coefficient of the fabricated detector agrees with the simulation. The relative standard deviation in short-term and long-term time measurements is used to compare designed and commercial sensor performances directly. The deviation in short-term time measurement is 0.19 % and 0.27 % for the designed and commercial sensors, respectively. The deviation in long-term time measurement for the designed sensor is less than 0.6 %, similar to the commercial sensor. The 90% response time for the designed sensor is less than 2.6 s (measurement system limit). The frequency response shows the sensor has very good reproducibility with a one-sigma standard deviation of 0.66 %. The detector is linear with a deviation of ± 0.25 dB for power levels above -3 dBm; however, the deviation is ±1.5 dB and ±0.6 dB for power levels between -10 dBm to -3 dBm. The bolometric power detector's portable size and competitive performance qualify the detector as a transfer standard/working standard. The comparison with other power standards using the working frequency band of the basic mount in the waveguide, matching type, response time and other attributes, such as power scales, is given in Table 2.1.

CHAPTER 5

SCHOTTKY DIODE POWER DETECTOR

This chapter discusses a power detector design based on a zero-bias Schottky diode in D-band (110-170 GHz). The chapter starts with the theoretical background and fundamentals of power detection. The design of individual elements such as lowpass filter (LPF), waveguide to microstrip (W-to-M) transition, diode simulation and matching circuit are discussed. The chapter discusses an approach to designing a W-to-M transition by stepping down the width of the 50 Ω microstrip line. The complete detector is designed in CST, and its S-parameters (scattering parameters) are exported to Keysight Technologies ADS (advanced design system) for non-linear simulations. Finally, detector fabrication and measurement are presented.

5.1 Schottky Diode Theory

The Schottky diode is two terminal devices made of a metal and semiconductor junction, which was first realised by F. Braun when he was experimenting with galena crystal in 1874 [148]. He noticed the rectification behaviour of such a junction but could not explain the working principle. More than half a century later, in 1938, Walter H. Schottky conducted pioneering research in metal-semiconductor junctions [149]. He postulated the theory of space charge region or the barrier formation in the metal-semiconductor junction, now known as the Schottky barrier. Later, more theories came forward to explain the working principle of metal-semiconductor junctions, detailed in [150].

In the metal-semiconductor junction, the semiconductor could be n-type or p-type doped. GaAs and Si have a large amount of experimental data available on Schottky contact [150]. The n-GaAs semiconductor material is preferred at higher frequencies due to its high electron mobility [88], [151], and metals such as titanium and gold are evaporated to form a Schottky junction [152]. The Schottky diode is the majority charge carrier device, unlike the p-n junction diode; therefore, it has an inherently fast response [88], [89].

5.1.1 Energy band diagram

When the metal and n-type semiconductor junction is formed, the electrons diffuse from semiconductor to metal, leaving net positive charges (space charge, Q_{SC}) behind in the depletion region and forming net negative charges on the metal surface. The depletion region is mainly spread inside the semiconductor and negligible on the metal side as the semiconductor has low charge carrier concentration (electrons for n-type and holes for p-type) compared to the high electron density of the metal. The electron diffusion, hence, the band bending, occurs until the Fermi energy of the metal (E_{Fm}) and the semiconductor (E_{Fs}) lines up; that is, it reaches the thermal equilibrium condition. This band bending gives rise to built-in potential (ψ_{bi}) and Schottky barrier (ϕ_b), as shown in Figure 5.1. The built-in potential opposes further diffusion of electrons into the semiconductor, and Schottky barriers resist the reverse flow of electrons from the metal to the semiconductor [88].

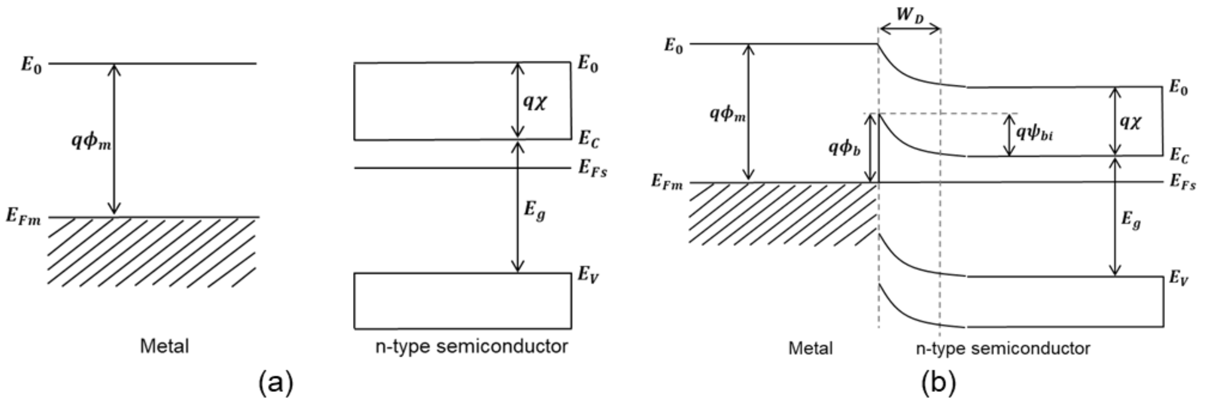

Figure 5.1 The energy band diagram of a metal-n-type semiconductor junction (a) before the contact, (b) after the contact and no bias.

The Schottky barrier height is generally a difference between the metal work function (ϕ_m) and electron affinity (χ) of the semiconductor without considering a minor image force lowering.

$$q\phi_b = q(\phi_m - \chi) \tag{5.1}$$

The metal work function is defined as the energy required for the electron at the fermi level to escape to the vacuum. The metal work function depends on various factors, such as the metals' electronic structure and surface condition (contamination). Titanium has ϕ_m= 4.33 eV, and gold has ϕ_m= 5.38 eV [153]. The electron affinity in the semiconductor is the energy difference between the vacuum level and the lowest energy state of the conduction band.

The width of the depletion region W_D is given by equation (5.2) and depends on the applied voltage across the junction [88].

$$W_D = \sqrt{\frac{2\varepsilon_s}{qN_D}\left(\psi_{bi} - V - \frac{kT}{q}\right)} \tag{5.2}$$

where, ε_s is the permittivity of the semiconductor, q is the charge of an electron, N_D is an ionised doping concentration in the case of an n-type semiconductor, ψ_{bi} is the built-in potential or diffusion potential, V is the bias voltage (either forward V_F or reverse V_R), k is the Boltzmann constant, T is the absolute temperature in Kelvin.

The Space charge Q_{SC} formed in the depletion region after the diffusion is given by [88],

$$Q_{sc} = S \cdot qN_D W_D = S \cdot \sqrt{2q\varepsilon_s N_D\left(\psi_{bi} - V - \frac{kT}{q}\right)} \tag{5.3}$$

where S is the diode's junction area or anode contact area.

Junction capacitance established between two electron-occupying regions (metal and n-semiconductor) separated by depletion region is [88],

$$C_j = S\frac{\varepsilon_s}{W_D} = S \cdot \sqrt{\frac{q\varepsilon_s N_D}{2\left[\psi_{bi} - V - \left(\frac{kT}{q}\right)\right]}} \tag{5.4}$$

The built-in potential is reduced when applying forward bias voltage (V_F) across the junction, allowing electrons to flow from semiconductor to metal. In reverse bias (V_R), the built-in potential increases, so electrons cannot pass the large potential barrier. The corresponding band diagrams are shown in Figure 5.2. The depletion region width reduces for forward bias and increases for reverse bias, as stated in (5.2).

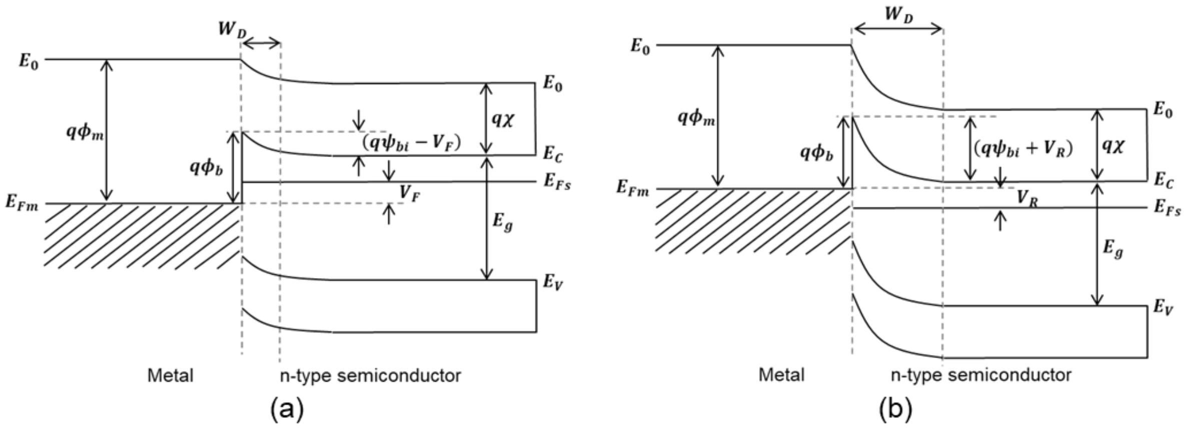

Figure 5.2 The energy band diagram (a) after forward biasing the junction, (b) after reverse biasing the junction.

In forward bias, the electron overcoming the potential barrier higher than the Fermi level of the metal is called thermionic emission, also known as hot carriers [154]. Electrons are also tunnelling through the thin width of the Schottky barrier, which is called tunnelling current. The total current flowing through the diode is thus given by [88],

$$I = I_S\left[exp\left(\frac{qV}{\eta kT}\right) - 1\right] = I_S[exp(\alpha V) - 1] \tag{5.5}$$

where,

$$I_S = SA^{**}T^2 exp\left(\frac{q\phi_{Bn}}{kT}\right) \tag{5.6}$$

where, η is the ideality factor, A^{**} is the reduced effective Richardson constant.

5.1.2 Equivalent circuit

The Schottky diode equivalent circuit consists of the junction resistance *Rj*, junction capacitance *Cj*, series resistance *Rs* at its core, and other parasitic elements, as shown in Figure 5.3. The nonlinearity of *Rj* is used for rectification/detection, and *Cj* for multiplier application [152]. The electronic components at higher frequencies suffer from parasitic loss as the wavelength becomes comparable to the physical dimension. The Schottky diode physical structure consists of an anode finger/air bridge, which acts as an inductance L_f. The trench under the finger acts as a pad-to-pad capacitance C_{pp}. The other capacitance can exist between the finger and the epilayer C_{fp}; and between the finger and Ohmic contact C_{foh}. In practice, every element has resistive loss associated with it, such as anode finger resistance *Rp*, Ohmic contact resistance *Roh*, and un-depleted Schottky layer resistance *Rsl*, adding up to a total resistance called diode series resistance *Rs* [5].

The cut-off frequency of the Schottky diode is given by,

$$f_c = \frac{1}{2\pi C_j R_s} \tag{5.7}$$

The diode can work at a higher frequency if the junction capacitance and parasitic series resistance are reduced by optimising its dimension. The series resistance is mainly associated with carrier mobility; higher carrier mobility gives smaller series resistance [88]. The cut-off frequency can also be defined as more application-specific in practice and can be improved by lowering parasitic capacitances [5].

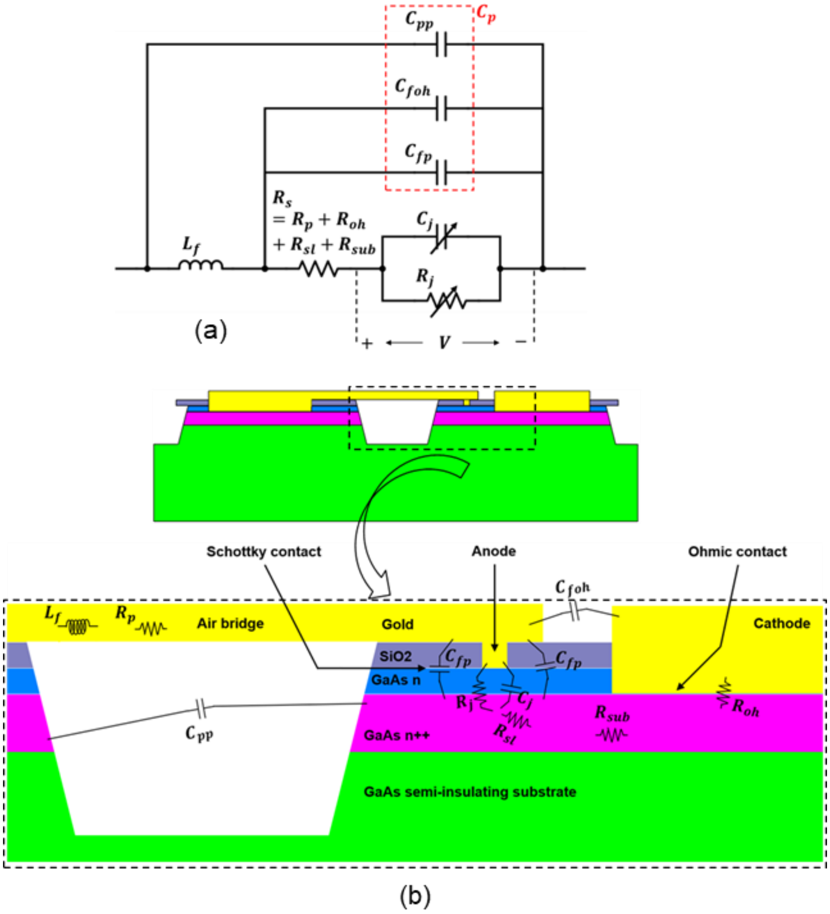

Figure 5.3 (a) equivalent circuit of a Schottky Diode, adapted from [5], (b) Schottky diode schematic with parasitics.

5.1.3 Diode power detector

The I-V characteristic of the diode is divided into non-linear (square law) and linear regions for small signal and large signal conditions, respectively. The general diode current equation (5.5) can be expanded in simplified power series as,

$$I = I_S(\alpha V + \frac{(\alpha V)^2}{2!} + \frac{(\alpha V)^3}{3!} + \cdots) \tag{5.8}$$

$$V = V_{Peak} \cdot cos(\omega t) \tag{5.9}$$

$$I = I_S\ (\alpha V_{Peak} \cdot cos(\omega t) + \frac{\alpha {V_{peak}}^2}{2}\{1 + cos(2\omega t)\} + \cdots) \tag{5.10}$$

where, V_{Peak} is the peak voltage of the input RF waveform.

Equation (5.10) shows that the frequency spectrum of the output of a diode detector contains DC (direct current or 0 Hz), fundamental and higher-order harmonics with reduced power compared to the fundamental frequency.

The DC component of the diode current is proportional to the square of input voltage that is equivalent to input power. So, the voltage drop across the load resistance at the output will be proportional to the input power. The power detector can be realised based on these basics, as shown in Figure 5.4. The detectors will be for waveguide-based applications, as discussed in Section 2.3. Therefore, the Waveguide-to-Microstrip (W-to-M) transition is required at the input. As discussed earlier, diodes suffer from parasitic losses, and a matching circuit is necessary to transfer the maximum power to the junction. The frequency components, including generated harmonics in the diode current, can be shorted using a filter at the output, and only the DC component proportional to the input power is used for readout. The current return path (CRP) is a lowpass filter at the input, which completes the DC loop.

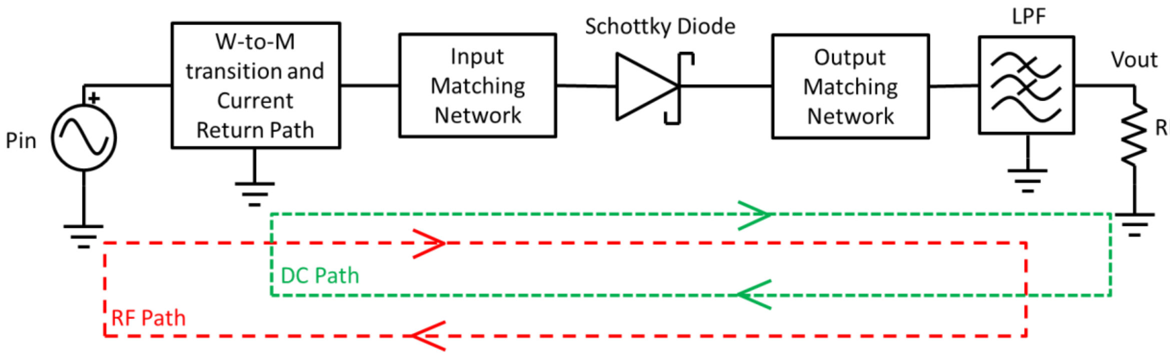

Figure 5.4 Basic block diagram of the power detector circuit.

The steps that are followed toward the design are shown in Figure 5.5. The first two steps are essential to estimate substrate and channel dimensions. The substrate width depends on the broader line of the stepped impedance filter. This also sets the waveguide channel width; therefore, the lowpass filter (LPF) is first in the design step. The waveguide channel height depends on the W-to-M transition and current return path to achieve good coupling of microwave energy to the microstrip line. Therefore, the transition is designed in the second step. Once the substrate and channel dimensions are fixed, these can be used in the following steps towards the final design.

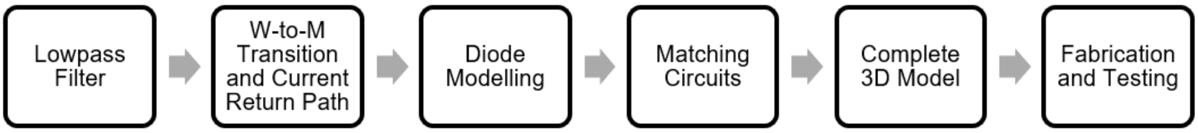

Figure 5.5 Design process for power detector.

The detector's performance is characterised by observing the reflection coefficient or return loss (S_{11}) and the responsivity. Responsivity is the DC voltage detected at the output per unit RF input power, and its unit is V/W or mV/mW.

5.2 Lowpass Filter Design

The output of a non-linear diode consists of undesired frequency components (fundamental and harmonics). The lowpass filter is necessary to filter out these frequency components (especially high-power fundamentals) and only allow DC to pass. The microstrip stepped impedance filter is common and straightforward to design, where the sharp rejection/roll-off of the stop band is not required. The stepped impedance filter consists of cascaded low and high impedance sections. The prototype lowpass filter is shown in Figure 5.6. In the prototype circuit, the shunt capacitor and series inductor can be realised using the short microstrip line ($\beta \cdot l < \pi/4$) with low characteristic impedance Z_l and high impedance Z_h, respectively [128]. The L and C are normalised inductance and capacitance values, also known as g_k values, where k = 0 to N+1 and N is the order of the filter or the number of elements.

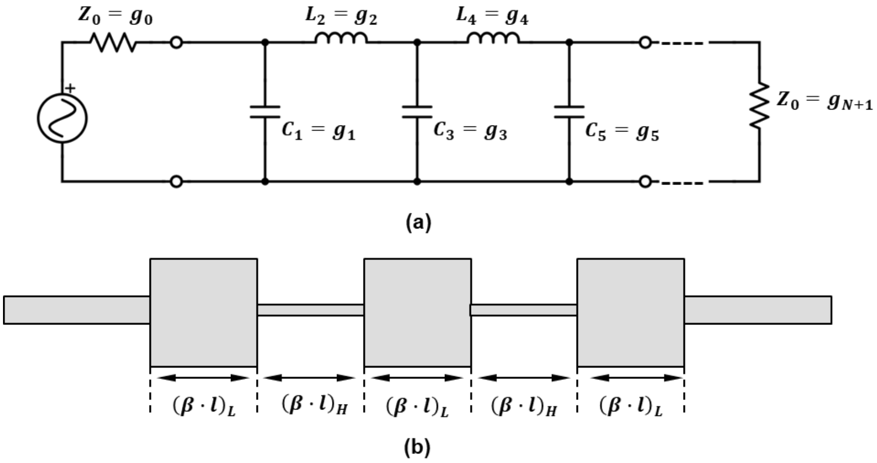

Figure 5.6 (a) N^{th} order lowpass filter prototype and the corresponding, (b) 5^{th} order stepped impedance filter, adapted from [128].

The practical low impedance Z_l and high impedance Z_h can be approximately 20 Ω and 120 Ω, respectively. The low-impedance line is wider, determining the substrate width. The high-impedance line has a narrow width, which is limited by the fabrication capability.

Quartz substrate ($\varepsilon_r = 3.75$) with a thickness, h = 50 µm is considered for this design. First, the width of each section needs to be chosen to get the corresponding high and low impedance, which can be done with the following steps.

The aspect ratio can be calculated by (5.11) after choosing the width of filter sections,

$$x = \frac{h}{w}\,. \tag{5.11}$$

The effective permittivity can be calculated as [155],

$$\varepsilon_{eff} = \frac{\varepsilon r+1}{2} + \frac{\varepsilon r-1}{2}\left(\sqrt{\frac{1}{1+12\cdot x}} + 0.04\cdot\left(1-\frac{1}{x}\right)^2\right) \qquad \{x > 1\} \tag{5.12}$$

$$= \frac{\varepsilon r+1}{2} + \frac{\varepsilon r-1}{2}\cdot\sqrt{\frac{1}{1+12\cdot x}} \qquad \{x \leq 1\}. \tag{5.13}$$

The characteristic impedance of the line for the chosen width, for any x, is [155],

$$Z = \frac{\eta_0}{2 \cdot \pi \cdot \sqrt{2 \cdot (\varepsilon r + 1)}} \cdot ln\left(1 + 4 \cdot x\left(\frac{14 \cdot \varepsilon r + 8}{11 \cdot \varepsilon r} \cdot 4 \cdot x + \sqrt{\left(\frac{14 \cdot \varepsilon r + 8}{11 \cdot \varepsilon r}\right)^2 \cdot (4 \cdot x)^2 + \left(1 + \frac{1}{\varepsilon r}\right) \cdot \frac{\pi^2}{2}}\right)\right). \tag{5.14}$$

where, the constant $\eta_0 = \sqrt{\frac{\mu_0}{\varepsilon_0}} \approx 377\ \Omega$.

The width of 500 µm is chosen for the low impedance line (calculated as 15.88 **Ω**), so the substrate width is chosen to be 600 µm considering 50 µm clearance on either side. This substrate width is assumed to be sufficient to accommodate other distributed matching elements and also feasible for the W-to-M transition covered in the following sections. The width of 25 µm is chosen for the high impedance line (calculated as 102.16 **Ω**) to not strain on the fabrication.

The large order of the filter gives a better response, but the circuit on the substrate gets longer, so the 5th order Chebyshev filter with 0.5 dB ripple factor is considered for the design. The ripple factor here is not crucial unless a sharp cut-off frequency is expected at the expense of ripples in the pass band [128]. The element values for the 0.5 dB Chebyshev filters are $g_0 = g_6 = 1$, $g_1 = g_5 = 1.7058$, $g_2 = g_4 = 1.2296$, $g_3 = 2.5409$. The electrical lengths of the low and high lines can be calculated using the following equations [128],

$$(\beta \cdot l)_L = \frac{C \cdot Z_l}{Z_0} = \frac{g_k \cdot Z_l}{Z_0} \quad \text{where k is even, 1,3,5,...} \tag{5.15}$$

$$(\beta \cdot l)_H = \frac{L \cdot Z_0}{Z_h} = \frac{g_k \cdot Z_0}{Z_h} \quad \text{where k is odd, 2,4,6,...} \tag{5.16}$$

The general equation for electrical length is [128],

$$\beta \cdot l = \frac{\omega_c}{V_P} = \frac{\omega_c \cdot \sqrt{\varepsilon_{eff}}}{c} \cdot l = \frac{2\pi f_c \cdot \sqrt{\varepsilon_{eff}}}{c} \cdot l \tag{5.17}$$

Rearranging (5.17) to calculate the physical length (*l*) of the respective lines gives,

$$l = \frac{\beta \cdot l \cdot c}{2\pi f_c \cdot \sqrt{\varepsilon_{eff}}} \tag{5.18}$$

where, f_C is the cut-off frequency, V_P is the phase velocity, ε_{eff} is the effective permittivity, and *c* is the speed of light. The cut-off frequency (70 GHz) is chosen such that the stop band of the filter lies in the fundamental frequency band (D-band, 110-170 GHz). The fundamental frequency band has more power than harmonics and should be suppressed. The calculated values of widths and lengths are given in Table 5.1.

Table 5. 1 Filter dimensions

Line	Width (µm)	ε_{eff}	Impedance (Ω)	βl (rad)	Length (µm)
1	500	3.302	15.88	0.542	200
2	25	2.664	102.16	0.602	250
3	500	3.302	15.88	0.807	300
4	25	2.664	102.16	0.602	250
5	500	3.302	15.88	0.542	200

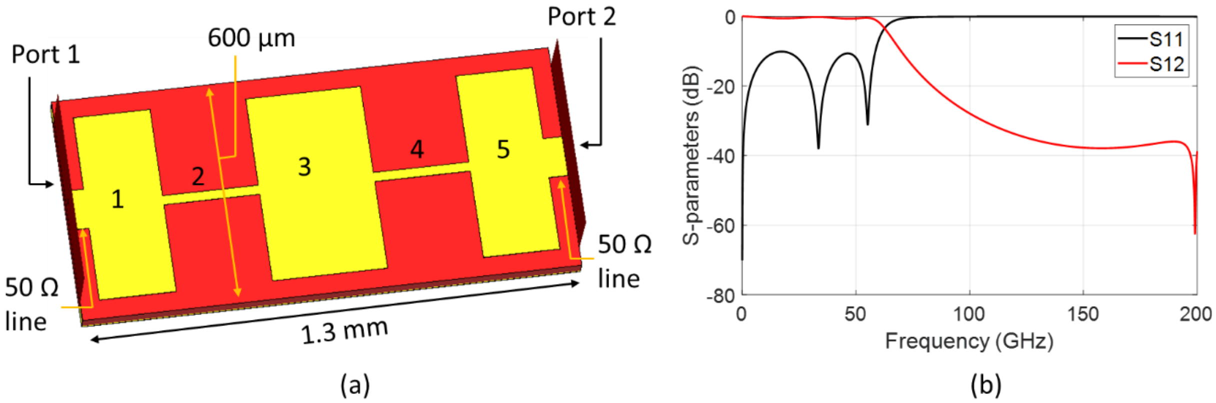

(a) (b)

Figure 5.7 Filter structure and simulated response.

The filter is designed in CST using the dimensions in Table 5.1. The 1 µm thick gold is used for all the microstrip structures in the simulation. The simulated response is shown in Figure 5.7. The filter has a stopband response in the D-band, as expected. The width of the substrate is 600 µm.

It must be noted that, for the sake of the diode detector design, 3D structures in CST must be simulated from 0 Hz (DC) to the required highest frequency, 170 GHz. This will ensure DC information is present in the S-parameter data file. So, when simulated in ADS, the circuit will have a DC path giving the correct DC voltages at the output.

5.3 Waveguide-to-Microstrip (W-to-M) Transition and Current Return Path (CRP)

The waveguide-based power detector needs the W-to-M transition structure to couple the RF energy to the detector circuit on the microstrip line. It consists of a microstrip probe inserted into the E-plane of the waveguide. The E-plane probe couples the TE10 mode of the waveguide to the quasi-TEM mode of the microstrip line. The transition should be wide in bandwidth with minimum insertion loss. The current return path that completes the DC loop is also incorporated in the same structure to reduce the number of separate components exported to ADS in the following sections.

The waveguide to microstrip probe transition [156], [157], [158] is preferred here because of its simplicity and ease of fabrication over the antipodal fin-line [117], [121], [123] and ridge waveguide transitions [159], [160]. The microstrip probe transition is generally an approach of designing a probe, then a high impedance line, and then a quarter wave transformer to match the 50 Ω line. However, here, the approach is stepping down the 50 Ω microstrip lines in two steps and then optimising for a better match. The current return path is also a part of this structure, and the matching response is sensitive to the position of the return path on the microstrip line. The stepped-down approach is intuitively chosen to match the microstrip 50 Ω line to the high impedance of the waveguide.

The W-to-M transition is designed with three sections of lines (50 Ω line, central line and probe) narrowing down into two steps. The width of the 50 Ω microstrip line at 140 GHz can be calculated as 107.3 µm using (5.14). The width of the central line and probe is chosen to be two-thirds (71.50 µm) and one-third (35.76 µm) of the 50 Ω line, respectively. The back-short distance for the probe is generally around a quarter of the guided wavelength (λ_g) in the waveguide, which is 2.8 mm at 140 GHz in the WR06 waveguide, calculated using (3.3), and hence the back-short distance is 700 µm.

The current return path is a narrow line from the main 50 Ω microstrip line to the edge of the substrate. The width of the line is selected as 25 µm. The end of the line has a 75 µm × 75 µm pad for wire bonding. The empty cavity is created in the metal housing opposite the pad, providing space for the bond wire. A line with a 50 µm width resembling a bond wire is used over the pads in the simulation.

The height of the channel, the position of the current return path on the main microstrip line, and the probe and central line widths are optimised to improve the response and are given in Table 5.2.

The W-to-M structure, including the current return path, is shown in Figure 5.8 (a). The structure has achieved a transmission response of better than 0.26 dB and a return loss of more than 15 dB, as shown in Figure 5.8 (b).

The W-to-M transition with the current return path finalises the channel dimension that opens into the waveguide from the top broad wall. The channel is made 50 µm wider on either side of the substrate (width 600 µm). This makes the width of the channel fixed to 700 µm. The height of the channel is 550 µm.

Table 5.2 Parameters for the waveguide to microstrip transition and current return path.

Parameters (µm)	Initial (before optimisation)	Updated (After optimisation)	Difference (µm)
Probe width	35.76	45.76	10 (28 %)
Central line width	71.50	61.50	-10 (-16.26 %)
Central line length	300	350	50 (16.66 %)
CRP position	325	575	250 (77 %)
Channel height	450	550	200 (44.44 %)
Back-short distance	700	700	0 (0%)

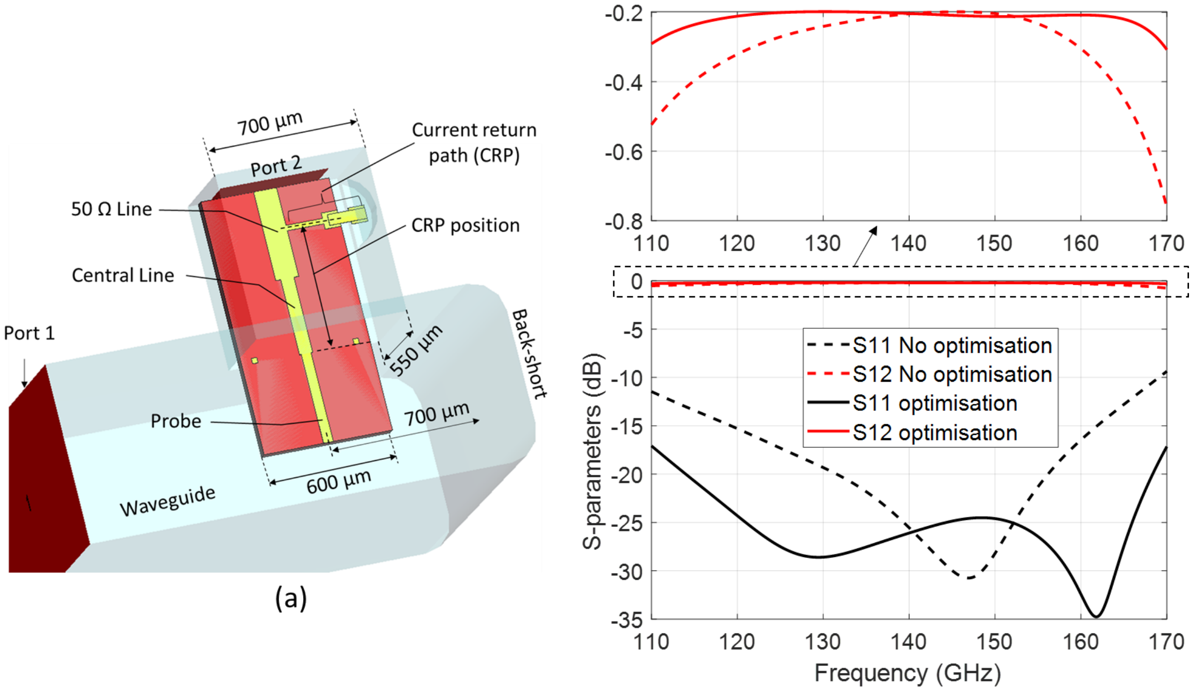

(a)

(b)

Figure 5.8 (a) Waveguide to Microstrip transition with current return path, (b) S-parameters of the corresponding structure.

5.4 Diode 3D Model

The lumped equivalent circuit model of the Schottky diode is not feasible at the high frequencies as the accuracy reduces; hence, the alternative way is to utilise the 3D and Spice models of the diode provided by the manufacturer using the coaxial probe method [161] [162]. The 3D model considers the parasitic losses arising from the diode structure, and the Spice model gives the non-linear characteristic to the diode.

The diode 3D model is implemented on a 50 Ω microstrip line in CST, as shown in Figure 5.9 (a). The length of the 50 Ω line is 52 µm, much shorter than the guided wavelength in the microstrip line (λ_g = 1256 µm at 140 GHz). This avoids impedance transformation over the longer lengths unless the line length is an integer multiple of half wavelength ($\lambda_g/2$), as the impedance repeats in the Smith chart every half wavelength. Microstrip lines on either side of the diode set the reference plane (Ref Planes 1 and 2) around which the detector circuitry would be designed in the next section. The diode is flip-chip mounted on the microstrip line gap of 100 µm, and extra 2 µm thick soldering pads resemble wedge bonding.

The microstrip line on the anode side is assigned as Port 1, the line on the cathode side is Port 2, and Port 3 is set at the anode surface, as shown in Figure 5.9 (b). This technique is called the coaxial probe method, which makes it easy to determine diode embedding impedances without requiring an equivalent circuit [161] [162].

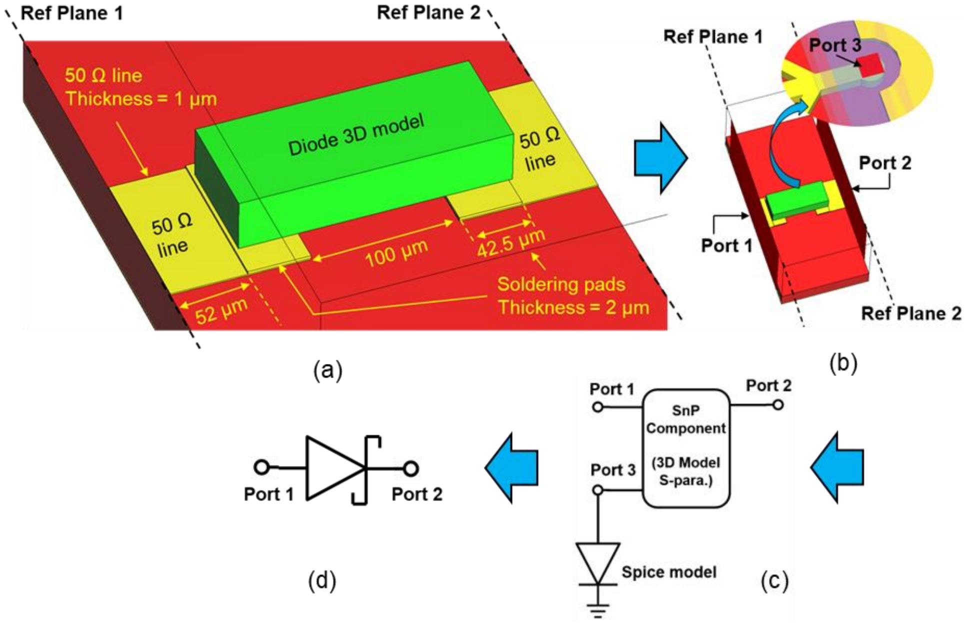

Figure 5.9 (a) diode 3D model on microstrip line in CST, (b) diode port assignation, (c) diode Spice model connected at intrinsic anode Port 3 in ADS, (d) the symbol for the complete diode.

The S-parameters of the three-port diode simulation are exported to the SnP component of ADS, where the Spice (non-linear) model of the Schottky diode is connected to Port 3, as shown in Figure 5.9 (c). The diode 3D model incorporated with the Spice model acts as a complete single diode circuit (Figure 5.9 (d)) to be used for the design.

The diode is connected to the DC voltage source (V_{in}) to simulate the current-voltage (IV) characteristics, as shown in Figure 5.10 (a). The DC voltage is swept from -40 mV to 150 mV, and the corresponding diode current is from a few µA to 700 µA. The IV characteristic of the diode is plotted in Figure 10 (b). The diode current (I_D) nonlinearly depends on the voltage across the diode, and the inset of Figure 5.10 (b) shows the IV curve passes through the origin, indicating a zero bias nature.

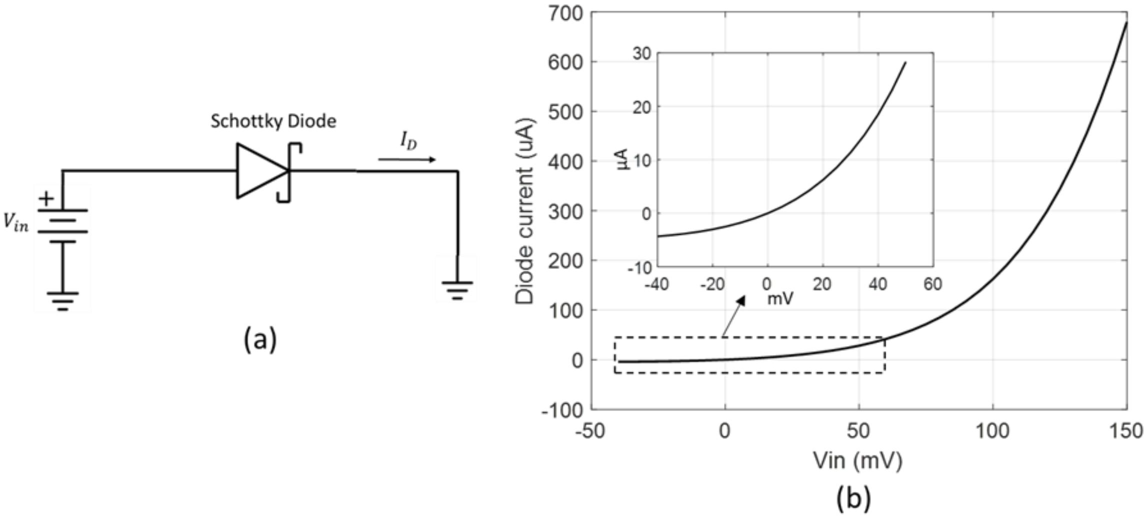

Figure 5.10 (a) Schottky diode connected to DC voltage (b) Schottky diode current-voltage characteristics.

The Schottky diode was terminated with a 50 Ω load resistance (R_L), as shown in Figure 5.11. The source resistance (R_S) is 50 Ω. The simulation was performed, and the input reflection coefficient was plotted in the Smith chart to reveal the input impedance of the diode, as shown in Figure 5.11 (b). The input impedance $Z_{in} = 50 \times (0.299 - j0.493) = 14.95 - j24.65\,\Omega$ at 140 GHz at both reference planes. The rectangular plot of a reflection coefficient of the diode with 50 Ω terminations is plotted later in Figure 5.16, showing its frequency dependence.

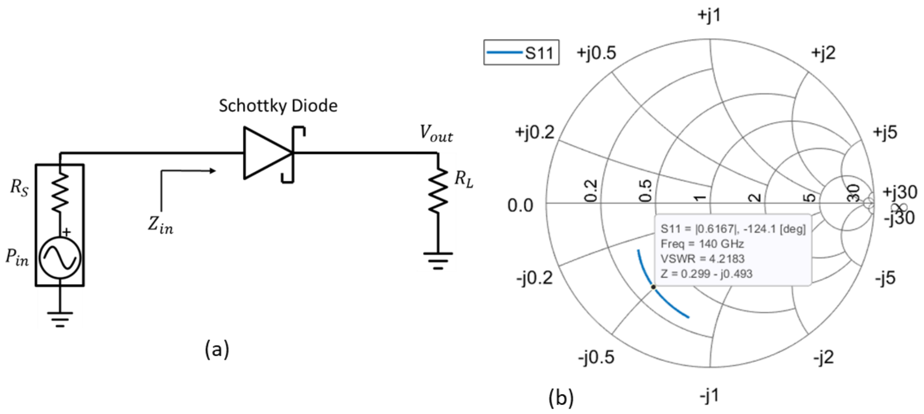

Figure 5.11 (a) schematic circuit to find the diode impedance at reference planes, (b) simulated input reflection coefficient (S_{11}) plotted in Smith Chart.

5.5 Input Matching Circuit

The matching circuit is necessary to match the diode impedance over the full frequency band. It ensures that maximum RF power reaches the diode junction, so the square law operation is performed across the D-band.

5.5.1 Discrete detector circuit

The input impedance of the diode depends on the circuit connected to the output. As discussed in Section 5.1.3, the power detector has a lowpass filter (LPF) and load resistance (R_L) at the output. The load resistance is 1 MΩ, the typical input impedance of the voltmeter. Therefore, before designing the matching circuit, the lowpass filter and load resistance of 1 MΩ are connected at the output, as shown

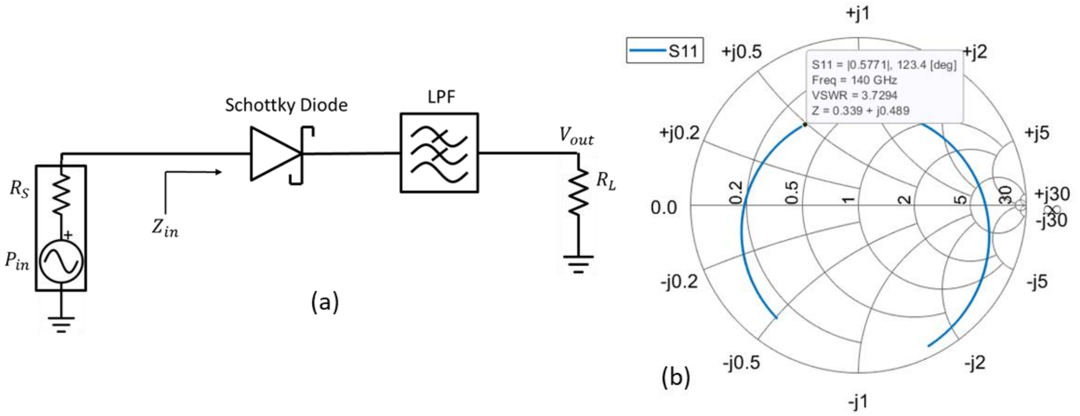

Figure 5.12 (a) schematic circuit to find the input impedance appearing at the reference plane 1, (b) simulated input reflection coefficient (S_{11}) plotted in Smith Chart.

in Figure 5.12. The circuit is simulated to find the input impedance. The input reflection coefficient S_{11} is plotted in the Smith chart, which shows the normalised input impedance ($Z_{in}/50$) at respective frequencies. The impedance of the circuit at 140 GHz is $Z_{in} = 50 \times (0.399 + j0.489) = 16.95 - j24.45\ \Omega$.

ADS's Smith Chart tool can be used for designing matching circuits. The impedance is entered into the Smith chart tool. It has lumped elements and microstrip lines available for design. The stubs are avoided as they may require larger space than available on the substrate. Therefore, a simple matching circuit is desired. The substrate width is fixed at 600 µm, as discussed in Section 5.2.

The matching circuit should bring the input impedance to the centre of the Smith chart. The 50 Ω line always rotates clockwise in the Smith chart with respect to the centre. Whereas a line with characteristic impedance other than 50 Ω will give a clockwise trajectory, the rotation will not be centred at the centre of the Smith chart. A 20 Ω (w = 385.6 µm) microstrip line is added to bring the impedance closer to the centre, as shown in Figure 5.13. However, matching using a single line results in a narrow bandwidth. The reflection coefficient (S_{11}) is narrowed to around 140 GHz and has a 10 dB bandwidth of 6 GHz, as shown in Figure 5.16. The corresponding responsivity is plotted in Figure 5.17. The reflection coefficients (S_{11}) and Responsivity graphs of all the following design stages are plotted in Figure 5.16 and Figure 5.17, respectively. Also, the same figures show the graphs for the diode terminated with 50 Ω and 1 MΩ load. It is seen that the responsivity is better for 1 MΩ termination than for 50 Ω because the voltage drop or the detected voltage across the high load would be higher than the low load.

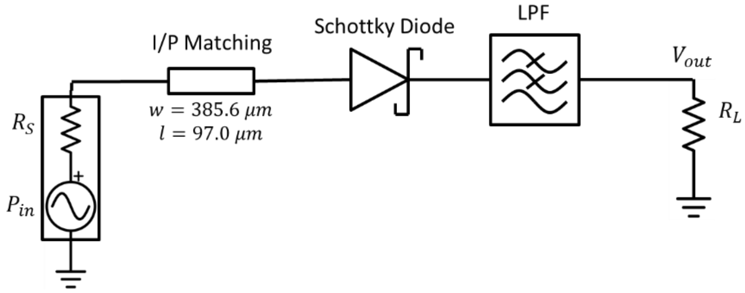

Figure 5.13. Schematic circuit shows input matching using a single microstrip line.

It is preferred to have wideband matching (ideally flat response) by compensating return loss. This will ensure the diode receives similar input power at all frequencies; hence, the responsivity curve would be flat. The second matching line is added in the input matching circuit, and the third matching line is at the diode output, as shown in Figure 5.14. All three lines are tuned for higher return loss (S_{11}) with a flat response. However, the maximum achieved return loss is around 2 dB for the entire band (110 – 170 GHz), as shown in Figure 5.16. It is realised that the matching is challenging to improve further as the diode input impedance is away from the centre of the Smith chart and is highly frequency dependent, as seen in Figure 5.12 (b).

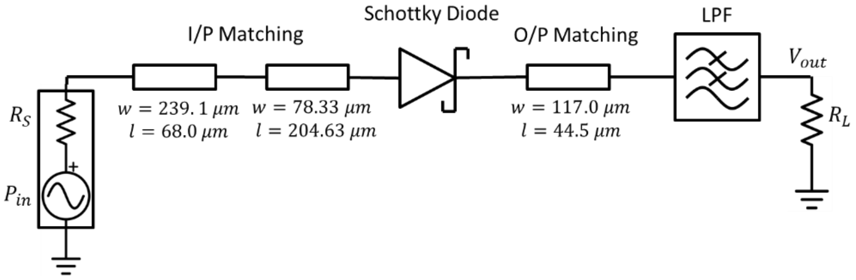

Figure 5.14 Schematic circuit shows a matching circuit using two lines at the input and a single line at the output.

At this stage, the effect of the W-to-M transition and the current return path (CRP) must be considered. The S-parameters of the transition with the current return path (CRP) are exported to the SnP component in ADS, as shown in the schematic of Figure 5.15. The source resistance (R_S) can be set equal to the waveguide characteristic impedance of 495 Ω, calculated using (3.4) at 140 GHz for simplicity, or (3.4) can be written in ADS to consider frequency dependence. Either case has no significant effect on responsivity; therefore R_S is set to 495 Ω during the simulation. The two input matching lines and an output matching line are again optimised for maximum return loss and responsivity. The achieved return loss is 3 dB, and responsivity is around 5000 V/W, as shown in Figure 5.16 and Figure 5.17, respectively.

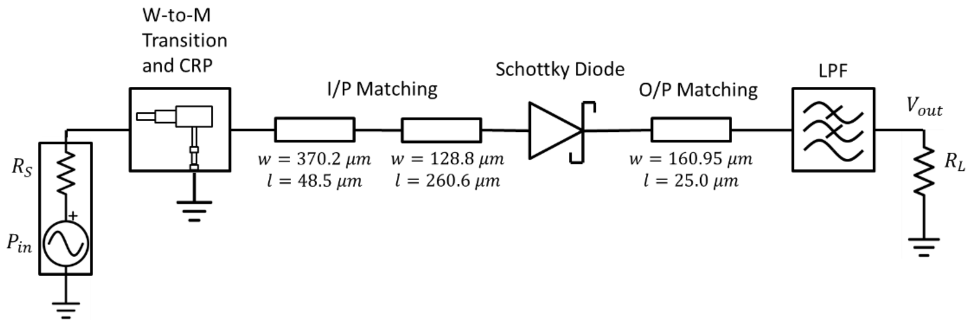

Figure 5.15 Schematic circuit including W-to-M transition and matching circuit.

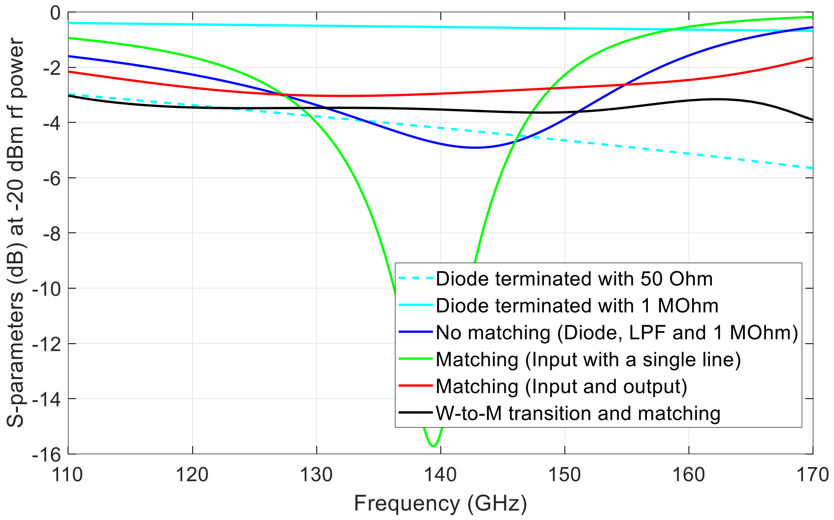

Figure 5.16 Reflection coefficient (S_{11}) at different design stages of the detector.

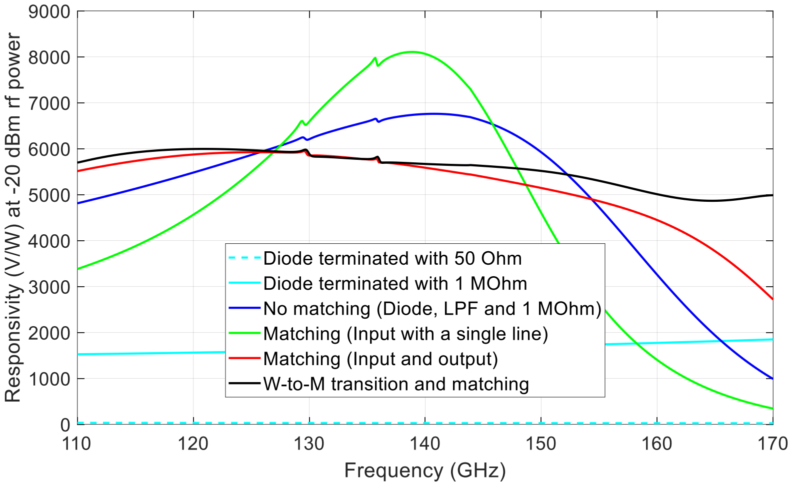

Figure 5.17 Responsivity (S_{11}) at different design stages of the detector.

As is seen from Figure 5.16 and Figure 5.17, the diode with a single matching line at the input gives narrow band matching and has a responsivity peak at around 139 GHz. However, achieving broadband match by adding matching lines at the input and output comes with the cost of reduced return loss to 2 dB (in red). As the return loss is reducing at higher frequencies, the responsivity (in red) is seen dropping drastically from around 5500 V/W at 140 GHz to 3000 V/W at 170 GHz. The detector with a waveguide to microstrip transition has a nearly flat return loss of 3 dB (in black) across the band. The corresponding least responsivity (in black) is around 5000 V/W. This final design (detector with the W-to-M transition) is the final structure to be implemented in the CST, as discussed in the following section.

5.5.2 Complete detector on microstrip

The individual circuit elements of the discrete detector are implemented on a single quartz substrate in CST, as shown in Figure 5.18. The structure has assigned three ports. Port 1 is at the waveguide input, and Port 2 is at the microstrip output. Port 3 is at the anode surface, the same as discussed in section 5.4. The S-parameters of the complete structure are exported to the SnP component in ADS, and the non-linear Spice model is connected at Port 3. The source resistance (R_S) is again set equal to the waveguide characteristic impedance 495 Ω (at 140 GHz). The load resistance (R_L) is 1 MΩ. It must be noted that CST might not simulate the 3D structure with significant differences in the largest dimension (such as the size of the complete detector) and the smallest dimension (such as the thickness of the microstrip line) in the same structure. In that case, alternatives such as Ansys HFSS (high-frequency structure simulator) can be used.

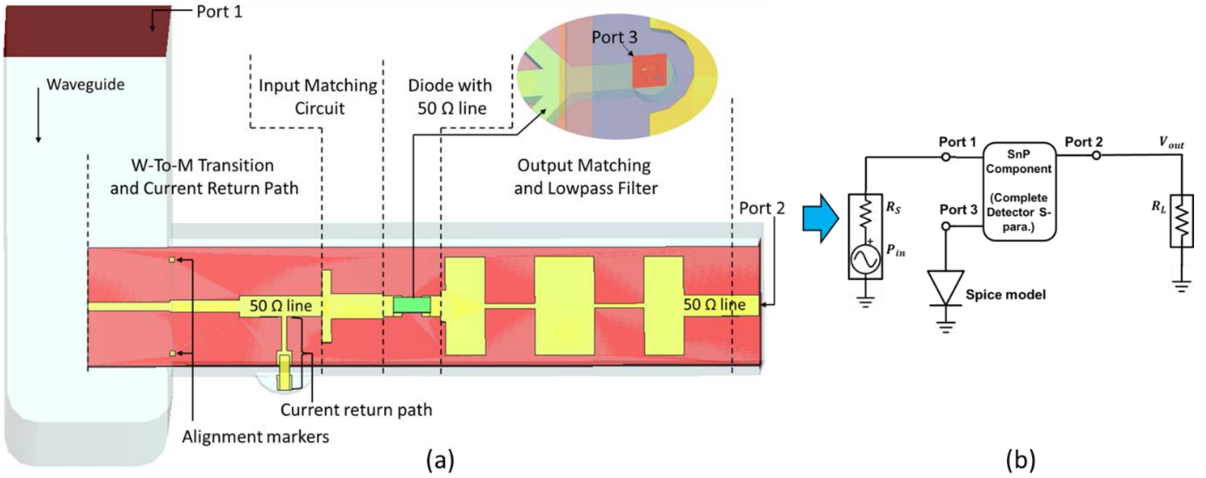

Figure 5.18 The complete detector (a) in CST microstrip structure, (b) in ADS SnP component for LSSP and Harmonic Balance simulation.

The LSSP (large signal scattering parameter) and HB (harmonic balance) simulations are performed in ADS. For LSSP simulation, the input power is swept from 0 dBm to -70 dBm in steps of -5 dBm and Parameter Sweep is used to simulate LSSP for each frequency point from 110 GHz to 170 GHz by a step of 5 GHz. For responsivity, Harmonic Balance simulation is performed by sweeping the power at each frequency point using a Parameter Sweep similar to LSSP.

LSSP is an s-parameter simulation of a relatively large input signal where the nonlinearity of the circuit must be taken into account. Hence, the s-parameter of the nonlinear system (e.g. diode and transistor) in large signal conditions is power-dependent, and the LSSP tool in ADS is used for this purpose [163].

HB is a frequency domain analysis used to simulate nonlinear devices. It assumes that the nonlinear systems have a steady-state solution that can be approximately represented by a finite Fourier series with satisfactory accuracy. The nonlinear response is sampled in the time domain and then transformed into the frequency domain using a finite Furior Transform. That means the simulator converts the nonlinear differential equations to algebraic ones, which are less complicated to solve using one of the numerical methods, such as Newton's method [163].

The simulated graph in Figure 5.19 shows that the reflection coefficient (S_{11}) and responsivity depend on input RF power. The S_{11} gets better for high power but worsens for low power, which is the opposite in the case of responsivity. This is due to the increased dominance of diode series resistance on diode current at higher power, which makes the junction resistance saturated with a value equal to series resistance [88]. The responsivity is better for low power levels and reduced for high powers. At higher power (above ~ -25 dBm), the diode enters from the square law region to the linear region, where the output voltage is no longer proportional to the square of the input voltage; instead, the input voltage only, so the responsivity drops.

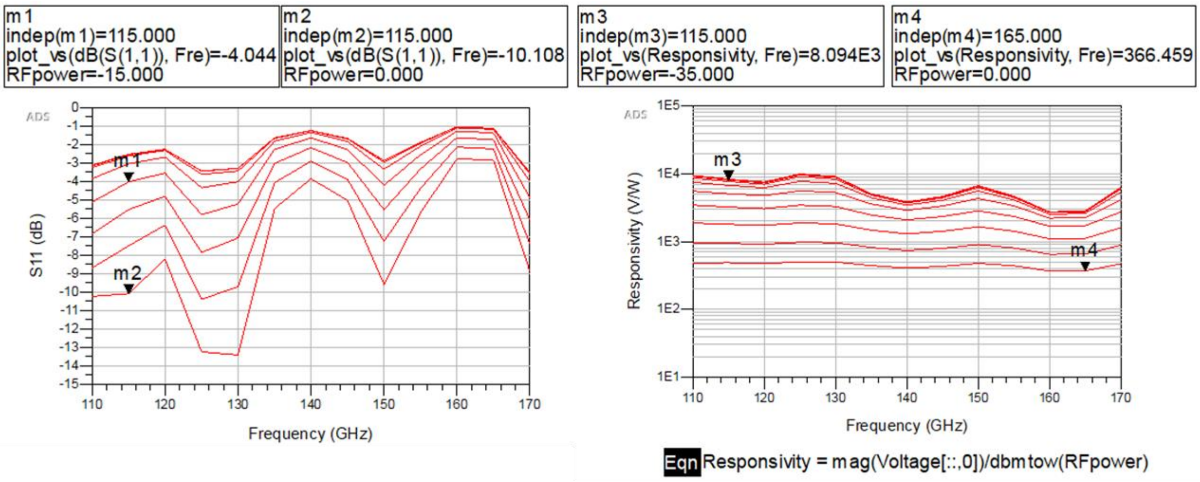

(a) (b)

Figure 5.19 Simulated (a) reflection coefficient (S_{11}) at various RF power levels, (b) responsivity with respect to frequency.

The responsivity and the detected voltage are plotted in Figure 5.20 with respect to input power. It is seen that the responsivity reduces drastically as the power increases above -30 dBm but stays well above 2000 V/W until -20 dBm. As shown in Figure 5.20 (b), the slope of voltage versus power changes as the diode moves from the square law region to the linear region for power more than around -25 dBm.

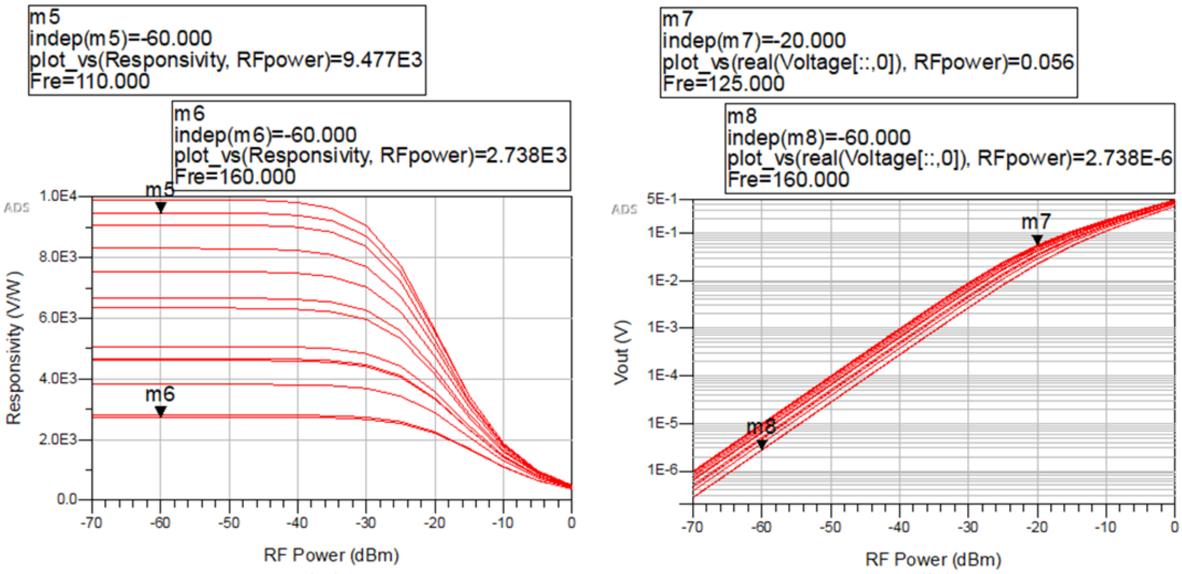

(a) (b)

Figure 5.20 Simulated (a) responsivity versus input RF power, (b) DC voltage versus input RF power.

5.6 Design of Detector Packaging

The layout of the detector chip with all the dimensions is detailed in Figure 5.21. The size of the chip is 50 µm × 600 µm × 3380 µm (thickness × width × length). As discussed in Section 5.1.2, it consists of a W-to-M transition with a current return path, input matching, diode output matching and lowpass filter. The largest feature on the chip is the low impedance line of LPF with a width of 500 µm. The smallest feature on the chip is the markers, high impedance lines of filter and current return path with a line width of 25 µm.

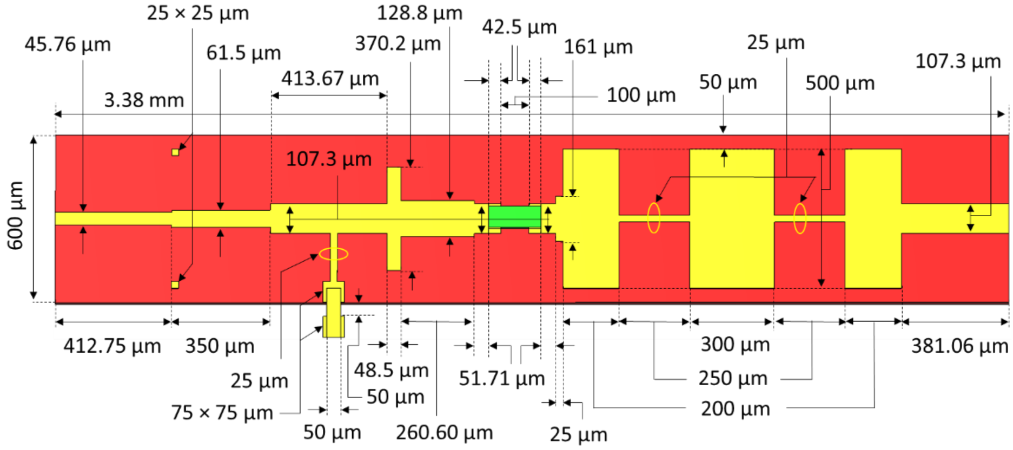

Figure 5.21 The 50 µm thick detector chip layout with all the dimensions.

The detector body with the UG-387 flange is developed in two blocks, split in the E-plane of the waveguide, as shown in Figure 5.22. The chip is in the left block, and the SMA (subminiature version A) connector is at the back. The structure would contain delicate parts such as the diode and bond wires, so the assembled system must be robust. The screw holes are added not just on the body but also on the flange to make the hold strong.

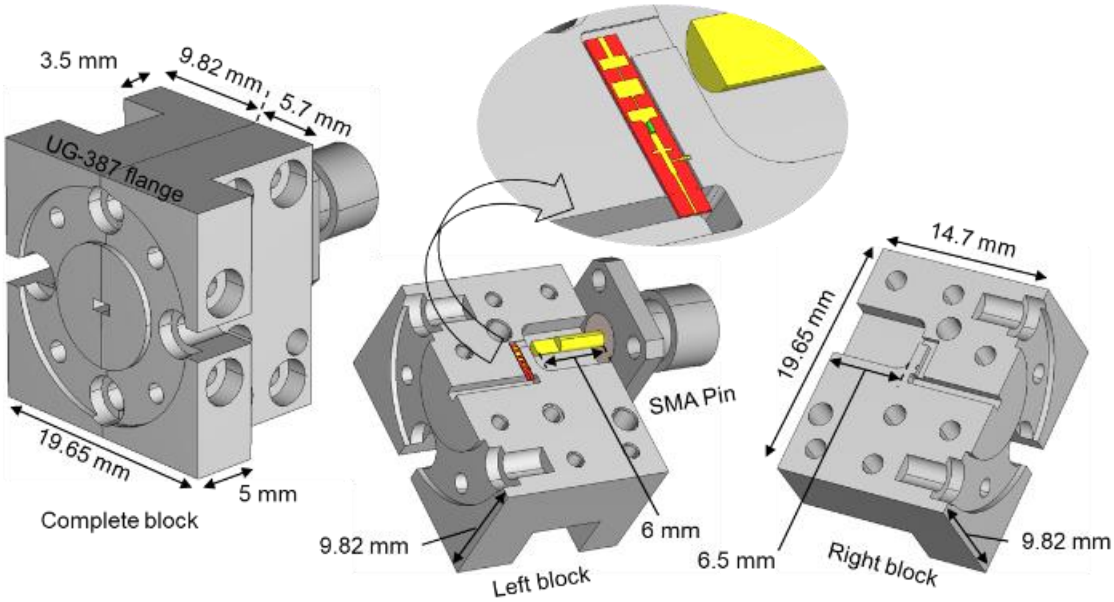

Figure 5.22 The detector body with embedded UG-387 flange and SMA connector at the back designed in CST.

The housing is designed to accommodate the arched bond wires and clearance gap for a relatively large centre conductor of the SMA connector. The dimensions of channels or cavities in the metal blocks are detailed in Figure 5.23 and Figure 5.24. The SMA pin has a centre conductor diameter of 1.27 mm, and the minimum gap between the centre pin and the metal housing is 500 µm at the front cross-section of the pin. On the side of the SMA pin, the gap is 865 µm. The recess width for the detector chip is 700 µm, and the central recess width between the sensor chip and the SMA pin is 600 µm. The height of both recesses is 550 µm, of which 50 µm is in the left block to fit the detector chip, and the remaining 500 µm is in the right block. The corners of the recesses and the waveguide are rounded by a radius of 150 µm, and the corner of the SMA channel by 1 mm. Figure 5.24 shows the back view of the housing with an arrangement for mounting the SMA pin. It shows that the SMA channel is split in half, with a 1.5 mm top and bottom, and the central recess for bond wiring is also visible.

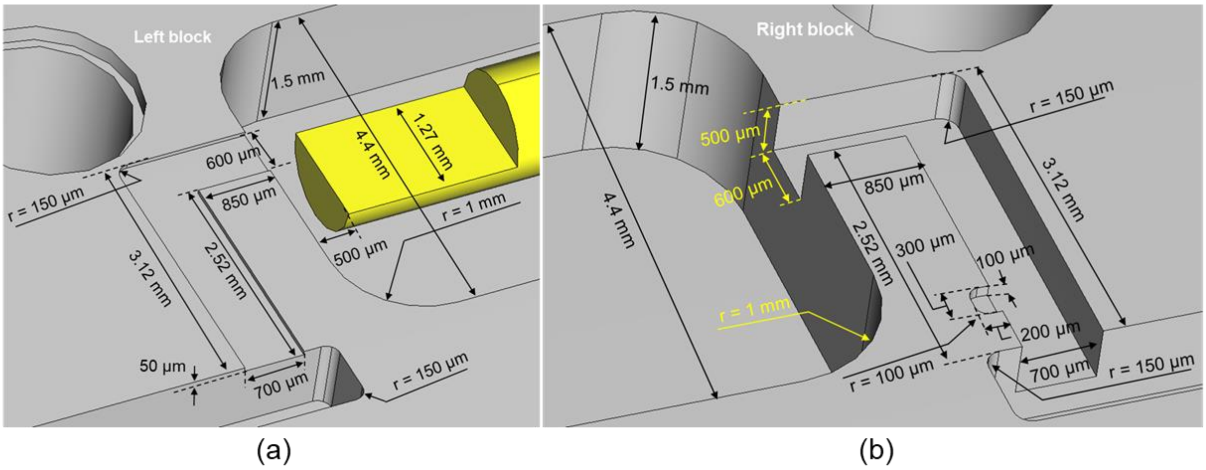

Figure 5.23 Channels in (a) left block, (b) right block of the detector body and their dimensions.

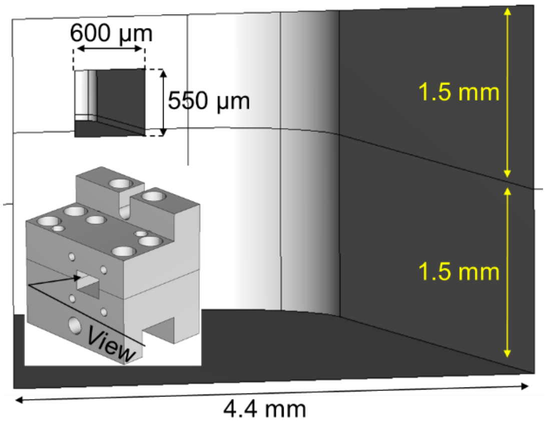

Figure 5.24 The view from the channel in the back of the detector body for the SMA centre conductor.

5.7 Fabrication and Assembly

The detector split blocks are CNC machined in aluminium and plated with gold, as shown in Figure 5.25. The quartz substrate with a microstrip feature is installed into the recess using non-conducting glue (manufacturer confidential), and the diode leads are wedge-bonded. The bond wires are used to short the current return path to the metal body (ground) and bond the microstrip output to the SMA connector.

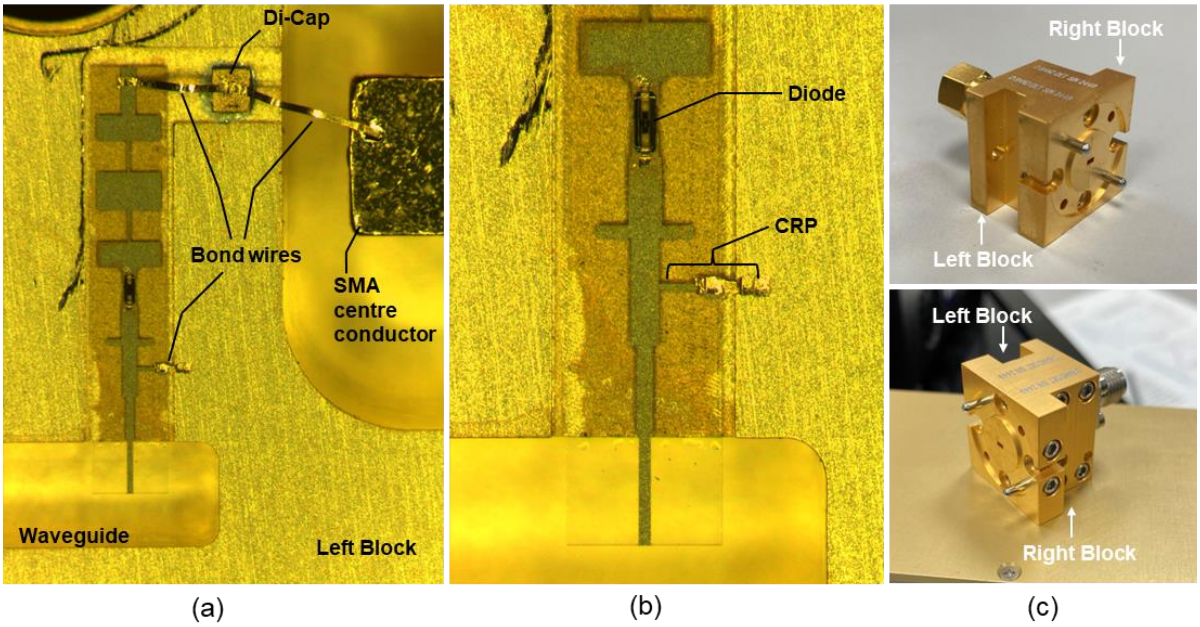

Figure 5.25 Fabricated (a) detector chip installed in the recess/channel, (b) detector chip zoomed version, (c) detector assembled and its view from two different perspectives.

The dielectric capacitor (Di-Cap) is used to step down the long bond wire, which avoids possible short circuits to the narrow channel and simultaneously acts as a lowpass filter. Also, this secures the bonding contact at the microstrip output. The Di-Cap (part number: D12BV101K5PX 100 pF) has dimensions 102 µm × 305 µm × 381 µm (thickness × width × length) [164] and fits into the central channel between the detector chip and SMA pin.

5.8 Measurement and Discussion

The reflection coefficient measurements are performed at NPL, London. The diode power detector (device under test or DUT) was connected to Port 1 after the vector network analyser (VNA) calibration using D-band calibration standards to measure the reflection coefficient (S_{11}), and the PM5 power meter combination was connected to Port 2 to note the power, as shown in Figure 5.26. The VNA frequency extender module (VNAX) allows the measurements at D-band. The signal power of the VNA is varied, and it appears approximately the same at both ports 1 and 2. Also, a change in the signal frequency changes the power at the ports. Therefore, the power was maintained at -20 dBm at different frequency points by adjusting the power setting in the VNA, and corresponding reflection coefficients are noted.

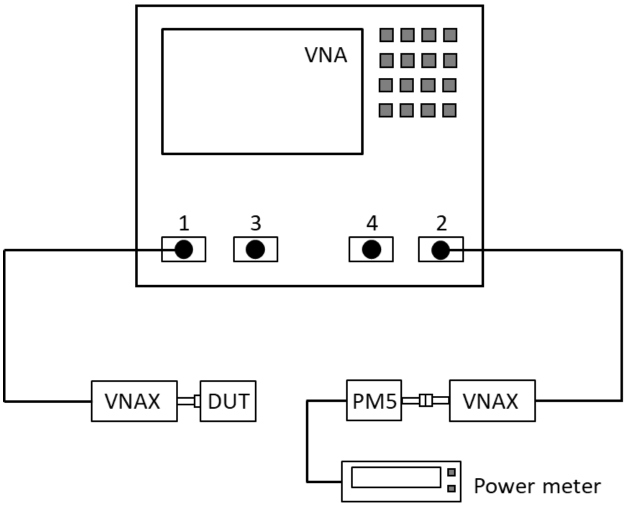

Figure 5.26 Reflection coefficient measurement setup.

The simulated and measured reflection coefficients are compared in Figure 5.27. The measured return loss is better than 2.5 dB, whereas the simulated return loss is better than 1 dB. These S_{11} responses are typical for Schottky devices and are challenging to improve further. This is due to the complex RF equivalent circuit of the diode, which has parasitic elements which depend on frequency. Diode intrinsic elements such as junction capacitor's reactance change with frequency, making it difficult to match over a wider bandwidth. The trend of both graphs is the same, showing better matches at lower frequencies, especially for the measured response.

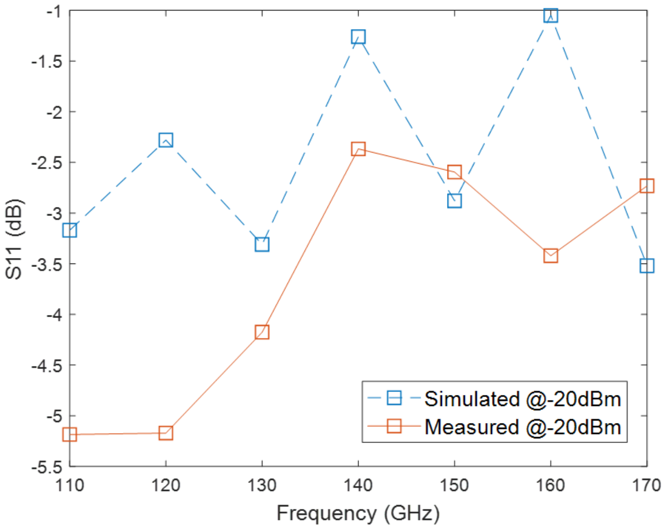

Figure 5.27 Reflection coefficient measured and simulated at -20 dBm.

The power measurement for responsivity was performed by Teratech Components Ltd. with their dedicated measurement setup, which is confidential. The measured and simulated responsivity at two power levels (-20 and -25 dBm) are plotted in Figure 5.28. The minimum responsivity in all cases is nearly 2000 V/W. The trend of measured and simulated responsivity is in agreement. However, the effect of matching can be clearly seen. The responsivity is better at lower frequencies, and the average responsivity is nearly 5000 V/W. The variation in measured responsivity (1900-10500 V/W) is more than the simulated (2200-5200 V/W) at -20 dBm input power. This can be attributed to fabrication uncertainty, and process variation can be a part of further study.

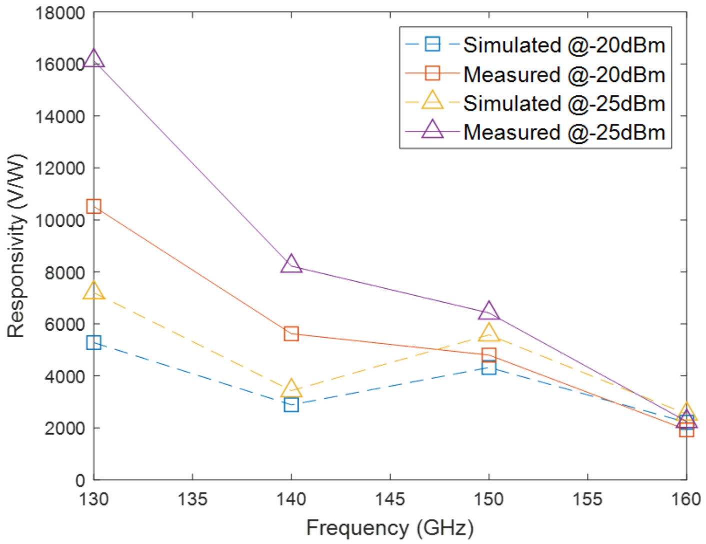

Figure 5.28 Responsivity measured and simulated at -20 dBm and -25 dBm.

5.9 Summary

The Schottky diode is a majority charge carrier device, and the diode with low capacitance can make it suitable to work up to a few terahertz frequency bands. The square law characteristic of the Schottky diode is used for power detection. The manufacturer provides the 3D and Spice models for design, which is more convenient than using equivalent circuits at higher frequencies. The matching circuit is important in delivering the maximum input power to the diode junction. The detector chip was built on a 50 µm thick quartz substrate with microstrip features in gold and a diode mounted in the 100 µm gap. The detector body is a split block of aluminium plated with gold. The wideband matching is challenging, with an achieved return loss of only 2.5 dB from measurement, which is typical for such devices. The least achieved responsivity is 1900 V/W at 160 GHz from the measurements, and the difference between the maximum (10500 V/W at -20 dBm) and minimum (1900 V/W at -20 dBm) responsivity is 8600 V/W which is typical and shall be reduced in future work. The comparison with other Schottky diode power detectors using diode use, working frequency and responsivity is given in Table 2.2. Compared to the detectors working in the D-band in Table 2.2, the responsivity of the designed detector is higher at lower frequencies; however, the difference between maximum and minimum responsivity is large.

CHAPTER 6

CONCLUSION AND FUTURE WORK

6.1 Conclusion

6.1.1 Bolometric power detector

The bolometric power detector is designed with thin film mounted in the E-plane of the waveguide. The thin film in the waveguide gives a resonance match where the bandwidth is narrow and depends on the film width and sheet resistance. The higher sheet resistance improves return loss but reduces the film thickness. The solution of a thin film in a waveguide can be applied to both types of arrangement, one facing the input port and the other facing the narrow wall. The thin film facing the narrow wall of the waveguide is preferred for the bolometer design to add more than one film on the same substrate to improve bandwidth. However, the direct solution is not available like single film design. The double-line design is based on knowledge gained from single-line design and computer simulation/optimisation. It is proved that double-line design improves bandwidth more than single-line, and its structure can be validated using equivalent circuits. The materials for the thin film must have a high temperature coefficient of resistance for sensing the heat rise and high resistivity to get a larger film thickness for fabrication ease. Titanium is the most suitable and chosen for thin film.

The basic double-line design evolved in five stages while analysing the reflection coefficient (S_{11}). The DC readout arrangement and the thermal insulation are the primary considerations in realising the bolometer. The rectangular shape is chosen over the T-shape for ease of fabrication. The substrate width plays a crucial role in defining the final design's reflection coefficient (S_{11}). Increasing the gaps around the sensor chip shifts the S_{11} towards the lower frequency, compensated by increasing film width, which does the opposite. The final design achieves a reflection coefficient of -15 dB from 120 – 170 GHz. The dual sensor design is introduced, consisting of sensor A and sensor B; the latter compensates for the ambient temperature variation from sensor A. The double shielding layer is designed for better thermal insulation and ease of handling. To improve thermal insulation (heat leak in either direction), low thermal conductivity materials are used for the sensor chip (quartz), sensor wrapping (polyimide), sensor body and inner shielding layer (PEEK). Only sensor A's body is gold plated as it carries RF power. The outer layer is made of aluminium. The shieldings also help for ease of handling.

The power detector is characterised, and a comparison is drawn between the designed power detector and the commercial power detector, VDI-Erickson PM5. The characterisation involves reflection coefficient measurement, short-term and long-term time response, frequency response and linearity measurement. The measured reflection coefficient agrees with the simulated; however, the measured return loss is reduced to 11.5 dB over 120-170 GHz, and it is 4.2 dB at 110 GHz. Statistical concepts such as deviation, average, and standard deviation are applied to the measurement data, allowing direct performance comparison between the designed and commercial sensors. The designed sensor has shown highly competitive performance. The standard deviation in the short-term response of the commercial sensor is 0.27 %, whereas the designed sensor is nearly the same, 0.19 %. The response time of the commercial sensor is 0.2 s with feedback; otherwise, the time constant of its basic sensor is 6 s, whereas the designed sensor has a 90 % response time of less than 2.6 s. The time resolution of 2.6 s is limited by delays from Ohm-meters, computers, and cables called the measurement system response time. The deviation in long-term time measurement for commercial and designed sensors is nearly the same and less than 0.6 %. This indicated that all the thermal insulation measures have been highly effective apart from the structural benefit of a thin film in a waveguide, which differs from the calorimetric sensor based on the absorption principle. The frequency response of the designed detector is measured for time intervals ranging from 1 min up to 120 min. It has shown a very good reproducible frequency response with a one-sigma standard deviation of 0.66 % at 135 GHz and a minimum of 0.33 % at 115 GHz. The detector is linear with less than 0.25 % deviation (from the arbitrarily chosen reference point of 5 dBm) for power above -3 dBm.

To the author's knowledge, this is the only power detector above 100 GHz that is based on resonance type matching, filling the research gap of more than three decades since the last reported type in 1985, but at 94 GHz [87] and also showing competitive performance with commercial potential as a transfer/working standard.

6.1.2 Schottky diode power detector

The diode power detector is designed for D-band waveguide-based applications. Schottky diode is a non-linear device that gives output voltage proportional to the square of input voltage, equivalent to input power. The diode power detector basic blocks contain W-to-M transition, input matching, diode, output matching, LPF and load resistance. The power detector's individual (discrete) structures are first implemented in CST for 3D EM (Electromagnetic) simulations and then exported to ADS for non-linear circuit simulation. The LPF and W-to-M transition with the return path defines the substrate width and channel dimensions, respectively. LPF has simulated return loss of more than 20 dB in the D-band. The transition's simulated insertion loss (S_{12}) is 0.26 dB, and the return loss is more than 15 dB. The equivalent circuit contains parasitic elements and becomes dominant as the diode's dimension becomes comparable to the operating wavelength, increasing the matching difficulty over a wider bandwidth. The combination of the diode 3D model and Spice model makes it easier to predict diode embedding impedances than the equivalent circuit to design the matching circuit. The single line matching at the input provides a limited bandwidth of 6 GHz (10 %) for 10 dB return loss and peak responsivity of 8000 V/W centred around 140 GHz. The expected wideband matching (ideally flat response) is challenging to obtain with a return loss of more than 10 dB. The bandwidth is increased at the expense of a low return loss of 3 dB, hence the reduced responsivity to 5000 V/W, by adding two matching lines at the input and one at the diode output. The LSSP and HB simulation is further used to analyse the complete detector's response (S_{11} and responsivity) at different power levels. The reflection coefficient of the diode detector reduces for higher power and increases and eventually saturates for lower power. The responsivity does the opposite; it stays higher for lower power levels and reduces as power increases.

The detector body is fabricated into aluminium split blocks plated with gold. The detector chip is fabricated using a 50 µm thick quartz substrate and the gold microstrip features. The gold microstrip features are developed on the 50 µm quartz substrate. The measured reflection coefficient is better than -2.5 dB at -20 dBm input power and has a trend similar to the simulated; S_{11} gets better for lower frequencies. The measured average responsivity at -20 dBm input power is approximately 5000 V/W; the lowest is 2000 V/W at 160 GHz. The responsivity trend has shown its dependence on matching. The variation in responsivity (highest - lowest) is more in the measured (1900 - 10500 V/W) than the simulated (2200 - 5200 V/W) at -20 dBm input power. These results are typical for diode detectors and challenging to improve.

6.2 Future Work

6.2.1 Bolometric power detector

In future, the bolometric power detector can be approached either way: (1) matched load type matching and (2) resonance type matching. The first approach presented in this thesis has shown that matching is challenging; however, it has the benefit of faster response time. The direct analytical solution for wideband matching the waveguide shorted at one end can still be explored. The double line design presented in the thesis can be scaled up and down the D-band. The scaled-up version of the double line design in the G-band (140 – 220 GHz) is shown in Figure 6.1 (a). Although the T-shape was not considered for the design presented in Chapter 4 due to fabrication and handling challenges, the scaled-up version can adopt the shape by splitting it into two separate rectangular substrates, one for the sensor chip and the other for the large pads (Pad 1 and Pad 2). The bond wiring concept from Chapter 5 can be utilised for making electrical connections between the two chips. The simulated S_{11} in Figure 6.1 (b) has shown the scaled-up design in G-band covers 87.5 % of -12 dB bandwidth, similar to the simulated double line design in the D-band (Chapter 4). The S_{11} response could be further improved. The final design that could be fabricated is shown in Figure 6.1 (c).

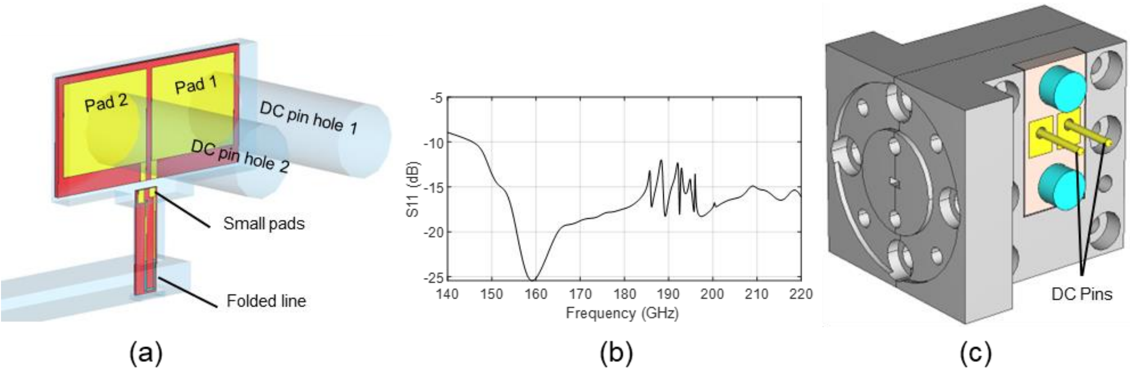

Figure 6.1 Scaled-up resonance match design (a) air model, (b) simulated reflection coefficient, (c) detector housing.

The second approach is a matched-load-based design where wideband matching is straightforward, and the shape or size of the sensor around the absorber does not affect matching significantly; however, the thermal insulation of the sensor chip is challenging, as discussed in Section 2.2. The measures to reduce the system's thermal mass must be taken for future designs. The sensor chip in [24] can be made smaller to reduce the thermal mass, and the multiple meader line concept from [25] can be adopted on the same chip to investigate optimum performance, as shown in Figure 6.2 (a). Two sets of meander lines are on the sensor chip, each with three pads on one side of the chip. The pads A1, A2 and A3 are on one meander line, and B1, B2, and B3 are on the other. One of the meander lines can be made of platinum as a sensor, and the other from NiCr to function as a heater for calibration purposes. The simulated reflection coefficient of the design is shown in Figure 6.2 (b), which depends on the taper angle. The thin wall waveguide [11] can be implemented by modifying the housing, as shown in Figure 6.2 (c), to further reduce the thermal mass. The thin tapered waveguide can be placed in the metal housing with a plastic holder for thermal insulation. The DC connection arrangement can be made at the back of metallic shielding, and The bond wiring concept can be used again. The waveguide tapered section in Figure 6.2 (d) is being considered for this design. The housing and sensor chip will be fabricated, and measurements will be carried out.

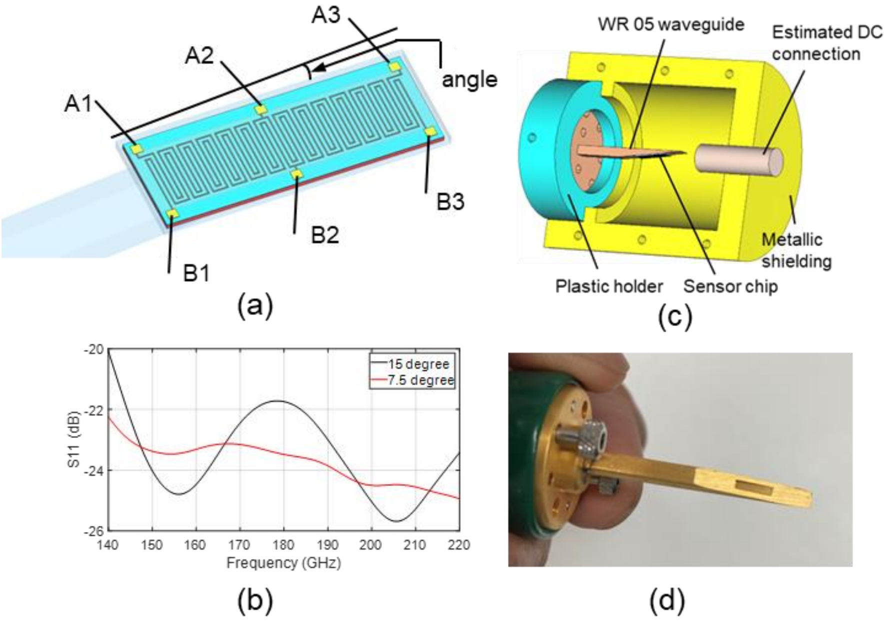

Figure 6.2 Scaled-up matched load design (a) air model, (b) simulated reflection coefficient, (c) detector housing, (d) commercial tapered waveguide.

6.2.2 Schottky diode power detector

The diode detector chip can be split into two, as discussed in Section 6.2.1, but connected by bonding metal strip or beam lead to maintain high-frequency performance. The first part of the chip would be a W-to-M transition with a return path, and the second part could be made wider, giving more space and flexibility to design matching circuits to achieve wider bandwidth. The difference in maximum and minimum responsivity should be reduced by investigating and optimising the detector circuit. The manufacturing process variation in a Schottky diode detector can also be an essential part of further study.

References

[1] Agilent Technologies Application Note 1449-1, “Fundamentals of RF and Microwave Power Measurements (Part 1),” no. Part 1, pp. 1–32, 2003.

[2] C. G. Montgomery, *Technique of Microwave Measurements*, First. McGraw-Hill Book Company, Inc, 1947.

[3] Rohde & Schwarz, “Voltage and Power Measurements 60 Years of Competence in Voltage and Power Measurements,” 2011.

[4] X. Cui, Y. S. Meng, Y. Shan, and Y. Li, “Microwave Power Measurements: Standards and Transfer Techniques,” *New Trends Dev. Metrol.*, pp. 3–20, 2016.

[5] S. Jenabi, A. Malekabadi, D. Deslandes, F. Boone, and S. A. Charlebois, “Submillimeter wave GaAs Schottky diode application based study and optimization for 0.1–1.5 THz,” *Solid. State. Electron.*, vol. 134, pp. 65–73, 2017.

[6] P. H. Siegel, “Terahertz Technology,” *IEEE Trans. Microw. Theory Tech.*, vol. 50, no. 3, pp. 910–928, 2002.

[7] G. Chattopadhyay, “Sensor Technology At Submillimeter Wavelengths for Space Applications,” *Int. J. Smart Sens. Intell. Syst. March 2008*, vol. 1, no. 1, pp. 1–20, 2008.

[8] T. S. Rappaport *et al.*, “Wireless communications and applications above 100 GHz: Opportunities and challenges for 6g and beyond,” *IEEE Access*, vol. 7, pp. 78729–78757, 2019.

[9] X. Shang, M. Ke, Y. Wang, and M. J. Lancaster, “WR-3 band waveguides and filters fabricated using SU8 photoresist micromachining technology,” *IEEE Trans. Terahertz Sci. Technol.*, vol. 2, no. 6, pp. 629–637, 2012.

[10] Virginia Diodes Inc, “PM5 Operational Manual,” vol. 6172, Charlottesville, VA, USA, p. 22, 2016.

[11] N. Erickson, “A Fast and Sensitive Submillimeter Waveguide Power Meter,” *Tenth International Symposium on Space Terahertz Technology*. pp. 501–507, 1999.

[12] X. Chen, M. Salek, Q. Zhang, and Y. Wang, “Subterahertz Filtering Six-Port Junction,” *IEEE Trans. Microw. Theory Tech.*, vol. 70, no. 8, pp. 3877–3885, 2022.

[13] J. W. Allen, F. R. Clague, N. T. Larsen, and M. P. Weidman, “NIST Microwave Power Standards in Waveguide,” *NIST Tech. Note 1511*.

[14] R. Judaschke, “Traceability of RF measurement quantities to national standards.”

[15] W. Yuan, X. Cui, Y. Li, and Y. S. Meng, “Development of a WR-6 Waveguide Microcalorimeter for Thermoelectric Power Sensor,” *CPEM 2018 - Conf. Precis. Electromagn. Meas.*, pp. 1–2, 2018.

[16] R. H. Judaschke, K. Kuhlmann, T. Reichel, and W. Perndl, “A w-band thermoelectric power transfer standard,” *CPEM Dig. (Conference Precis. Electromagn. Meas.*, pp. 756–757, 2014.

[17] X. Cui, Y. Li, X. Gao, M. Dai, and D. Zhu, “Measurement and Evaluation of the WR-28 Calorimeter,” *2011 77th ARFTG Microw. Meas. Conf. Des. Meas. Microw. Syst. ARFTG 2011*, pp. 1–3, 2011.

[18] X. Cui, Y. S. Meng, Y. Li, Y. Zhang, and Y. Shan, “An Improved Design and Simplified Evaluation Technique for Waveguide Microcalorimeter,” *IEEE Trans. Instrum. Meas.*, vol. 65,

no. 6, pp. 1450–1455, 2016.

[19] Y. S. Lau, T. Denning, and C. Oleson, “Millimeter wave power measurement above 110 GHz,” *2006 67th ARFTG Microw. Meas. Conf. - Meas. Des. High Power Devices Syst.*, pp. 97–102, 2006.

[20] R. H. Judaschke, K. Kuhlmann, T. M. Reichel, and W. Perndl, “Millimeter-Wave Thermoelectric Power Transfer Standard,” *IEEE Trans. Instrum. Meas.*, vol. 64, no. 12, pp. 3444–3450, 2015.

[21] Hughes Aircraft Company, “MILLIMETER-WAVE TEMPERATURE COMPENSATED THERMISTOR MOUNT,” *Tech. Man.*

[22] R. H. Judaschke, W. Perndl, K. Kuhlmann, and J. Ruhaak, “Thermoelectric power transfer standards for V-and W-band,” *CPEM 2016 - Conf. Precis. Electromagn. Meas. Conf. Dig.*, pp. 2–3, 2016.

[23] J. Y. Kwon, Y. P. Hong, D. J. Lee, and T. W. Kang, “V- and W-band waveguide microcalorimeters for millimeter-wave power standards,” *85th ARFTG Microw. Meas. Conf. Meas. Tech. 5G Appl. ARFTG 2015*, pp. 1–3, 2015.

[24] M. Salek *et al.*, “Design, Fabrication, and Characterization of a D-Band Bolometric Power Sensor,” *IEEE Trans. Instrum. Meas.*, vol. 71, pp. 6–14, 2022.

[25] X. Wang, Q. Zhong, J. Li, W. Yuan, Y. Li, and X. Cui, “WR-06 Power Standard Devices,” *CPEM 2018 - Conf. Precis. Electromagn. Meas.*, pp. 1–2, 2018.

[26] J. Y. Kwon, Y. P. Hong, and N. W. Kang, “D-Band Waveguide Microcalorimeter for Millimeter-Wave Power Standard,” *CPEM 2018 - Conf. Precis. Electromagn. Meas.*, pp. 1–2, 2018.

[27] W. He, W. Zhang, W. Qi, and H. Yin, “Design of a 110GHz to 170GHz calorimeter,” *2017 Int. Work. Electromagn. Appl. Student Innov. Compet. iWEM 2017*, no. 1, pp. 71–73, 2017.

[28] K. Shimaoka, M. Kinoshita, K. Fujii, and T. Tosaka, “Design of a broadband calorimeter for mm-wave power standard in the frequency range from 110 GHz to 170 GHz,” *Int. Conf. Infrared, Millimeter, Terahertz Waves, IRMMW-THz*, pp. 1–2, 2012.

[29] Y. Tojima, M. Kinoshita, H. Iida, and K. Fujii, “Development of WR-5 Waveguide Calorimeter for Millimeter Wave Power Standard,” *CPEM 2018 - Conf. Precis. Electromagn. Meas.*, pp. 1–2, 2018.

[30] C. Ma, X. Cui, W. Yuan, and Y. Li, “Design of a WR-6 thermoelectric conversion power sensor,” *IRMMW-THz 2015 - 40th Int. Conf. Infrared, Millimeter, Terahertz Waves*, vol. 6, pp. 1–2, 2015.

[31] D. Adamson, J. Miall, J. Howes, M. Harper, and R. Thompson, “A new 75-110 GHz primary power standard with reduced thermal mass,” *75th ARFTG Microw. Meas. Conf. Meas. Modul. Signals Commun.*, pp. 1–4, 2010.

[32] X. Cui, W. Yuan, Y. Li, C. Jia, and Y. S. Meng, “Development of a National WR-10 (75 to 110 GHz) Microcalorimeter,” *2016 URSI Asia-Pacific Radio Sci. Conf. URSI AP-RASC 2016*, pp. 478–480, 2016.

[33] D. Gu, X. Lu, B. F. Jamroz, D. F. Williams, X. Cui, and A. W. Sanders, “NIST-Traceable Microwave Power Measurement in a Waveguide Calorimeter with Correlated Uncertainties,” *IEEE Trans. Instrum. Meas.*, vol. 68, no. 6, pp. 2280–2287, 2019.

[34] Y. Huang, W. Yuan, X. Cui, Y. S. Meng, and Y. Li, “WR-42 Waveguide Microcalorimeter for Thermistor Mount Calibration,” *CPEM 2018 - Conf. Precis. Electromagn. Meas.*, pp. 1–2, 2018.

[35] J. A. Mallat, S. N. Dudorov, D. V. Lioubtchenko, and A. V. Räisänen, “110-170 GHz millimetre

wave power standard," *Proc. 36th Eur. Microw. Conf. EuMC 2006*, no. September, pp. 482–485, 2006.

[36] C. M. O'Sullivan and J. A. Murphy, "Schottky Diodes," *F. Guid. to Terahertz Sources, Detect. Opt.*, no. February, pp. 35–36, 2012.

[37] H. Ko *et al.*, "Zero-bias InGaAs Schottky barrier diode array for terahertz imaging applications," *2014 Optoelectron. Commun. Conf. OECC 2014 Aust. Conf. Opt. Fibre Technol. ACOFT 2014*, no. July, pp. 982–983, 2014.

[38] X. Yang and P. Chahal, "Embedded actives for terahertz circuit applications: Imaging array," *Proc. - Electron. Components Technol. Conf.*, pp. 2082–2086, 2012.

[39] H. Liu, J. Yu, P. Huggard, and B. Alderman, "A multichannel THz detector using integrated bow-tie antennas," *Int. J. Antennas Propag.*, vol. 2013, 2013.

[40] D. Guo *et al.*, "A 2×2 integrated heterodyne receiver array for terahertz imaging application," *9th Int. Conf. Microw. Millim. Wave Technol. ICMMT 2016 - Proc.*, vol. 2, pp. 795–797, 2016.

[41] J. C. Mou, M. M. Xu, L. Chen, Z. M. Wang, W. H. Yu, and X. Lv, "Schottky diodes with the cutoff frequency of 2.6 THz and its applications in focal imaging array," *2012 Int. Conf. Microw. Millim. Wave Technol. ICMMT 2012 - Proc.*, vol. 2, pp. 807–810, 2012.

[42] K. B. Cooper *et al.*, "Penetrating 3-D imaging at 4- and 25-m range using a submillimeter-wave radar," *IEEE Trans. Microw. Theory Tech.*, vol. 56, no. 12, pp. 2771–2778, 2008.

[43] M. Hoefle *et al.*, "89 GHz zero-bias Schottky detector for direct detection radiometry in European satellite programme MetOp-SG," *Electron. Lett.*, vol. 50, no. 8, pp. 606–608, 2014.

[44] J. H. Schaffner *et al.*, "A wideband radiometer module for an unamplified direct detection scalable W-band imaging array," *Passiv. Millimeter-Wave Imaging Technol. XI*, vol. 6948, no. May, p. 694807, 2008.

[45] F. Yang, Z. Wang, W. Dou, and Z. Sun, "ZERO-BIASED DIODE SCHOTTKY DETECTOR FOR LOW COST PREAMPLIFIED MILLIMETER-WAVE IMAGING," *Microw. Opt. Technol. Lett.*

[46] L. Xie, Y. H. Zhang, and Y. Fan, "W-band radiometer front end module for real-time imaging," *Microw. J.*, vol. 57, no. 1, pp. 80–90, 2014.

[47] D. Segovia-Vargas *et al.*, "300 GHz CMOS video detection using broadband and active planar antennas," *2013 7th Eur. Conf. Antennas Propagation, EuCAP 2013*, no. Eucap, pp. 744–747, 2013.

[48] H. Sherry *et al.*, "Lens-integrated THz imaging arrays in 65nm CMOS technologies," *Dig. Pap. - IEEE Radio Freq. Integr. Circuits Symp.*, pp. 6–9, 2011.

[49] A. Tomkins, P. Garcia, and S. P. Voinigescu, "A passive W-band imager in 65nm bulk CMOS," *Tech. Dig. - IEEE Compd. Semicond. Integr. Circuit Symp. CSIC*, pp. 1–4, 2009.

[50] C. Y. Huang, C. M. Li, L. Y. Chang, C. C. Nien, Y. C. Yu, and J. H. Tarng, "A W-band monolithic HEMT receiver for passive millimeter-wave imaging system," *Asia-Pacific Microw. Conf. Proceedings, APMC*, vol. 2, pp. 367–370, 2011.

[51] L. Gilreath, V. Jain, and P. Heydari, "Design and analysis of a w-band sige direct-detection-based passive imaging receivera," *IEEE J. Solid-State Circuits*, vol. 46, no. 10, pp. 2240–2252, 2011.

[52] N. Daghestani *et al.*, "Room temperature ultrafast InGaAs Schottky diode based detectors for

terahertz spectroscopy," *Infrared Phys. Technol.*, vol. 99, no. December 2018, pp. 240–247, 2019.

[53] Y. Tian, J. Jiang, Q. Liu, C. Lin, K. Huang, and X. Deng, "A 15Gps high speed OOK receiver based on a 0.34THz Zero-bias Schottky diode detector," *27th Int. Symp. Sp. Terahertz Technol. ISSTT 2016*, vol. 2, pp. 8–10, 2017.

[54] H. Zirath and Z. He, "Power detectors and envelope detectors in mHEMT MMIC-technology for millimeterwave applications," *Eur. Microw. Week 2010 Connect. World, EuMIC 2010 - Conf. Proc.*, no. September, pp. 353–356, 2010.

[55] "Mm-Wave High Sensitive Power Meters," *ELVA-1 Man.*, pp. 1–2.

[56] J. Guo, H. Cheng, J. Xu, and C. Qian, "Design of a full W-band detector based on Schottky diode with quartz substrate," *IET Microwaves, Antennas Propag.*, vol. 13, no. 7, pp. 936–941, 2019.

[57] D. F. Ji, B. Niu, H. Q. Tao, T. S. Chen, and W. B. Wang, "A D Band Zero Bias Detector Chip Using Schottky Diode," *Prog. Electromagn. Res. Symp.*, vol. 2022-April, pp. 752–754, 2022.

[58] M. Hrobak, M. Sterns, M. Schramm, W. Stein, and L.-P. Schmidt, *Planar Zero Bias Schottky Diode Detector Operating in the E- and W-Band*. 2013.

[59] C. Hannachi, B. Zouggari, R. I. Cojocaru, T. Djerafi, and S. O. Tatu, "A V-band high dynamic range planar integrated power detector: Design and characterization process," *Microw. Opt. Technol. Lett.*, vol. 59, no. 11, pp. 2742–2748, 2017.

[60] F. Michler, S. Lindner, F. Lurz, S. Erhardt, R. Weigel, and A. Koelpin, "Zero-bias schottky power detector design for six-port based radar systems," *Eur. Microw. Week 2017 "A Prime Year a Prime Event", EuMW 2017 - Conf. Proceedings; 47th Eur. Microw. Conf. EuMC 2017*, vol. 2017-Janua, pp. 228–231, 2017.

[61] B. Schoch, A. Tessmann, S. Wagner, and I. Kallfass, "E-band Balanced Broadband Driver Amplifier MMIC with 1.8THz Gain-Bandwidth Product," *GeMIC 2020 - Proc. 2020 Ger. Microw. Conf.*, pp. 9–12, 2020.

[62] A. Serhan, E. Lauga-Larroze, and J. M. Fournier, "A V-Band BiCMOS power detector for millimeter-wave applications," *2013 25th Int. Conf. Microelectron. ICM 2013*, 2013.

[63] A. M. Couturier *et al.*, "E-band medium power amplifiers with gain control and output power detector," *Eur. Microw. Week 2013, EuMW 2013 - Conf. Proceedings; EuMIC 2013 8th Eur. Microw. Integr. Circuits Conf.*, pp. 133–136, 2013.

[64] A. Tessmann *et al.*, "A millimeter-wave low-noise amplifier MMIC with integrated power detector and gain control functionality," *IEEE MTT-S Int. Microw. Symp. Dig.*, vol. 2016-Augus, pp. 17–19, 2016.

[65] Y. Yang, B. Zhang, D. Ji, and Y. Fan, "220GHz GaAs Integrated Schottky Diode Mixer for Imaging System," *11th UK-Europe-China Work. Millim. Waves Terahertz Technol. UCMMT 2018 - Proc.*, vol. 1, pp. 1–3, 2018.

[66] C. Viegas, B. Alderman, J. Powell, H. Liu, H. Wang, and R. Sloan, "Characterization of 94 GHz and 183 GHz planar schottky diode based radiometer modules," *IEEE MTT-S Int. Microw. RF Conf. 2015, IMaRC 2015*, pp. 296–299, 2016.

[67] S. Koch, M. Guthoerl, I. Kallfass, A. Leuther, and S. Saito, "A 120-145 GHz heterodyne receiver chipset utilizing the 140 GHz atmospheric window for passive millimeter-wave imaging applications," *IEEE J. Solid-State Circuits*, vol. 45, no. 10, pp. 1961–1967, 2010.

[68] P. F. X. Neumaier *et al.*, "Molecular spectroscopy with a compact 557-GHz heterodyne receiver," *IEEE Trans. Terahertz Sci. Technol.*, vol. 4, no. 4, pp. 469–478, 2014.

[69] M. Sieth *et al.*, "Technology developments for a large-format heterodyne MMIC array at W-band," *Int. J. Microw. Wirel. Technol.*, vol. 4, no. 3, pp. 299–307, 2012.

[70] A. Di Gaspare, V. Giliberti, R. Casini, E. Giovine, F. Evangelisti, and M. Ortolani, "Sub-terahertz mixer based on heterostructure field effect transistor with integrated antennas," *2013 7th Eur. Conf. Antennas Propagation, EuCAP 2013*, vol. 1, no. EUCAP, pp. 1736–1739, 2013.

[71] C. Wang *et al.*, "0.34-Thz Wireless Link Based on High-Order Modulation for Future Wireless Local Area Network Applications," *IEEE Trans. Terahertz Sci. Technol.*, vol. 4, no. 1, pp. 75–85, 2014.

[72] M. Abbasi *et al.*, "Single-chip 220-GHz active heterodyne receiver and transmitter MMICs with on-chip integrated antenna," *IEEE Trans. Microw. Theory Tech.*, vol. 59, no. 2, pp. 466–478, 2011.

[73] M. Hoefle *et al.*, "89 GHz Schottky detector modules for MetOp-SG," *2016 Glob. Symp. Millim. Waves, GSMM 2016 ESA Work. Millimetre-Wave Technol. Appl.*, pp. 4–6, 2016.

[74] C. Hannachi and S. O. Tatu, "Millimeter-Wave Multi-Port Front-End Receivers: Design Considerations and Implementation," *IntechOpen*, 2018.

[75] A. Semenov *et al.*, "Schottky diode detectors for monitoring coherent THz synchrotron radiation pulses," *IPAC 2014 Proc. 5th Int. Part. Accel. Conf.*, pp. 3465–3467, 2014.

[76] H. Arab, S. Dufour, E. Moldovan, C. Akyel, and S. O. Tatu, "A 77-GHz six-port sensor for accurate near-field displacement and doppler measurements," *Sensors (Switzerland)*, vol. 18, no. 8, 2018.

[77] C. Goldstein, M. Trier, A. Maestrini, and J. C. Orlhac, "Present and future R&T development in CNES for Microwave radiometer," *2006 IEEE MicroRad Proc. - 9th Spec. Meet. Microw. Radiom. Remote Sens. Appl. MicroRad'06*, no. 0, pp. 60–65, 2006.

[78] P. Piironen, "Millimetre-Wave Direct Detection Receivers for Earth Observation Instruments - Trends and Challenges," *GSMM 2022 - 14th Glob. Symp. Millimeter-Waves Terahertz*, no. Ici, pp. 74–77, 2022.

[79] E. Bryerton, T. Reck, J. Hesler, and T. Crowe, "Sub-millimeter Wave Compact Correlation Radiometers," *2022 Asia-Pacific Microw. Conf.*, pp. 931–933, 2022.

[80] A. Fantom, "Radio Frequency and Microwave Power Measurement." Peter Peregrinus Ltd., Loddon, United Kindgom, London, 1990.

[81] R. Ginley, "Microwave Power Measurements," *IRE Trans. Instrum.*, vol. I–11, no. 3–4, pp. 257–263, 1962.

[82] Keysight Technologies Application Note, "Fundamentals of RF and Microwave Power Measurements (Part 2) Power Sensors and Instrumentation," 2014.

[83] D. Allal, D. Belieres, and M. Charles, "Development of a new DC-substitution RF power meter at LNE," *CPEM Dig. (Conference Precis. Electromagn. Meas.*, pp. 754–755, 2014.

[84] Keysight Technologies Data Sheet, "N432A Thermistor Power Meter."

[85] J. A. Lane and D. M. Evans, "The design and performance of transverse-film bolometers in rectangular waveguides," *Proc. IEE Part B Electron. Commun. Eng.*, vol. 108, no. 37, p. 133, 1961.

[86] I. Lemco and B. Rogal, "Resistive-Film Milliwatmeters For The Frequency Bands 8.2-12.4Gc/s, 12.4-18Gc/s and 26.5-40Gc/s," *Inst. Electr. Eng. Sep. 1960*, vol. 16, no. 3298, pp. 16–19, 1960.

[87] T. Inoue, I. Yokoshima, and M. Sasaki, "High-Performance Thin-Film Barretter Mount For Power Measurement In W-Band," *Electron. Lett.*, vol. 21, no. 5, pp. 170–172, 1985.

[88] S. M. Sze and K. N. Kwon, *Physics of Semiconductor Devices*, Third. Hoboken, New Jersey: John Wiley & Sons, Inc., 2007.

[89] V. L. Rideout, "A review of the theory, technology and applications of metal-semiconductor rectifiers," *Thin Solid Films*, pp. 261–291, 1978.

[90] K. Sakurai and T. Nemoto, "A Thin-Film Bolometer Unit," *IEEE Trans. Instrum. Meas. Sept. 1967*, vol. IM, no. 3, pp. 206–211, 1967.

[91] IEEE Instrumentation and Measurements Group, "IEEE Standard Application Guide for Bolometric Power Meters," 1972.

[92] D. D. Dinh and M. J. Lancaster, "Microwave power sensors with integrated filtering function for transfer power standards," *IEEE Microw. Wirel. Components Lett.*, vol. 30, no. 3, pp. 308–311, 2020.

[93] J. A. Lane, "Transverse film bolometers for the measurement of power in rectangular waveguides," *Proc. IEE - Part B Radio Electron. Eng.*, vol. 105, no. 19, pp. 77–80, 1958.

[94] N. Erickson, "A Fast , Very Sensitive Calorimetric Power Meter for Millimeter to Submillimeter Wavelengths," no. March, pp. 301–308, 2002.

[95] Y. Tojima, M. Kinoshita, H. Iida, and K. Fujii, "Calibrating Power Meters in the 140-220-GHz Frequency Range Using an Absolute-Power Reference Calorimeter," *IEEE Trans. Instrum. Meas.*, vol. 70, 2021.

[96] "Elmika Power Meters (M1-25M/XXE)." .

[97] L. Brunetti, "Thin-film bolometer for high-frequency metrology," *Sensors Actuators A. Phys.*, vol. 32, no. 1–3, pp. 423–427, 1992.

[98] L. Brunetti and E. Monticone, "Properties of nickel thin films on polyimide substrata for HF bolometers," *Meas. Sci. Technol.*, vol. 4, no. 11, pp. 1244–1248, 1993.

[99] N. Marcuvitz, *Waveguide Handbook*, First. McGraw-Hill Book Company, Inc, 1951.

[100] M. Salah Abdullatif, S. Hajjar, and A. Khanna, "Cost-effective, Accuracy Preserving Scalar Characterization for mmWave Transceivers," *IECON Proc. (Industrial Electron. Conf.*, vol. 2022-Octob, pp. 1–5, 2022.

[101] I. Dan, G. Ducournau, S. Hisatake, P. Szriftgiser, R. P. Braun, and I. Kallfass, "A superheterodyne 300 GHz wireless link for ultra-fast terahertz communication systems," *Int. J. Microw. Wirel. Technol.*, vol. 12, no. 7, pp. 578–587, 2020.

[102] "VDI - Erickson Power Meters (PM5B)." [Online]. Available: https://www.vadiodes.com/en/products/power-meters-erickson.

[103] H. Toda, K. Sasaki, Y. Nakagawa, and I. Sugiura, "Matched-Load-Type Thermoelectric Transducer for Power Measurements in the Millimeter Wave Region.," *IEE Conf. Publ.*, vol. IM, no. 113, pp. 188–190, 1974.

[104] H. Wang *et al.*, "A Monolithic W-band Preamplified Diode Detector," pp. 167–170, 1993.

[105] L. Zheng, L. Gilreath, V. Jain, and P. Heydari, "Design and analysis of a W-band detector in

0.18-μm SiGe BiCMOS," *2010 10th Top. Meet. Silicon Monolith. Integr. Circuits RF Syst. SiRF 2010 - Dig. Pap.*, no. 1, pp. 196–199, 2010.

[106] R. Malmqvist, C. Samuelsson, D. Dancila, S. Reyaz, M. Kaynak, and A. Rydberg, "Design and test results of a wideband sige detector and on-chip slot antenna for W-band sensing applications," *Proc. Int. Semicond. Conf. CAS*, vol. 1, pp. 205–208, 2012.

[107] M. Hoefle, A. Penirschke, A. Amrhein, O. Cojocari, M. Trier, and R. Jakoby, "Addressing the temperature stability in an 89 GHz Schottky detector design for radiometry," *Int. Conf. Infrared, Millimeter, Terahertz Waves, IRMMW-THz*, no. 2, pp. 1–3, 2012.

[108] Avago Technologies, "HSMS-286x Series Surface Mount Microwave Schottky Detector Diodes," pp. 1–18.

[109] S. Qayyum, M. D. Wei, and R. Negra, "Investigation of wideband and high sensitivity RF power detectors," *Eur. Microw. Week 2014 Connect. Futur. EuMW 2014 - Conf. Proceedings; EuMC 2014 44th Eur. Microw. Conf.*, pp. 758–761, 2014.

[110] Hewlett Packard Application Note 963, "Impedance Matching Techniques for Mixers and Detectors."

[111] J. Gutiérrez, K. Zeljami, J. P. Pascual, T. Fernández, and A. Tazón, "Comparison of microstrip w-band detectors based on zero bias schottky-diodes," *Electron.*, vol. 8, no. 12, 2019.

[112] L. A. Tejedor-Álvarez, J. I. Alonso, and J. González-Martín, "An ultrabroadband microstrip detector up to 40 GHz," *Proc. 14th Conf. Microw. Tech. Com. 2008*, no. August 2016, 2008.

[113] Q. Chen, X. Chen, H. Cai, and F. Chen, "A waveguide-fed 35-GHz rectifier with high conversion efficiency," *IEEE Microw. Wirel. Components Lett.*, vol. 30, no. 3, pp. 296–299, 2020.

[114] T. Suzuki, M. Ikeda, K. Sakakibara, N. Kikuma, and H. Hirayama, "Design of Waveguide-Input Millimeter-wave Detector Module."

[115] T. Ren, Y. Zhang, R. Xu, J. Zhou, C. Yang, and Z. Jin, "A 340-400 GHz Zero-Biased Waveguide Detector Using an Self-Consistent Method to Extract the Parameters of Schottky Barrier Diode," *Appl. Comput. Electromagn. Soc. J.*, vol. 30, no. 12, pp. 1334–1340, 2015.

[116] P. J. Meier, "Millimeter Integrated Circuits Suspended in the E-Plane of Rectangular Waveguide," *October*, pp. 726–733, 1978.

[117] J. de Mingo, A. Moliner, and A. Comeron, "Waveguide-to-Coupled Fin-Line Transition in Ka Band," vol. 6, no. October, pp. 363–365, 1996.

[118] J. N. Schulman *et al.*, "W-Band Direct Detection Circuit Performance With Sb-Heterostructure Diodes," *IEEE Microw. Wirel. Components Lett.*, vol. 14, no. 7, pp. 316–318, 2004.

[119] J. L. Hesler and T. W. Crowe, "NEP and Responsivity of THz Zero-Bias Schottky Diode Detectors," *IRMMW-THz2007 - Conf. Dig. Jt. 32nd Int. Conf. Infrared Millimetre Waves, 15th Int. Conf. Terahertz Electron.*, pp. 844–845, 2007.

[120] Y. Changfei, Z. Ming, L. Yunsheng, and X. Conghai, "Millimeter wave broadband high sensitivity detectors with zero-bias Schottky diodes," *J. Semicond.*, vol. 36, no. 6, pp. 1–5, 2015.

[121] M. Tekbas, M. S. Erdogan, and I. Unal, "A W band waveguide detector module using zero bias schowttky diode," *2017 IEEE 37th Int. Conf. Electron. Nanotechnology, ELNANO 2017 - Proc.*, pp. 137–142, 2017.

[122] K. Xu, Y. Zhang, L. Xie, and Y. Fan, "A Broad W-band Detector Utilizing Zero-bias Direct Detection Circuitry," *2011 Int. Conf. Comput. Probl. ICCP 2011*, pp. 190–194, 2011.

[123] W. Zhang, F. Yang, and Z. X. Wang, “W-band(90GHz) Zero Bias Schottky Diode Directive Detector,” *Asia-Pacific Microw. Conf. Proceedings, APMC*, vol. 2, pp. 7–9, 2016.

[124] J. Li, H. Hu, and H. Sun, “A Zero-bias GaAs W-band Microstrip Detector Circuit,” *2014 IEEE Int. Conf. Commun. Probl. ICCP 2014*, pp. 569–571, 2014.

[125] L. Xie, Y. Zhang, Y. Fan, C. Xu, and Y. Jiao, “A W-band Detector with High Tangential Signal Sensitivity and Voltage Sensitivity,” *2010 Int. Conf. Microw. Millim. Wave Technol. ICMMT 2010*, no. 60632020, pp. 528–531, 2010.

[126] J. Campion *et al.*, “An Ultra Low-Loss Silicon-Micromachined Waveguide Filter for D-Band Telecommunication Applications,” *IEEE MTT-S Int. Microw. Symp. Dig.*, vol. 2018-June, pp. 583–586, 2018.

[127] S. R. Zahran, L. Boccia, G. Amendola, S. Moscato, M. Oldoni, and D. Tresoldi, “Broadband D-Band Antenna Array Based on 64 Stepped Horns for 5G Backhauling Applications,” *15th Eur. Conf. Antennas Propagation, EuCAP 2021*, 2021.

[128] David M Pozar, *Microwave Engineering, 4th Edition*. JohnWiley & Sons, Inc., 2011.

[129] Z. Wu and C. H. Ahn, “A WEARABLE PRESSURE AND TEMPERATURE SENSOR ARRAY USING Zhizhen Wu and Chong H . Ahn,” *19th Int. Conf. Solid-State Sensors, Actuators Microsystems*, 2017.

[130] A. Zawadzka, P. Płóciennik, K. Waszkowska, D. Guichaoua, and B. Sahraoui, “Nonlinear Optical Properties of Oxide Thin Films,” *Int. Conf. Transparent Opt. Networks*, vol. 2018-July, pp. 47–49, 2018.

[131] M. B. Heaney, *Electrical Conductivity and Resistivity*. 2004.

[132] N. Hiromoto *et al.*, “High Responsivity and Low NEP of Room-Temperature Terahertz Antenna-Coupled Microbolometers with Meander Titanium Thermistor,” *Int. Conf. Infrared, Millimeter, Terahertz Waves, IRMMW-THz*, vol. 2019-Septe, 2019.

[133] R. S. Saxena, R. K. Bhan, C. R. Jalwania, and K. Khurana, “Effect of excessive bias heating on a titanium microbolometer infrared detector,” *IEEE Sens. J.*, vol. 8, no. 11, pp. 1801–1804, 2008.

[134] “Resistivity and Conductivity - Temperature Coefficients Common materials.” [Online]. Available: https://www.engineeringtoolbox.com/resistivity-conductivity-d_418.html.

[135] “Table of Electrical Resistivity and Conductivity.” [Online]. Available: https://www.thoughtco.com/table-of-electrical-resistivity-conductivity-608499.

[136] “NESS ENGINEERING TECHNICAL DATA METAL / ALLOY RESISTIVITY.” [Online]. Available: https://www.nessengr.com/techdata/metalresis.html.

[137] “Resistivity and Temperature Coefficient at 20 C.” [Online]. Available: http://hyperphysics.phy-astr.gsu.edu/hbase/Tables/rstiv.html.

[138] H. Hoffmann and J. Vancea, “Critical assessment of thickness-dependent conductivity of thin metal films,” *Thin Solid Films*, vol. 85, no. 2, pp. 147–167, 1981.

[139] W. Zhang *et al.*, “Influence of the electron mean free path on the resistivity of thin metal films,” *Microelectron. Eng.*, vol. 76, no. 1–4, pp. 146–152, 2004.

[140] J. S. Agustsson *et al.*, “Electrical resistivity and morphology of ultra thin pt films grown by dc magnetron sputtering on SiO2,” *J. Phys. Conf. Ser.*, vol. 100, no. PART 8, 2008.

[141] M. Avrekh, O. R. Monteiro, and I. G. Brown, “Electrical resistivity of vacuum-arc-deposited

platinum thin films," *Appl. Surf. Sci.*, vol. 158, no. 3, pp. 217–222, 2000.

[142] N. Arshi, J. Lu, C. G. Lee, J. H. Yoon, B. H. Koo, and F. Ahmed, "Thickness effect on properties of titanium film deposited by d.c. magnetron sputtering and electron beam evaporation techniques," *Bull. Mater. Sci.*, vol. 36, no. 5, pp. 807–812, 2013.

[143] S. P. Morgan, "Effect of Surface Roughness on Eddy Current Losses at Microwave Frequencies," *J. Appl. Phys.*, vol. 20, no. 4, pp. 352–362, 1949.

[144] T. Edwards and M. Steer, *Foundations for Microstrip Circuit Design*, Fourth Edi. Wiley.

[145] "DuPont ™ Kapton ® Summary of Properties," *Dupont Datasheet*, pp. 1–20.

[146] S. A. Book, "Why n - 1 in the Formula for the Sample Standard Deviation ?," *Two-Year Coll. Math. J.*, vol. 10, no. 5, pp. 330–333, 1979.

[147] X. Wan, W. Wang, J. Liu, and T. Tong, "Estimating the sample mean and standard deviation from the sample size, median, range and/or interquartile range," *BMC Med. Res. Methodol.*, vol. 14, no. 1, pp. 1–13, 2014.

[148] F. Braun, "Lieber die Stroinleitung durch Scliwefelmetulle," 1874.

[149] W. Schottky, "Halbleitertheorie der Sperrschicht," vol. 26, no. 8, p. 938, 1938.

[150] W. Monch, "On the physics of metal-semiconductor interfaces," *Eur. J. Phys.*, vol. 20, no. 3, 1990.

[151] D. T. Young and J. C. Irvin, "Millimeter Frequency Conversion Using Au-n-Type GaAs Schottky Barrier Epitaxial Diodes with a Novel Contacting Technique," *Proc. IEEE*, vol. 53, no. 12, p. 2130, 1965.

[152] S. Jenabi, D. Deslandes, F. Boone, and S. A. Charlebois, "A low-cost fabrication method for sub-millimeter wave GaAs Schottky diode," *Semicond. Sci. Technol.*, vol. 32, no. 10, 2017.

[153] "Electron Work Function of The Elements." [Online]. Available: https://public.wsu.edu/~pchemlab/documents/Work-functionvalues.pdf.

[154] A. M. Cowley and H. O. Sorensen, "Quantitative Comparison of Solid-State Microwave Detectors," pp. 588–602, 1966.

[155] B. C. Wadell, "Transmission Line Design Handbook," *Artech House*, p. 1991, 1991.

[156] Y.-C. Shish, T.-N. Ton, and L. Q. Bui, "Waveguide-To-Microstrip Transition for Millimeter-Wave Applicaiton," *IEEE*, 1988.

[157] Y.-C. Leong and S. Weinreb, "Full Band Waveguide-to-Microstrip Probe Transitions," *IEEE MTT-S Int. Microw. Symp. Dig.*, 1999.

[158] S. Llorente-Romano, B. P. Dorta-Naranjo, F. Perez-Martinez, and M. Salazar-Palma, "Design, Implementation and Measurements of Ka-band Waveguide-to-microstrip Transitions," *2002 32nd Eur. Microw. Conf. EuMC 2002*, pp. 2–5, 2002.

[159] H.-W. Yao, A. Abdelmonem, J.-F. Liang, and K. A. Zaki, "A Full Wave Analysis of Microstrip-To-Waveguide Transitions," *IEEE MTT-S Int. Microw. Symp. Dig. (Cat. No.94CH3389-4)*, 1994.

[160] M. Simone, A. Fanti, G. Valente, G. Montisci, R. Ghiani, and G. Mazzarella, "A Compact In-Line Waveguide-to-Microstrip Transition in the Q-Band for Radio Astronomy Applications," *Electron.*, vol. 7, no. 2, pp. 1–9, 2018.

[161] J. L. Hesler *et al.*, “Fixed-tuned submillimeter wavelength waveguide mixers using planar schottky-barrier diodes,” *IEEE Trans. Microw. Theory Tech.*, vol. 45, no. 5 PART 1, pp. 653–658, 1997.

[162] J. L. Hesler, “Planar Schottky Diodes In Submillimeter-Wavelength Waveguide Receivers,” University of Virginia, 1996.

[163] Keysight Technologies Technical Overview, “Harmonic Balance (HB) Simulation,” pp. 1–14.

[164] “DiCap ® High Performance Single-Layer Capacitors for RF, Microwave, and Millimeter-Wave Applications,” *Compon. Distrib. Datasheet*, pp. 8–11.

Appendix A

Publications

1. **H. Kamble**, M. Salek, X. Wang, M. Celep, D. Stokes, J. Skinner and Y. Wang, “D-Band Thin-Film Resistive Line Bolometer as Transfer Standard,” IEEE Transactions on Microwave Theory and Techniques, pp. 1–11, 2023.

2. **H. Kamble**, M. Salek and Y. Wang, “Zero-biased Schottky Diode Power Detector for D-band,” 16th UK-Europe-China Workshop on Millimetre Waves and Terahertz Technologies (UCMMT2023), Guangzhou, China.

D-band Thin-Film Resistive Line Bolometer as Transfer Standard

Harshwardhan Kamble, Milan Salek, Xueshen Wang, Murat Celep, *Senior Member, IEEE*, Daniel Stokes, James Skinner, *Member, IEEE*, Yi Wang, *Senior Member, IEEE*

***Abstract*— A bolometric thin-film based transfer standard with a novel structure for absolute power detection in D-band (110 - 170 GHz) is reported. It uses a resonance-type matching technique with thin-film resistive lines. The same line functions as the sensing element. The change in the resistivity of the line under the incident wave is calibrated to measure the absolute RF power in the D-band. This paper presents the analysis using equivalent circuit models, the full-wave electromagnetic design, the fabrication and the comprehensive characterization of the device. The comparison between a single and a folded-line matching structure is performed, showing the wideband capability of the latter. The transfer standard consists of two sensors in one waveguide housing for RF power measurement, as well as for monitoring and calibrating out the ambient temperature variation. It has shown a very good short-term time response with only ~0.19 % deviation in a given time interval, which is very close to a commercial PM5 sensor with ~0.27 % deviation. The long-term time response is also impressive, with a deviation of less than 0.6 %, similar to a commercial PM5 sensor. The fast response time, good thermal isolation and ambient compensation ability make it suitable for transfer/working standards, which can be used in ambient temperature environments.**

***Index Terms*— Barretter mount, bolometer, metrology millimetre wave, power sensor, thin-film, transfer standard.**

I. INTRODUCTION

In the electromagnetic spectrum, microwave (3 – 30 GHz) and millimetre-wave (30 - 300 GHz) bands have a major contribution in communication, defence, astronomy, and medical applications. However, the sub-terahertz (sub-THz) band above 100 GHz is not substantially commercialised [1]. Today this band is mostly used for scientific research. One of the reasons why this band has been immature for many years is the manufacturing challenges at very short wavelengths (λ < 3 mm). Considerable research is going on to utilise this band by employing advanced fabrication techniques such as high-precision CNC machining, micromachining and 3D printing [2]. Another reason is that very few commercial sources and detectors are readily available, as solid-state devices often suffer from excessive losses and limited efficiency [1]. In the past few years, the commercial exploitation of the sub-THz band, especially around the D-band (110 - 170 GHz), is gaining momentum because of the emerging applications in back-haul communications and high-resolution radars. With these also comes the increasing demand for power measurement above 110 GHz for metrology and qualification.

One of the most demonstrated power measurement techniques is the calorimetric technique which is frequency independent [3], [4], and uses matched-load usually made of absorptive materials on tapered sections. Sensor elements employed include thermoelectric (single load [5], dual load [6], quasi twin [7]) or bolometric (thermistor [8], thin film [4], [9]) types. Such loads are also used as power-absorbing terminals in a twin-load configuration [10], [11]. However, the calorimeter is a primary power measurement standard and requires a very long heat settling time due to its bulky structure and high thermal mass [3], [4], [7]. A traceable/working standard (not only as a calorimetric load) is required for commercial users with a simple design and fast response time. The power detector in this paper is designed for such purposes.

Above 100 GHz, building a thermistor bead or platinum wire bolometer in a waveguide is difficult due to the space constraint, and their losses would significantly reduce the efficiency. Therefore, barretter mount based designs using metallic thin-film lines are adopted in this work. Similar techniques have been reported in [12]–[16] but at much lower frequencies. So far, the highest operation frequency of room temperature thin-film bolometer barretter mount is at 94 GHz reported in 1985 [15]. Some existing power standards are compared in Table I. We intend to compare all the metrology sensors above 75 GHz. Most of them are based on matched load. We also include three lower frequency sensors [12] [18] [24] as examples of the resonant-type sensor. Unfortunately, not all the key parameters (such as settling time) are provided in the literature. Some of the comparisons may be further qualified depending on the power level and scale used in the measurement. Some of the response time data were taken as an estimate from the figure provided in the literature.

In this paper, a novel thin-film resistive-line based power detector is designed, fabricated, and characterised for transfer/

Manuscript received …: revised …. H. K. acknowledges the financial support from Rajarshi Shahu Maharaj Foreign Scholarship awarded by Social Justice and Special Assistance Department, State Government of Maharashtra, India. The work described in this paper was partly funded by the National Measurement System Directorate of the U.K. Government Department for Business, Energy and Industrial Strategy. *(Corresponding author: Yi Wang)*

H. Kamble, M. Salek and Y. Wang are with the School of Engineering, University of Birmingham, Birmingham B15 2TT, U.K. (e-mail: hxk940@student.bham.ac.uk; m.salek@bham.ac.uk; y.wang.1@bham.ac.uk).

M. Celep, D. Stokes and J. Skinner are with the National Physical Laboratory, Teddington, TW11 0LW, U.K. (e-mail: murat.celep@npl.co.uk, daniel.stokes@npl.co.uk, james.skinner@npl.co.uk).

X. Wang is with National Institute of Metrology, Beijing 100029, China. (e-mail: wangxs@nim.ac.cn)

TABLE I

POWER STANDARDS COMPARISON

Ref. Year	Freq (GHz)	Time (sec)	Resistance (Ω)	Matching Type	Remarks
This work	110-170	< 2.6	1600	Resonance	90% Response time; Bolometric Transfer Standard; Input power ~ 22.5 mW
[4] 2022	110-170	2400	205.5	Matched Load	Rise Time; Microcalorimeter; Input power ~ 31.5 mW
[17] 2021	140-220	~300	-	Matched Load	90% Response time (graph); Calorimetric; Reference Standard
[9] 2018	110-170	-	1000	Matched Load	Calorimeter element
[18] 2018	50-75	-	200	Resonance	Calorimeter; Thermistor mount
[19] 2018	75-110	-	-	Matched Load	Calorimeter using VDI Erickson PM5
[6] 2017	110-170	-	-	Matched Load	Calorimeter; Thermocouple
[20] 2016	75-110	0.2	-	Matched Load	90% Response time (20 mW scale); VDI Erickson PM5 with feedback
[21] 2015	75-110	-	50	Matched Load	Calorimetric Transfer Standard; Waveguide to CPW Transition
[8] 2015	110-170	-	-	Matched Load	Microcalorimeter
[10] 2010	75-110	~ 3000	-	Resonance	90% Time constant (graph); Thermistor Mount
[5] 2006	110-170	30	-	Matched Load	Response time (at 5 mW); Calorimeter with Feedback
[22] 2006	75-110	0.4	-	Matched Load	90% Response time (scale 20 mW); Calorimeter PM1B with feedback
[3] 1999	75-110	0.45	-	Matched Load	Time constant (scale 20 mW); Calorimeter with Feedback
[23] 1974	60-90	< 0.8	200	Matched Load	Response time of practical transducer; Thermocouple at resistive strip
[12] 1960	26.5-40	~ 15	609	Resonance	Time constant; Bolometer-Milliwatmeter
[24] 1958	8.20-12.40	15, 3	480-500	Resonance	Time constant of system (≥ 10 mW); 9.2 GHz; Thermocouple at the centre of film

working standard in the D-band. The power detector consists of two sensors A and B. The first is the main/active sensor to measure incident power, and the second is the dummy sensor for temperature compensation. As far as the author's knowledge, this is a unique type of barretter mount structure which has never been reported before in D-band or above. Other novelties and key features of the sensors are: (1) A resonance-type sensor covering the whole D-band. Resonant matching generally has poorer matching and narrowed bandwidth than matched load. We have used a folded-line structure to generate more matching points so as to increase the bandwidth to cover the whole D-band. (2) Fast response time. This is achieved through a compact design and effective thermal isolation. We have used quartz substrate and polyimide (Kapton) insulation tape. The sensor body is made of low thermal conductivity plastic (polyether ether ketone or PEEK). All help reduce the thermal time constant. (3) Temperature compensation using a compact dual-sensor configuration. This is to remove the impact of ambient temperature on the power measurement. These features and the portability of the sensor make it highly suitable as a transfer standard which is used to establish the traceability between the primary standard at the metrology organisation and industrial users.

In section II, the design and comparison between a single-line and a folded-line matching structure are explained. Section III shows the complete design of the power sensor. Section IV presents the fabrication and assembly. Section V discusses the power sensor characterisation before conclusions in Section VI.

II. THIN-FILM RESISTIVE LINE MATCHING STRUCTURE

The impedance matching and power sensing both rely on a thin-film resistive line. It uses a resonance-type matching technique which is inherently narrow band. We will first investigate and compare two matching structures with an objective to achieve a matched load across the D-band.

A. Single-Line Design

The conventional thin-film power detector only contains one section of the line placed at an off-set distance from the back-short. The circuit solution to such a line placed in a waveguide facing the input port has been detailed in [13]. Here a similar method is applied to a thin-film line facing the narrow wall of the waveguide instead, as shown in Fig. 1. This sidewall-facing E-plane configuration makes it convenient to accommodate more than one section of the line on the substrate in an effort to improve bandwidth, which will be discussed later in section B. The waveguide used is a standard D-band (WR-6) waveguide with internal dimensions of 1.651 mm by 0.826 mm.

The single resistive line is parallel to the electric field coming in the waveguide, and the electric field induces current oscillating in the line. The metallic thin-film line behaves as an inductor with a reactance X and a resistance R, as shown in the equivalent circuit in the inset of Fig. 2. The following can be written [13],

$$Z_{sc} = +j \cdot Z_0 tan(\beta l_s) \tag{1}$$

$$Z_1 = \frac{Z_{sc} \times F_1}{Z_{sc} + F_1} \tag{2}$$

where Z_{SC} is the short circuit impedance at a distance l_S from the back-short, which is in parallel to $F_1 = R + jX$, the impedance of the line. Z_1 is the overall equivalent input impedance.

The maximum current will only be induced and heat up the line when the structure in Fig. 1 is well matched. That is, the port should only see the purely resistive termination. The following two equations of matching conditions can be derived by equating the real term of (2) to Z_0 and the imaginary to zero [13],

$$X = \sqrt{R \cdot Z_0 - R^2} \tag{3}$$

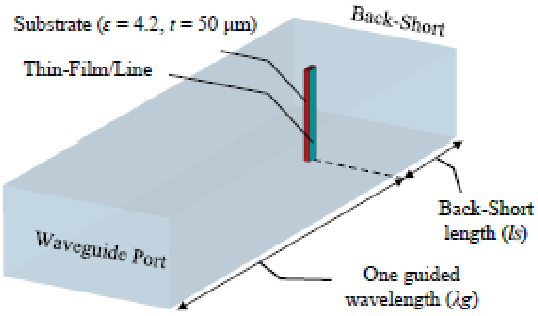

Fig. 1. Single-line matching structure inside the waveguide shorted at one end.

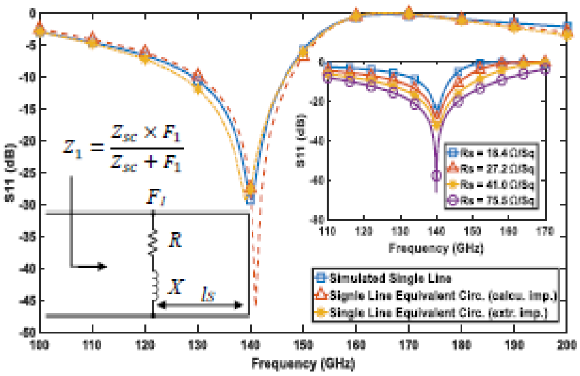

Fig. 2. Simulated S_{11} of the matched single-line in Fig. 1 (with different sheet resistance, R_s), in comparison with the calculated responses from the circuit model. The inset shows the equivalent circuit diagram of the single-line design.

$$l_s = \frac{1}{\beta} \cdot \tan^{-1}\left(\frac{-R}{X}\right) \tag{4}$$

where β is the propagation constant. The resistance, R, of the line depends on the material and its dimensions (length, width and thickness). The reactance, X, depends on the waveguide characteristic impedance, frequency and the width w of the line.

The impedance of the line can either be approximated using the analytical formula (for lines facing the port) given in [25] or extracted from the simulated reflection coefficient. To do so, the line is placed at the centre of a waveguide of a length of $2\lambda_g$ as shown in Fig. 3. The thin-film line impedance F can be linked to the linear reflection coefficient Γ as follows,

$$F = R + jX = -\frac{(1+\Gamma)}{2 \cdot \Gamma} Z_0. \tag{5}$$

Therefore, the equivalent R and X of the line can be extracted from the simulated reflection coefficient Γ.

Although the DC resistance of the power sensor element (thin-film line or thermistor) can usually be flexibly chosen,

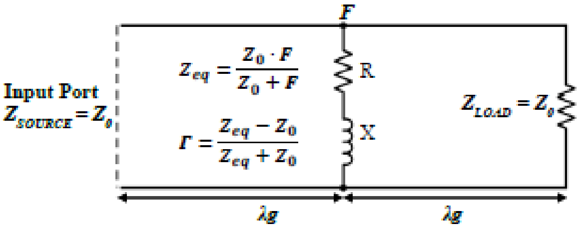

Fig. 3. Equivalent circuit diagram showing the method to extract the impedance of the thin-film line from the simulated reflection coefficient.

typically, this is around 200 Ω to match the widely available self-balancing bridge circuit in metrology [16], [26]. This value is initially chosen in this single-line design. It is worth noting that the R value is not prescribed for the final design.

Once R for the single-line design is chosen, the required X is determined from (3), and in turn, the back-short distance l_s can be found from (4). The length of the resistive line, in this case, equals to the internal height of the waveguide which is 0.826 mm. The width of the line w can either be found using the analytical formula in [17] or extracted from X using the method in Fig. 3. The sheet resistance R_S can be calculated by (6), which in turn can be used to determine the required film thickness t,

$$R_S = \frac{1}{\sigma \cdot t} = \frac{R \cdot w}{l}. \tag{6}$$

As an example, at the central frequency (140 GHz) of the D-band, the line width is found be 112 µm from the simulation. The extracted impedance of the line is 231+j233 Ω. The back-short distance l_s is calculated to be 1.059 mm from (4). The required sheet resistive is 27.2 Ω/Sq.

From Fig. 2, it can be seen that the calculated response from the equivalent circuits agrees well with the full-wave simulation using CST Studio Suite, which validated the circuit approach. Further simulation from Fig. 2 shows that a higher sheet resistance R_S (corresponding to a higher R value) would improve the impedance matching. However, it also means thinner film is required. For instance, if the widely used platinum is to realise the sheet resistance of 27.2 Ω/Sq, the film thickness would be 4 nm based on its nominal conductivity of 9.434 ×10⁶ S/m. This thickness would cause difficulty in term of its reproducibility in deposition. Fig. 2 also indicates, as expected, that the single-line solution only offers limited bandwidth.

B. Folded-Line Design

To enhance the matching bandwidth, a folded-line structure is proposed as shown in Fig. 4. The design has used the knowledge gained from equivalent circuit analysis. At the start of the design process, only the two vertical sections of the folded-line are considered to simplify the circuit analysis. The idea is to create more matching points across the band, so the

TABLE II

DESIGN PARAMETERS FOR 200 Ω RESISTANCE AT THREE DIFFERENT FREQUENCIES

Design frequency (GHz)	120	140	160
Chosen DC line (Single) resistance (Ω)	200	200	200
Line width (µm)	64	112	157
Sheet resistance (Ω/Sq)	15.6	27.2	38

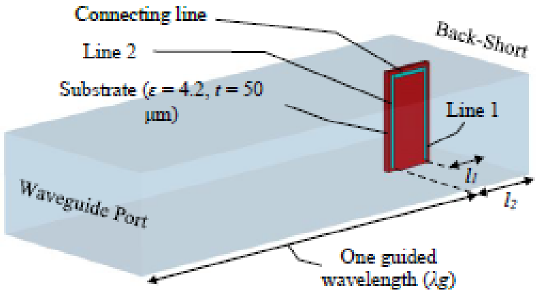

Fig. 4. Folded-line matching structure inside the waveguide shorted at one end.

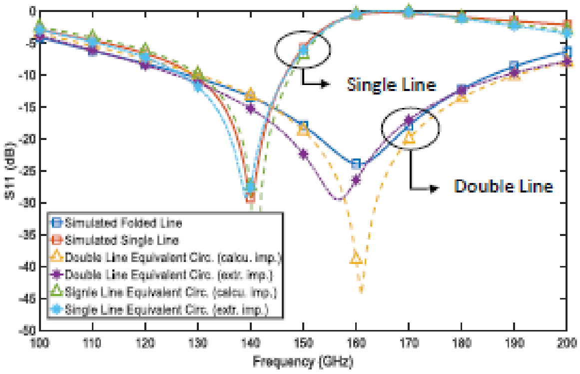

Fig. 5. Comparison of reflection coefficient curves obtained from the simulation and the equivalent circuit

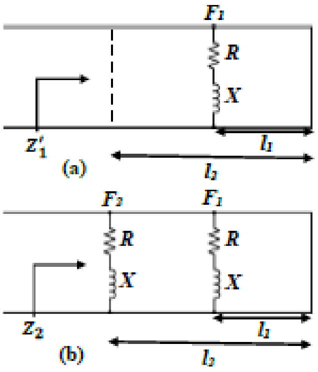

Fig. 6. Equivalent circuit diagram of the two lines: (a) Before adding Line 2, (b) After adding Line 2.

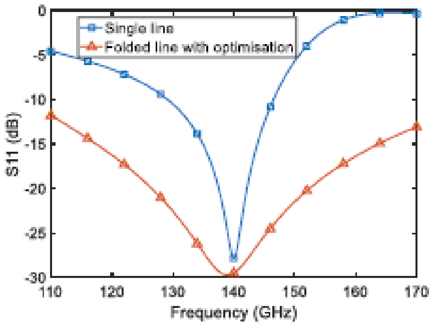

Fig. 7. Simulated S_{11} of the optimised single and folded-line structures (R_S = 27.2 Ω/Sq).

initial dimensions of the matched single-line at three different frequencies (120, 140, and 160 GHz) are first obtained from (3) – (5). These parameters are given in Table II. The impedances of these three lines are extracted from the simulated reflection coefficient as in Fig. 3. The corresponding back-short lengths can then be calculated from (4). For the initial design, as a comprise, the sheet resistance is chosen to be the value obtained from the central frequency of 140 GHz, i.e., 27.2 Ω/Sq, whereas the off-sets of the two lines (Line 1 and Line 2 in Fig. 4) are chosen to be the values obtained for 120 and 160 GHz, respectively. It is observed that using small line width improves return loss. After optimisation, the response in Fig. 5 is obtained where w = 0.032 mm, l_1 = 0.903 mm and l_2 = 0.533 mm. Note that still only the two vertical sections of the line are considered so far.

Figure 6 shows the equivalent circuit diagram of the dual-line structure, excluding the connecting strip that joins the two lines. Assume the impedance of both lines is the same (F_1 = F_2). The input impedance seen at a distance of l_2 to the back-short, excluding the parallel Line 2 is,

$$Z_1' = Z_0\frac{Z_1 + jZ_0 tan\beta(l_2 - l_1)}{Z_0 + jZ_1 tan\beta(l_2 - l_1)} \tag{7}$$

where Z_1 is the input impedance seen at a distance of l_1 to the back-short and given in (2). Therefore, the overall input impedance, Z_2, is a result of parallel Z_1' and the line impedance of F_2, i.e.,

$$Z_2 = \frac{Z_1' \times F_2}{Z_1' + F_2} \tag{8}$$

The calculated impedance based on the line dimension as well as the extracted impedance from CST, are used in (8). The calculated S-parameter responses from these two different approaches agree very well, as shown in Fig. 5. They are also in good agreement with the simulated responses. It is important to note from Fig. 6 that the two-line design has much wide bandwidth than the single-line design. However, the matching point of the two-line design is shifted upward to about 160 GHz. At this point, a horizontal line is added to connect the two vertical lines, forming a dc path as required for sensor readout. This lowers the matching frequency and worsens the matching. After further optimisation (w = 0.035 mm, l_1 = 0.773 mm and l_2 = 0.403 mm), the matching point is corrected back to 140 GHz. As shown in Fig. 7, a return loss of over 10 dB can be achieved across the D-band. The advantage of the bandwidth is again very clear from the comparison with an optimised single-line design based on the same sheet resistance of 27.2 Ω/Sq. It should be noted that the DC resistance (R) of the folded-line has been increased to 1.96 kΩ.

III. COMPLETE DESIGN

The actual sensor with the presented folded-line structure will be housed in D-band waveguide with a UG-387 flange. The sensor chip will be fitted into a holding recess and inserted into the waveguide along the E-plane, as shown in Fig. 8. The complete design consists of the main sensor (sensor A) for detecting incident microwave power and the dummy sensor without a flange (sensor B) for detecting ambient temperature variation. The sensor housing needs to be designed to allow for secure installation of the sensor chip and to thermally isolate it from ambient temperature drift

The sensor chip is 6.6 mm × 2.0 mm × 0.1 mm (length × width × thickness) in size, as illustrated in Fig. 9. Substrate materials with low thermal conductivity such as polyimide (thermal conductivity = 0.12 W/m·K) and quartz (3 W/m·K) are good options. A quartz substrate (ε = 3.75, thickness of 100 µm) is chosen to fabricate the sensor chip. The polyimide tape is used to hold the chip securely in the rectangular slot and to isolate the chip from the housing.

The material for the sensor line should have high temperature coefficient, high resistivity and be compatible with the quartz substrate in fabrication. Nichrome [12][13], nickel [14][15], and platinum [24] materials have been mostly used as sensing elements. Titanium has also been used for detecting terahertz [27] and infrared [28] radiations. Titanium has higher resistivity (430 nΩ·m) than Platinum (106 nΩ·m), while both have similar temperature coefficients. Therefore, titanium is chosen for the thin-film line, for ease of fabrication, which allows a larger film thickness (15.5 nm) than a platinum line (4 nm) to achieve the same sheet resistance of 27.2 Ω/Sq. Two gold-coated pads are added for DC connection above the line, as shown in Fig. 9. Two spring-loaded DC connection pins press down from the holes for each sensor, as shown in Fig. 8.

Several changes have been made to fit the folded-line design (Fig. 4) in the housing. The substrate size has to be increased to accommodate the DC pads. This has led to leakage through the substrate and spurious resonances. The reflecting-strip was added to limit the signal leakage to the large side cavity containing the substrate and reduce the spurious resonances at higher frequencies. It has also helped to align the polyimide tape after fabrication. Polyimide wrapping is used to isolate the chip from the surrounding body and to fit into the housing. This has also affected the matching but not in a significant way, as shown in Fig. 10 when different thicknesses of the wrapping (0, 250, and 500 µm) around the chip are simulated to see the effect on S_{11}. Also shown in Fig. 10 is the matching point in the simulated S_{11} that has shifted from 140 to 132 GHz. Some ripples appear, which is believed to be a result of some weak resonances from the recess used to hold

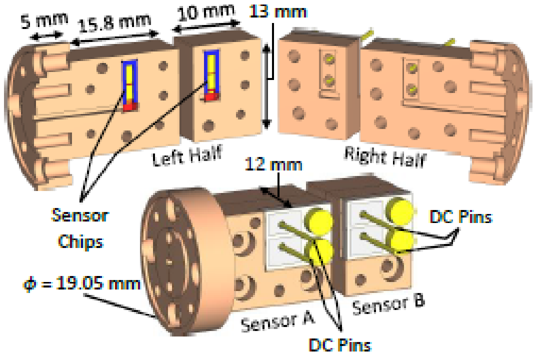

Fig. 8. Illustration of the detector housing, showing the chip placement.

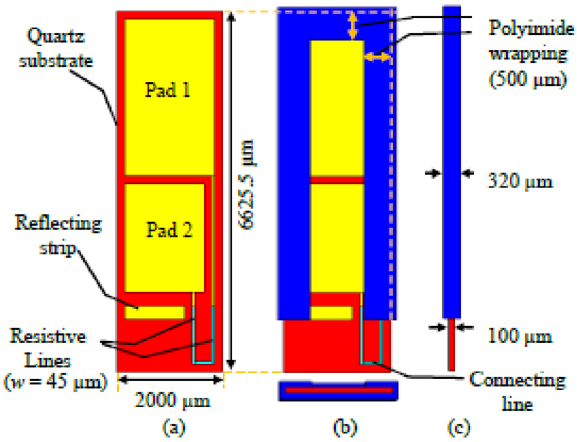

Fig. 9. Layout of the sensor chip: (a) chip (b) chip covered in polyimide (c) side view.

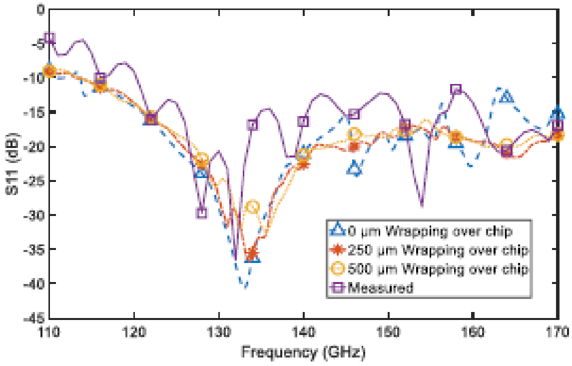

Fig. 10. Simulated result of the final design model with the housing compared to the measurement.

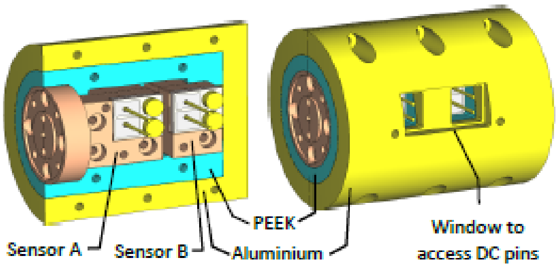

Fig. 11. Design of sensor A and B in thermal shielding.

the chip and the gaps around the chip in the waveguide. The measured reflection coefficient from Section V is also plotted with the simulated S_{11} in Fig. 10 for comparison, they are in good agreement. The final updated parameters are w = 0.045 mm, l_1 = 0.803 mm and l_2 = 0.433 mm. The DC resistance of the sensor is calculated to be 1.5 kΩ.

The two sensors (A and B) should be placed together to ensure the sensing of the same ambient temperature and simultaneously be thermally isolated from each other. The latter is facilitated by an air gap of 2 mm. The sensor B is used to compensate out the ambient temperature variations from sensor A so that the absolute RF power can be measured. The sensors are also found to be very sensitive to handling and airflow, so they are shielded, as shown in Fig. 11. The inner shielding is made of PEEK material, and the outer one is made of aluminium.

IV. SENSOR FABRICATION

The fabricated sensor chips are shown in Fig. 12(a). The titanium thin film was evaporated on the quartz substrate. At the nominal thickness of 15.5 nm, the measured sheet resistance is 79.3 Ω/sq, about three times higher than the design requirement. The film thickness is therefore increased to reach 27 Ω/sq. The DC pads were coated with gold of 100 nm. The measured resistance of the folded-line is ~1.6 kΩ which is consistent with the design. 50 µm thick polyimide tape was used to wrap the chip and fit it into the housing.

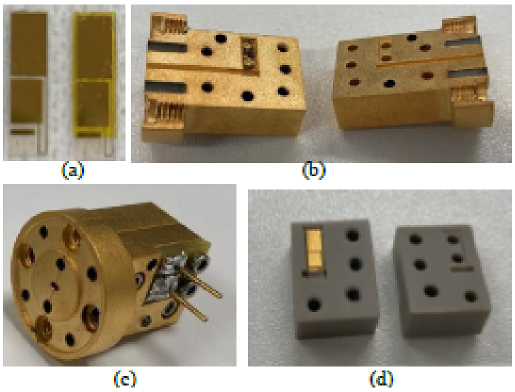

Fig. 12. Fabricated sensors: (a) Sensor chips before and after wrapping with polyimide; (b) Sensor A in split blocks; (c) Assembled Sensor A; (d) Sensor B in split blocks with the chip installed.

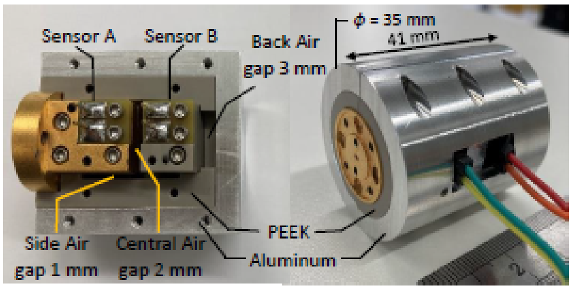

Fig. 13. Fabricated sensors A and B in thermal shielding.

As shown in Fig. 12 (b) - (d), the sensor bodies are made out of the thermoplastic polymer PEEK, which has a low thermal conductivity of 0.25 W/m·K, to reduce the effect of surrounding temperature drift. The body of Sensor A is gold-plated, whereas Sensor B is not plated, as it does not carry any microwave signal. The absence of the gold coating also helps with thermal isolation.

Sensors A and B are placed inside the shielding (shown in Fig. 13), which helps with the handling and reduces the effect of ambient temperature fluctuation. The shielding also ensures a similar ambient environment for both sensors. The sensor bodies are held inside the PEEK shielding only at the corners. There is an air gap of 1 mm surrounding it for thermal isolation. The air gap between the sensors is kept 2 mm. This will minimise the amount of heat exchange between the sensor A and B. All these measures aim to reduce the correlation between the two sensors so that Sensor B can trace the ambient temperature only. The size of the cylindrical aluminium shielding is 35 mm × 41 mm (outer diameter × length), which is comparable to that of the commercially available PM5 (51 mm × 48 mm × 76 mm).

V. SENSOR CHARACTERIZATION

The performance of the sensor has been evaluated through the measurement of voltage reflection coefficient (VRC or S_{11}), short- and long-term time responses, linearity and frequency response as described in [4]. These parameters can be used to characterize the sensor behaviour when a microwave signal is incident for real applications.

A. Voltage Reflection Coefficient, VRC or S_{11}

The VRC of sensor A was measured using a vector network analyser (VNA) with a D-band waveguide extender. A D-band calibration kit was used to calculate the error terms of the VNA-extender combination using a through-reflect-line calibration methodology. Sensor A was connected to the extender's waveguide port. VRC was measured and is illustrated in magnitude and phase in Fig. 14. The sensor output was not connected to any other instrumentation during this measurement.

The measured VRC shows good agreement with the simulation, as shown in Fig. 10. The VRC magnitude of the

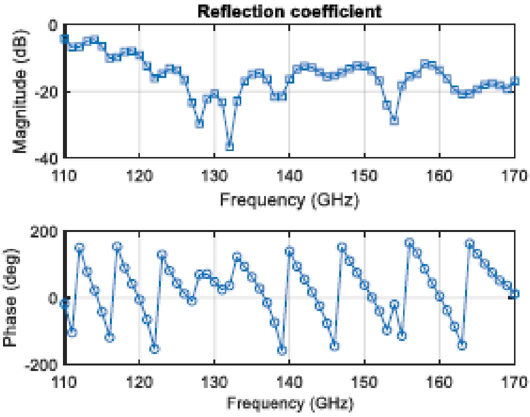

Fig. 14. VRC measurements of sensor A.

sensor is - 4.2 dB at 110 GHz and decreases as the frequency increases. It is lower than -11.5 dB for frequencies greater than 120 GHz. The phase of the sensor in Fig. 14 shows good continuity except for around 130 and 155 GHz, where the VRC magnitude is small. This is due to the uncertainty in the phase being related to the magnitude of the VRC and its associated uncertainty. When the magnitude is close to 0 (infinite in dB scale) and less than its uncertainty, the phase becomes undefined and can therefore be described as fully uncertain.

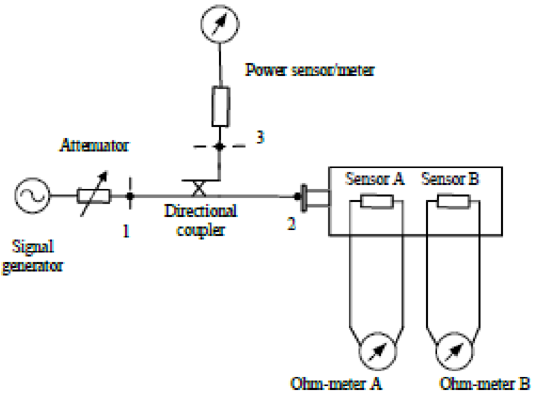

Fig. 15. Measurement setup for time response characterization of the sensor.

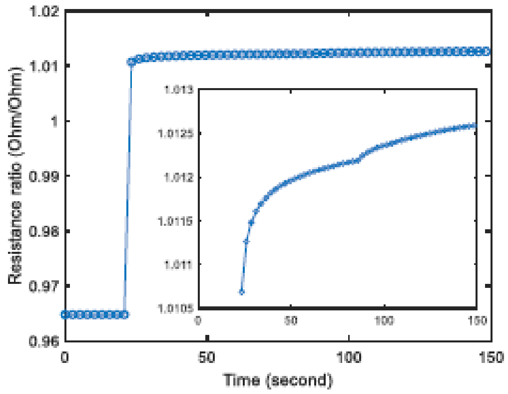

Fig. 16. Short-time response of the mounted sensor at 140 GHz.

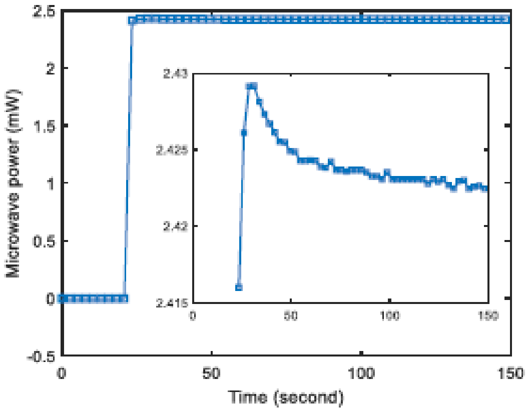

Fig. 17. The commercial PM5 sensor/meter combination power response under the same condition as the mounted sensor.

B. Short-Term Time Response

To characterize the short-term time response, the setup shown in Fig. 15 was used. A signal generator, including a WG29 multiplier was used to produce the necessary microwave signal and an attenuator was used to adjust the power level. This power flows through a 10 dB directional coupler whilst a small portion is coupled to port 3 where it can be measured by a commercial power sensor/meter combination (VDI Erickson PM5) [20], with its indication acting as a reference power. The shielded sensor A and B combination (Fig. 13) was connected to port 2 of the directional coupler, where a fixed proportion of the input power was incident upon. An Ohm-meter was connected to each of the sensor outputs A and B, respectively to measure the sensor's resistance.

To ensure that thermal equilibrium of the system had been reached, the sensor and system setup were connected and allowed to settle for 24 hours prior to measurement. Measurements were performed for power off and on, respectively, at 140 GHz. This frequency was chosen because of the relatively small VRC magnitude of the Sensor A. The measurement sequence began with a reading of the resistance of Sensor A and B using the ohm-meters with the power off for ~175 minutes. Power was then applied to sensor A while the output from ohm-meters were monitored. During all these measurements the output of the PM5 was also monitored. The time interval between two measurements from the same sensor was ~2.6 s and named as the measurement system response time. It should be noted that this time is limited by the response of our ohm meters, computer and cable delays. The estimated response time of the sensor itself (without any feedback) should be less than 2.6 s. This is competitive with commercial PM5 sensors. The time constant of the basic sensor in PM5/PM5B is 6 s [20]. Feedback electronics have been used to get a fast response time, whereas our sensor is raw.

The resistance ratio between sensor A and B was used to show the short-term response of the mounted sensor combination. This ratio eliminates the dependency of the sensor resistance on the ambient temperature and its variation effect on sensor A. The ratio of these resistances for the off and on states is shown in Fig 16. The sensor response time is much shorter (< 2.6 s) than the measurement system. The resistance of sensor A and B, measured with the system at thermal equilibrium and without any incident power was 1578.5 Ω and 1633.8 Ω respectively, giving a resistance ratio of 0.9662. After power was incident onto the sensor, the resistance ratio deviated slightly from the ratio of 1.0107 at approximately 25s to that of 1.0126 after 125s. This is a variation of 0.19% over this period. Given a typical measurement period of nominally 2 min for general applications, a test interval of 125 s was selected to calculate the mounted sensor deviations. The deviation of the reference power from the PM5 was also calculated for the same period and is depicted in Fig. 17. The deviation for the PM5 sensor was 0.27% for a nominal 2.5 mW power. The two deviations are very close to each other and shows that the mounted sensor has very good short-time response.

C. Long-Term Time Response

The other time dependent parameter to assess for the mounted sensor is the long-term response and how the sensor repeats with the power switched multiple times. The same setup as the short-term response measurement was used here. The measurement sequence was powered off-on-off-on-off, with each off and on lasting 175 minutes. The outputs of sensor A, sensor B and the reference power were measured at the same system time response interval as previously. The resistance ratio was once again recorded to eliminate the ambient temperature effect on the mounted sensor. This ratio and the measured reference power for each sequence are shown in Fig. 18. To evaluate the mounted sensor performance, the measured reference power by the PM5 sensor was used. The average and experimental standard deviation for each individual sequence (total of 4050 measurement points) were calculated and given in Table III. The standard deviations of the resistance ratios are consistent whereas those for the reference powers are different. This is due to the zeroing process of the commercial sensor. To make the two parameters more comparable, the difference between the ON and OFF parameters given in Table III was used. This difference in the reference power was 2.39931 mW and 2.38535 mW for the first and second power on-off cycles, respectively. For the mounted sensor, the resistance ratios were 0.04709 Ω/Ω and 0.04734 Ω/Ω.

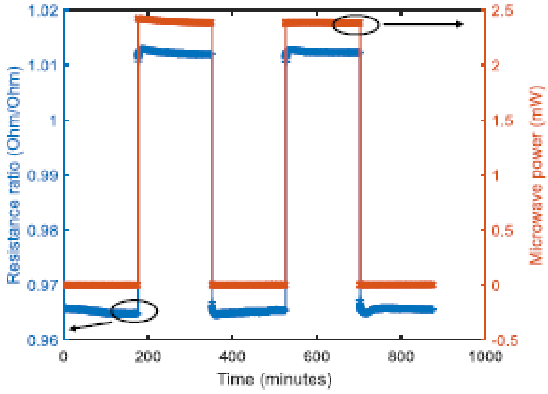

Fig. 18. The resistance ratio and reference power for the power off and on sequences at 140 GHz.

TABLE III

AVERAGE AND EXPERIMENTAL STANDARD DEVIATION FOR EACH SEQUENCE.

Sequence	Average Microwave power (mW)	Average Ratio (Ω/Ω)	Standard deviation Microwave power (mW)	Standard deviation Ratio (Ω/Ω)
Power off-1	-0.00198	0.96516	0.00028	0.00035
Power on-1	2.39733	1.01226	0.01162	0.00028
Power off-2	-0.00080	0.96506	0.00049	0.00023
Power on-2	2.38455	1.01240	0.00149	0.00016
Power off-3	0.00101	0.96559	0.00043	0.00024

The ratio of the standard deviations relative to the calculated differences is a more meaningful indicator of the sensor performance, allowing for direct comparison. The standard deviation ratios for the reference power were obtained as 0.484% and 0.062% for the first and second power on-off sequences, whilst for the mounted sensor these were 0.594% and 0.338%. This shows that the deviation of the mounted sensor is less than 0.6% and similar to the commercial power sensor.

D. Frequency Response

The frequency response (F_R) is a transfer function defined as the change of the mounted sensor's output resistance with respect to the incident microwave power onto the mounted sensor. This was calculated using (9), derived for the measurement setup in Fig. 15 using a 3-port power splitter methodology. The measurement was performed from 110 GHz to 170 GHz at a step of 5 GHz. A characterized PM5 sensor/meter [29] was used to monitor the microwave power at Port 3.

$$F_R = EE\frac{\Delta R}{P_{STD}}\frac{|S_{31}|^2}{|S_{21}|^2}\frac{1-|\Gamma_{STD}|^2}{1-|\Gamma_{MS}|^2}\frac{|1-\Gamma_2\Gamma_{MS}|^2}{|1-\Gamma_3\Gamma_{STD}|^2} \qquad (9)$$

where EE is the effective efficiency of the PM5 sensor/meter given in [29], P_{STD} is the measured microwave power from the power sensor/meter, S_{31} and S_{21} are voltage transfer

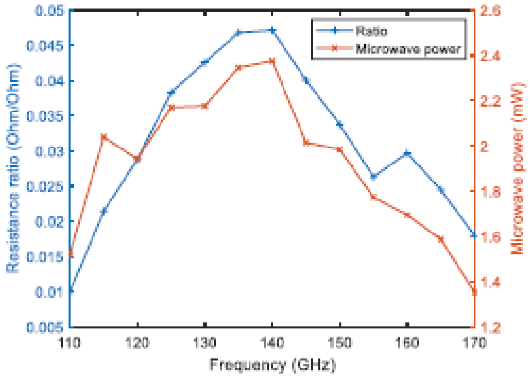

Fig. 19. Measured power from the sensor/meter and the resistances ratio of sensor A and B for a 3-min waiting time interval.

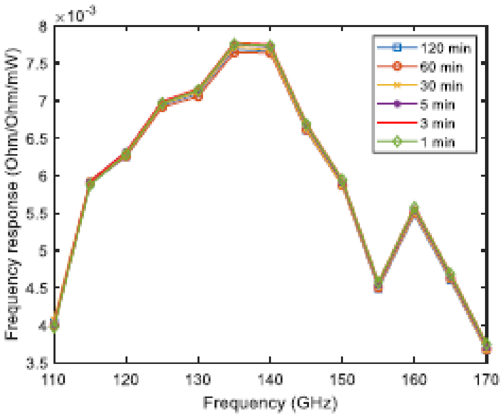

Fig. 20. The frequency response for different waiting time intervals.

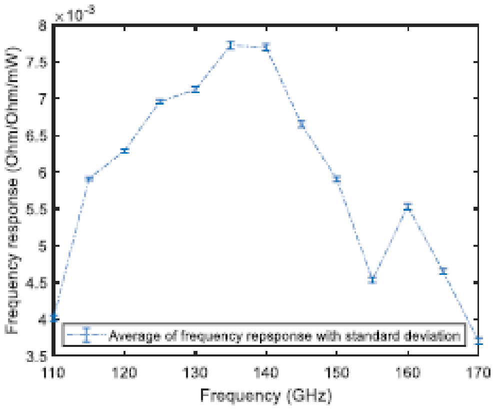

Fig. 21. Average and standard deviation of the frequency response.

coefficients from port 1 to 3 and from port 1 to 2, respectively. Γ_{MS} is the voltage reflection coefficient of the mounted sensor, Γ_{STD} is that of the power sensor/meter, Γ_2 and Γ_3 are those of port 2 and 3 of the directional coupler, and ΔR is the difference between the resistance ratios for microwave off and on for sensor A and sensor B.

The measurement was performed, firstly, for microwave power off, measuring sensor A and sensor B resistances and the power meter/sensor output power with 150 samples taken and average. Afterwards, microwave power was applied to the directional coupler incrementally from 110 GHz to 170 GHz, and the aforementioned parameters were measured again at each frequency. The ratio for the resistance changes of sensor A and B were calculated for all measured points including power off. The difference between the ratios with respect to each frequency point and power off was used as the ΔR parameter.

The frequency response for different waiting time intervals between the two measurement points (e.g., two consecutive frequency points) was analysed with waiting times between 1 and 120 minutes. The measured ΔR and P_{STD} for a waiting interval of 3 minutes are illustrated in Fig. 19.

The frequency responses for different waiting times (1, 3, 5, 30, 60 and 120 minutes) were calculated using (9) and shown in Fig. 20. An average of all measurements with standard deviation is shown in Fig. 21. The minimum and maximum standard deviation at one-sigma were 0.36% (115 GHz) and 0.66% (135 GHz). This shows that the mounted sensor has very reproducible frequency response between 1 – 120 min intervals.

E. Linearity

Linearity is a parameter that shows how the mounted sensor's response behaves at different input power levels at a single frequency. The measurement setup in Fig. 15 was used. The input power was varied from -10 dBm to 9 dBm for each frequency from 110 GHz to 170 GHz at 5 GHz steps using the waveguide attenuator. The resistances of Sensor A and B and the reference power were monitored. The microwave power was worked out using the resistance ratios for each measured point and the frequency response (Fig 21) of the mounted sensor. The mounted sensor response at +5 dBm at each frequency was used as a reference. The measured deviation from this reference was plotted in Fig. 22. It can be observed the deviation varies between ±1.5 dB and ±0.6 dB from -10 dBm to -3 dBm. Above this power level, the deviation is within ±0.25 dB. The deviation at 110 GHz is the highest due to the relatively high VRC.

VI. CONCLUSION

A D-band thin-film bolometer with a unique folded-line structure in the E-plane was designed, fabricated and characterized as a transfer standard. The circuit analysis and simulations show the folded-line structure improves bandwidth. The effect of ambient temperature drift is reduced in this design by using low thermal conductive materials for the sensor chip (quartz), its wrapping (polyimide) and the detector housing (PEEK). The compensation sensor (B) detects the ambient variation and removes its impact on the

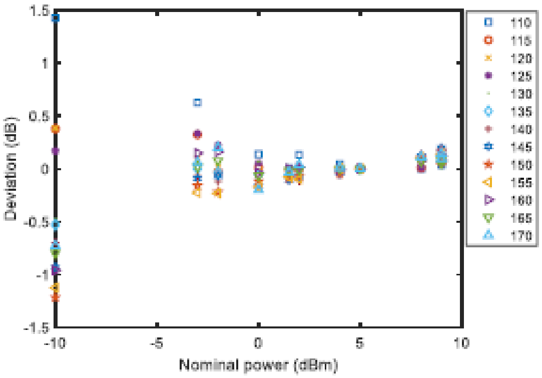

Fig. 22. The Linearity of the mounted sensor from 110 GHz to 170 GHz in 5 GHz step.

power sensor. The device is successfully characterized as a transfer/working standard which can be used in ambient temperature environments. The measured return loss is above 10 dB from 122 GHz to 170 GHz. The deviation in the sensor's response (0.19 %) for the given short-time interval is very close to the commercial sensor (0.27 %). The sensor exhibits very good short-time response with a response time much better (< 2.6 s) than the measurement system. The long-term time response showed that the sensor is thermally very well isolated from the surrounding, and the standard deviation is less than 0.6 %. This indicates the sensor performs excellently. However, the lowest power that can be measured depends on the acceptable deviation from linearity. From -3 dBm to 10 dBm, the deviation is limited within ±0.6 dB.

REFERENCES

[1] P. H. Siegel, "Terahertz Technology," *IEEE Trans. Microw. Theory Tech.*, vol. 50, no. 3, pp. 910–928, 2002.

[2] X. Shang, M. Ke, Y. Wang, and M. J. Lancaster, "WR-3 band waveguides and filters fabricated using SU8 photoresist micromachining technology," *IEEE Trans. Terahertz Sci. Technol.*, vol. 2, no. 6, pp. 629–637, 2012.

[3] N. Erickson, "A Fast and Sensitive Submillimeter Waveguide Power Meter," *Tenth International Symposium on Space Terahertz Technology*. pp. 501–507, 1999.

[4] M. Salek *et al.*, "Design, Fabrication, and Characterization of a D-Band Bolometric Power Sensor," *IEEE Trans. Instrum. Meas.*, vol. 71, pp. 6–14, 2022.

[5] J. A. Mallat, S. N. Dudorov, D. V. Lioubtchenko, and A. V. Räisänen, "110-170 GHz millimetre wave power standard," *Proc. 36th Eur. Microw. Conf. EuMC 2006*, no. September, pp. 482–485, 2006.

[6] W. He, W. Zhang, W. Qi, and H. Yin, "Design of a 110GHz to 170GHz calorimeter," *2017 Int. Work. Electromagn. Appl. Student Innov. Compet. iWEM 2017*, no. 1, pp. 71–73, 2017.

[7] Y. Tojima, M. Kinoshita, H. Iida, and K. Fujii, "Development of WR-5 Waveguide Calorimeter for Millimeter Wave Power Standard," *CPEM 2018 - Conf. Precis. Electromagn. Meas.*, pp. 1–2, 2018.

[8] C. Ma, X. Cui, W. Yuan, and Y. Li, "Design of a WR-6 thermoelectric conversion power sensor," *IRMMW-THz 2015 - 40th Int. Conf. Infrared, Millimeter, Terahertz Waves*, vol. 6, pp. 1–2, 2015.

[9] X. Wang, Q. Zhong, J. Li, W. Yuan, Y. Li, and X. Cui, "WR-06 Power Standard Devices," *CPEM 2018 - Conf. Precis. Electromagn. Meas.*, pp. 1–2, 2018.

[10] D. Adamson, J. Miall, J. Howes, M. Harper, and R. Thompson, "A new 75-110 GHz primary power standard with reduced thermal mass," *75th ARFTG Microw. Meas. Conf. Meas. Modul. Signals Commun.*, pp. 1–4, 2010.

[11] J. Y. Kwon, Y. P. Hong, D. J. Lee, and T. W. Kang, "V- and W-band waveguide microcalorimeters for millimeter-wave power standards," *85th ARFTG Microw. Meas. Conf. Meas. Tech. 5G Appl. ARFTG 2015*, pp. 1–3, 2015.

[12] I. Lemco and B. Rogal, "Resistive-Film Milliwatmeters For The Frequency Bands 8.2-12.4Gc/s, 12.4-18Gc/s and 26.5-40Gc/s," *Inst. Electr. Eng. Sep. 1960*, vol. 16, no. 3298, pp. 16–19, 1960.

[13] J. A. Lane and D. M. Evans, "The design and performance of transverse-film bolometers in rectangular waveguides," *Proc. IEE Part B Electron. Commun. Eng.*, vol. 108, no. 37, p. 133, 1961.

[14] K. Sukurai and T. Nemoto, "A Thin-Film Bolometer Unit," *IEEE Trans. Instrum. Meas. Sept. 1967*, vol. IM, no. 3, pp. 206–211, 1967.

[15] T. Inoue, I. Yokoshima, and M. Sasaki, "High-Performance Thin-Film Barretter Mount For Power Measurement In W-Band," *Electron. Lett.*, vol. 21, no. 5, pp. 170–172, 1985.

[16] L. Brunetti, "Thin-film bolometer for high-frequency metrology," *Sensors Actuators A. Phys.*, vol. 32, no. 1–3, pp. 423–427, 1992.

[17] Y. Tojima, M. Kinoshita, H. Iida, and K. Fujii, "Calibrating Power Meters in the 140-220-GHz Frequency Range Using an Absolute-Power Reference Calorimeter," *IEEE Trans. Instrum. Meas.*, vol. 70, 2021.

[18] D. Gu, X. Lu, B. F. Jamroz, D. F. Williams, X. Cui, and A. W. Sanders, "NIST-Traceable Microwave Power Measurement in a Waveguide Calorimeter with Correlated Uncertainties," *IEEE Trans. Instrum. Meas.*, vol. 68, no. 6, pp. 2280–2287, 2019.

[19] J. Y. Kwon, Y. P. Hong, and N. W. Kang, "D-Band Waveguide Microcalorimeter for Millimeter-Wave Power Standard," *CPEM 2018 - Conf. Precis. Electromagn. Meas.*, pp. 1–2, 2018.

[20] Virginia Diodes Inc, "PM5 Operational Manual," vol. 6172, Charlottesville, VA, USA, p. 22, 2016.

[21] R. H. Judaschke, K. Kuhlmann, T. M. Reichel, and W. Perndl, "Millimeter-Wave Thermoelectric Power Transfer Standard," *IEEE Trans. Instrum. Meas.*, vol. 64, no. 12, pp. 3444–3450, 2015.

[22] Y. S. Lau, T. Denning, and C. Oleson, "Millimeter wave power measurement above 110 GHz," *2006 67th ARFTG Microw. Meas. Conf. - Meas. Des. High Power Devices Syst.*, pp. 97–102, 2006.

[23] H. Toda, K. Sasaki, Y. Nakagawa, and I. Sugiura, "Matched-Load-Type Thermoelectric Transducer for Power Measurements in the Millimeter Wave Region," *IEE Conf. Publ.*, vol. IM, no. 113, pp. 188–190, 1974.

[24] J. A. Lane, "Transverse film bolometers for the measurement of power in rectangular waveguides," *Proc. IEE - Part B Radio Electron. Eng.*, vol. 105, no. 19, pp. 77–80, 1958.

[25] N. Marcuvitz, *Waveguide Handbook*, First. McGraw-Hill Book Company, Inc, 1951.

[26] X. Cui, Y. S. Meng, Y. Shan, and Y. Li, "Microwave Power Measurements: Standards and Transfer Techniques," *New Trends Dev. Metrol.*, pp. 3–20, 2016.

[27] N. Hiromoto *et al.*, "High Responsivity and Low NEP of Room-Temperature Terahertz Antenna-Coupled Microbolometers with Meander Titanium Thermistor," *Int. Conf. Infrared, Millimeter, Terahertz Waves, IRMMW-THz*, vol. 2019-Septe, 2019.

[28] R. S. Saxena, R. K. Bhan, C. R. Jalwania, and K. Khurana, "Effect of excessive bias heating on a titanium microbolometer infrared detector," *IEEE Sens. J.*, vol. 8, no. 11, pp. 1801–1804, 2008.

[29] M. Celep, M. Salek, D. Stokes, J. Skinner, and Y. Wang, "Power Sensor Characterization from 110 to 170 GHz Using a Waveguide Calorimeter," *IEEE Trans. Instrum. Meas.*, vol. 71, 2022.

Zero-bias Schottky Diode Power Detector for D-band

Harshwardhan Kamble#1, Milan Salek#2, Yi Wang#3
#University of Birmingham, U.K.
{1hxk940, 2m.salek, 3y.wang.1}@bham.ac.uk

***Abstract* — The D-band (110 - 170 GHz) waveguide-based zero-bias Schottky diode (ZBD) power detector is reported. The design aims to get high responsivity across the band. The circuit is fabricated on a 50 µm thick quartz substrate. A 3D model and spice model of a commercially available zero-bias Schottky diode are used in the design. The detector achieves the average responsivities of nearly 5000 V/W and a minimum of 1900 V/W at higher frequencies. The detector circuit is housed in a gold-plated metallic block for measurements.**

Keywords — Direct detection, Schottky diode, power detector, millimetre wave, responsivity, waveguide to microstrip transition.

I. INTRODUCTION

The sub-terahertz band above 100 GHz is not substantially commercialised due to parasitic losses, less efficiency, and thermal challenges [1], [2]. However, the band is getting attention due to the large available bandwidth and the atmospheric window. This has led to applications in backhaul communication, image sensing and radiometry, radar and astronomy. Schottky diodes are favoured at higher frequencies for their fast response time and suitability for use in varying temperatures [3].

The Schottky diode direct detectors are used in terahertz imaging [4], radiometry [5], communication [6], spectroscopy [7], and particle accelerator [8]. Unlike heterodyne detectors, direct detectors do not require a local oscillator; hence the system is simple and consumes less power [6], [9].

Schottky diode power detectors are widely used in six-port based radars [10] and communication systems [11]. Direct detection is getting attention, especially for space applications, as it allows denser packaging/integration and is being pushed above 100 GHz [12], [13]. The waveguide-based compact six-port technology can also be found at D-band [14]. All these create a need for a power detector above 100 GHz with a typical responsivity of 1000 V/W [12]. Some reported power detectors are given in Table 1.

II. DESIGN

A diode power detector operates in the square law region in small-signal conditions. It produces current proportional to the square of the input voltage, which corresponds to the input RF power. The frequency spectrum of the output of a diode detector contains fundamental and higher-order harmonics with reduced power compared to the fundamental frequency. At higher frequencies, the planar diode structure suffers from parasitic, which makes matching challenging. So, it is important to mention that the performance of the diode-based device depends not only on the external circuit but also on the diode structure. Techniques to reduce the parasitic have been extensively studied [15].

In the design process, the stepped impedance low pass filter (LPF) was designed first to find the substrate width as it contains large capacitive sections occupying a large portion of the substrate. The next step was to design the Waveguide to Microstrip (W-to-M) transition with the current return path (CRP), which defines the channel/recess opening height into the waveguide. The *S*-parameters of these individual designs and the diode 3D model are imported to Keysight ADS after being simulated in CST Microwave Studio. The matching circuit is then designed and optimised for better responsivity.

A. Low-Pass Filter and Transition with Current Return Path

The stepped impedance low pass filter is common and straightforward to design. A 5th-order, 0.5 dB ripple, Chebyshev stepped impedance low pass filter is designed for a wide stop band, as shown in Fig. 1. The cut-off frequency (f_C) of the filter is chosen such that its stop band lies in the fundamental D-band. The f_C from the simulated response is 62 GHz, and stop band insertion loss is 20 dB. The low (~ 16 Ω) and high (~ 102 Ω) impedance line widths are 500 µm and 25 µm, respectively, and the corresponding line lengths are $l_1 = l_5 = 200$ µm; $l_2 = l_4 = 250$ µm; and $l_3 = 300$ µm. The substrate width is chosen to be 50 µm wider on either side (of low imp. line); therefore, its width is 600 µm.

The W-to-M transition is designed with three sections of lines (50 Ω line, central line and probe) narrowing down towards the probe. The 50 Ω microstrip line width at 140 GHz can be calculated as 107.3 µm. The width of the central line (71.5 µm) and the probe (35.8 µm) are initially selected as two-thirds and one-third of the 50 Ω line, respectively. The CRP (of 25 µm line) is the ground for low frequency placed before the diode to complete the direct current (DC) loop. The W-to-M transition and return path are designed in a single structure, as shown in the inset of Fig. 2.

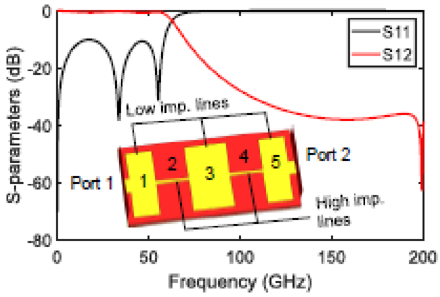

Figure 1. Stepped impedance low-pass filter

TABLE 1 DIODE POWER DETECTORS COMPARISON

Reference	Diode technology	Frequency (GHz)	Return Loss (dB)	Responsivity (V/W)
This work	Teratech ZBD	110-170	>2.5	1900-10500 @ -20 dBm 130 – 160 GHz
[16]	InGaAs/InP SBD	340-400	-	100-800 (graph)
[6]	ZBD	315-357	-	910~2210
[17]	VDI ZBD	110-170	-	2500-4000 (graph)
[18]	Aeroflex MZBD-9161 GaAs	110-170	4 (typical)	Typical 600, Highest 1600
		75-110	5 (typical)	2000-11800 @ 80 – 104 GHz
[7]	InGaAs ZBD	75-110	-	800-3000 (graph) @ 75-105 GHz
[19]	Aeroflex/Metelics MZBD-9161	75-110	-	125-1000 (graph)
[20]	Sb-heterostructure InAs/GaAlSb	75-110	-	2000-11000 (graph)
[5]	ACST ZBD	78-97	>10	8600 @-30dBm, 89 GHz

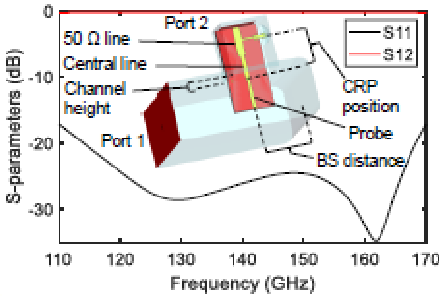

Figure 2. Waveguide to Microstrip transition and current return path.

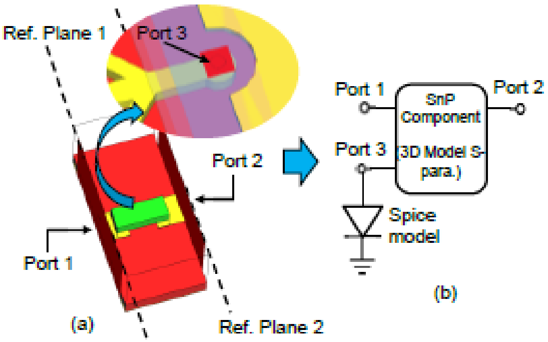

Figure 3. (a) Diode 3D model on microstrip line (b) Diode spice model connected at intrinsic anode port 3.

The W-to-M transition sets the dimension of the channel/recess that opens into the waveguide. The width of the channel is 700 µm considering 50 µm tolerance on either side of the substrate. The height of the channel (550 µm), the position of the current return path (575 µm) on the main microstrip line, and the widths of the central lines (61.5 µm) and probe (45.8 µm) are optimised to get a transmission response of better than 0.26 dB and a return loss of more than 15 dB. The material of the waveguide and the substrate during the simulation are gold ($\sigma = 4.561\times10^7$ S/m) and quartz ($\tan\delta = 0.0004$), respectively. The back-short (BS) distance in the waveguide is fixed to a quarter-wavelength ($\lambda_g/4$), that is 700 µm, calculated at 140 GHz.

B. Diode Simulation and Matching Circuits

The Schottky diode 3D model and spice model are provided by the manufacturer. The diode 3D model is implemented on a 50 Ω microstrip line in CST, as shown in Fig. 3(a). The microstrip line on the anode side is assigned as Port 1, and the line on the cathode side is Port 2. Port 3 is set at the anode surface where the diode spice (non-linear) model is connected, as shown in Fig. 3(b). This technique makes it easy to determine diode embedding impedances without requiring an equivalent circuit [21]. The diode 3D model incorporated with the spice model acts as a complete single diode circuit to be used for the design. The microstrip ends on either side of the diode act as a reference plane around which the rest of the detector circuitry is placed.

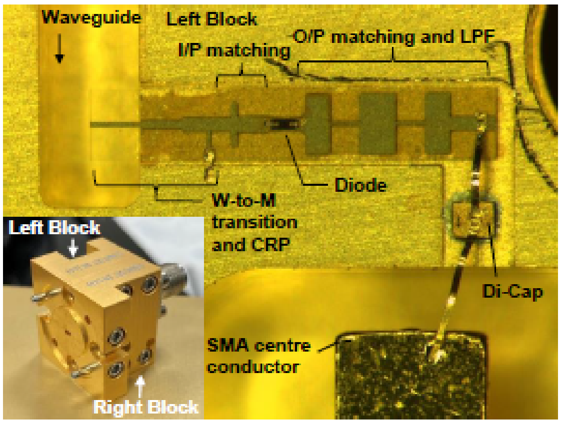

Figure. 4. Fabricated detector.

After placing all the earlier structures, the W-to-M transition with return path, diode, LPF and 1 MΩ load (typical for voltmeter) in ADS, the input (I/P) and output (O/P) matching circuits are designed and optimised using three microstrip lines, two at the input and the other one at the output for high broadband responsivity.

It must be noted that 3D structures in CST must be simulated from 0 Hz (DC) to the required highest frequency, 170 GHz. This will ensure DC information is present in the *S*-parameter data file. So, when simulated in ADS, the circuit will have a DC path giving the correct DC voltages at the output. Also, CST might not simulate the structure with significant differences in the dimensions of the features. In that case, alternatives such as Ansys HFSS can be used.

III. FABRICATION AND MEASUREMENT

The detector split blocks are fabricated in aluminium and plated with gold, as shown in Fig. 4. The dielectric capacitor (Di-Cap) is used to step down the long bond wire, which avoids possible short circuits to the narrow channel and simultaneously acts as a low-pass filter. Also, this secures the bonding contact at the microstrip output.

The simulated and measured reflection coefficients are compared in Fig. 5. The measured return loss is better than 2.5 dB, whereas the simulated return loss is better than 1 dB.

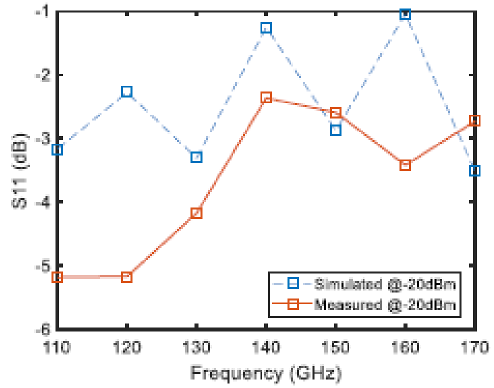

Figure 5. Reflection coefficient.

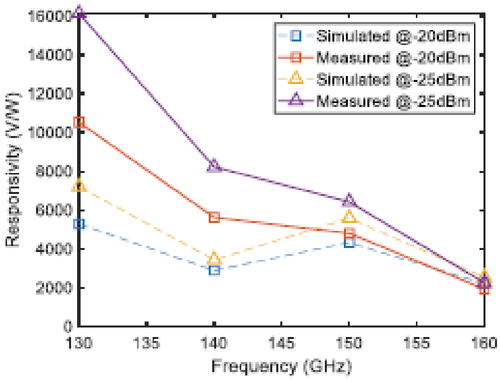

Figure 6. Responsivity versus Frequency.

These S_{11} responses are typical for Schottky devices and challenging to improve further. The trend of both graphs is the same, showing better matches at lower frequencies, especially for the measured response.

The measured and simulated responsivity at two power levels (-20 and -25 dBm) are plotted in Fig. 6. The minimum responsivity in all cases is nearly 2000 V/W. The trend of measured and simulated responsivity is in agreement. However, the effect of matching can be clearly seen. The responsivity is better at lower frequencies, and the average responsivity is nearly 5000 V/W. The variation in measured responsivity (1900-10500 V/W) is more than the simulated (2200-5200 V/W) at -20 dBm input power. This can be attributed to fabrication uncertainty, and process variation can be a part of further study.

IV. CONCLUSION

The D-band Schottky diode power detector is designed, fabricated and measured. The measured return loss is better than 2 dB for the entire D-band. The responsivity depends on matching. At lower frequencies, the matching is better hence the responsivity. The detector reaches higher average responsivity of nearly 5000 V/W than those reported in the literature but suffers from the variation from 1900 V/W to 10500 V/W at -20 dBm. The detector can be improved in future to reduce variation in responsivity. The SMA is at the back, parallel to the waveguide, making installation into the system easy. The designed power detector may find applications in six-port receivers and radiometers.

REFERENCES

[1] P. H. Siegel, "Terahertz Technology," *IEEE Trans. Microw. Theory Tech.*, vol. 50, no. 3, pp. 910–928, 2002.
[2] N. Cahoon, P. Srinivasan, and F. Guarin, "6G Roadmap for Semiconductor Technologies: Challenges and Advances," *IEEE Int. Reliab. Phys. Symp. Proc.*, vol. 2022-March, pp. 11B11-11B19, 2022.
[3] S. M. Sze and K. N. Kwon, *Physics of Semiconductor Devices*, Third. Hoboken, New Jersey: John Wiley & Sons, Inc., 2007.
[4] H. Ko *et al.*, "Zero-bias InGaAs Schottky barrier diode array for terahertz imaging applications," *2014 Optoelectron. Commun. Conf. OECC 2014 Aust. Conf. Opt. Fibre Technol. ACOFT 2014*, no. July, pp. 982–983, 2014.
[5] M. Hoefle *et al.*, "89 GHz zero-bias Schottky detector for direct detection radiometry in European satellite programme MetOp-SG," *Electron. Lett.*, vol. 50, no. 8, pp. 606–608, 2014.
[6] Y. Tian, J. Jiang, Q. Liu, C. Lin, K. Huang, and X. Deng, "A 15Gps high speed OOK receiver based on a 0.34THz Zero-bias Schottky diode detector," *27th Int. Symp. Sp. Terahertz Technol. ISSTT 2016*, vol. 2, pp. 8–10, 2017.
[7] N. Daghestani *et al.*, "Room temperature ultrafast InGaAs Schottky diode based detectors for terahertz spectroscopy," *Infrared Phys. Technol.*, vol. 99, no. December 2018, pp. 240–247, 2019.
[8] A. Semenov *et al.*, "Schottky diode detectors for monitoring coherent THz synchrotron radiation pulses," *IPAC 2014 Proc. 5th Int. Part. Accel. Conf.*, pp. 3465–3467, 2014.
[9] C. Goldstein, M. Trier, A. Maestrini, and J. C. Orlhac, "Present and future R&T development in CNES for Microwave radiometer," *2006 IEEE MicroRad Proc. - 9th Spec. Meet. Microw. Radiom. Remote Sens. Appl. MicroRad'06*, no. 0, pp. 60–65, 2006.
[10] F. Michler, S. Lindner, F. Lurz, S. Erhardt, R. Weigel, and A. Koelpin, "Zero-bias schottky power detector design for six-port based radar systems," *Eur. Microw. Week 2017 "A Prime Year a Prime Event", EuMW 2017 - Conf. Proceedings; 47th Eur. Microw. Conf. EuMC 2017*, vol. 2017-Janua, pp. 228–231, 2017.
[11] S. O. Tatu and E. Moldovan, "Alternative millimeter-wave communication receivers in six-port technology," *Can. Conf. Electr. Comput. Eng.*, no. May, pp. 2337–2340, 2006.
[12] P. Piironen, "Millimetre-Wave Direct Detection Receivers for Earth Observation Instruments - Trends and Challenges," *GSMM 2022 - 14th Glob. Symp. Millimeter-Waves Terahertz*, no. Ici, pp. 74–77, 2022.
[13] E. Bryerton, T. Reck, J. Hesler, and T. Crowe, "Sub-millimeter Wave Compact Correlation Radiometers," *2022 Asia-Pacific Microw. Conf.*, pp. 931–933, 2022.
[14] X. Chen, M. Salek, Q. Zhang, and Y. Wang, "Subterahertz Filtering Six-Port Junction," *IEEE Trans. Microw. Theory Tech.*, vol. 70, no. 8, pp. 3877–3885, 2022.
[15] S. Jenabi, A. Malekabadi, D. Deslandes, F. Boone, and S. A. Charlebois, "Submillimeter wave GaAs Schottky diode application based study and optimization for 0.1–1.5 THz," *Solid. State. Electron.*, vol. 134, pp. 65–73, 2017.
[16] T. Ren, Y. Zhang, R. Xu, J. Zhou, C. Yang, and Z. Jin, "A 340-400 GHz Zero-Biased Waveguide Detector Using an Self-Consistent Method to Extract the Parameters of Schottky Barrier Diode," *Appl. Comput. Electromagn. Soc. J.*, vol. 30, no. 12, pp. 1334–1340, 2015.
[17] J. L. Hesler and T. W. Crowe, "NEP and Responsivity of THz Zero-Bias Schottky Diode Detectors," *IRMMW-THz2007 - Conf. Dig. Jt. 32nd Int. Conf. Infrared Millimetre Waves, 15th Int. Conf. Terahertz Electron.*, pp. 844–845, 2007.
[18] Y. Changfei, Z. Ming, L. Yunsheng, and X. Conghai, "Millimeter wave broadband high sensitivity detectors with zero-bias Schottky diodes," *J. Semicond.*, vol. 36, no. 6, pp. 1–5, 2015.
[19] M. Tekbas, M. S. Erdogan, and I. Unal, "A W band waveguide detector module using zero bias schowttky diode," *2017 IEEE 37th Int. Conf. Electron. Nanotechnology, ELNANO 2017 - Proc.*, pp. 137–142, 2017.
[20] J. N. Schulman *et al.*, "W-Band Direct Detection Circuit Performance With Sb-Heterostructure Diodes," *IEEE Microw. Wirel. Components Lett.*, vol. 14, no. 7, pp. 316–318, 2004.
[21] J. L. Hesler *et al.*, "Fixed-tuned submillimeter wavelength waveguide mixers using planar schottky-barrier diodes," *IEEE Trans. Microw. Theory Tech.*, vol. 45, no. 5 PART 1, pp. 653–658, 1997.